Magnetic Properties
of
Molecular and Nanoscale Magnets

DISSERTATION

zur Erlangung des akademischen Grades

Doctor rerum naturalium
(Dr. rer. nat.)

vorgelegt
der Fakultät für Mathematik und Naturwissenschaften
der Technischen Universität Dresden

von

Diplom-Physikerin
Yulia Krupskaya

Gutachter: Prof. Dr. B. Büchner
Prof. Dr. R. Klingeler

Tag der Einreichung: 11. 04. 2011
Tag der Disputation: 18. 08. 2011

Contents

0 Introduction

The interest in nanosized materials has developed in the 1980s in the frame of the emerging field of so-called nanoscience. The idea of miniaturization of devices in order to increase their efficiency and convenience became more and more exciting and motivated a lot of research in this field. The use of nanomaterials enables, for example, development of high-density magnetic data storage devices [1]. On the other hand, in biology and medicine, magnetic nanoparticles found a particularly large number of interesting and promising applications, like in drug delivery and cell separation, as agents for magnetic resonance imaging and magnetic hyperthermia [2, 3].

From the scientific point of view, it was realized that nanosize objects are complex enough to give rise to absolutely new physical properties, while simple enough that they can be investigated very deeply and in great detail. The miniaturization of devices down to the nanoscale where quantum effects become relevant demands a detailed understanding of the interplay between classical and quantum properties. In magnetism, one of the most spectacular phenomena is the possibility to observe quantum tunnelling effects in mesoscopic matter.

A scheme of the size effects in the magnetization and its dynamics in ferromagnets is shown in Fig. 0.1 [4]. On the macroscopic scale, the magnetic energy is minimized by forming magnetic domains, regions in space where all the individual moments are aligned in the same direction, separated by so-called domain walls. When the system size is comparable to the domain wall width or the exchange length, the formation of domain walls becomes energetically unfavorable and single domain behavior emerges. The magnetic anisotropy of such a particle strongly depends on its size and shape. In general, on reducing the size of the particle the anisotropy barrier for the reorientation of the magnetization becomes eventually comparable with the thermal energy. In this case, the magnetization can spontaneously fluctuate and, therefore, the system does not remain magnetized in zero magnetic field.

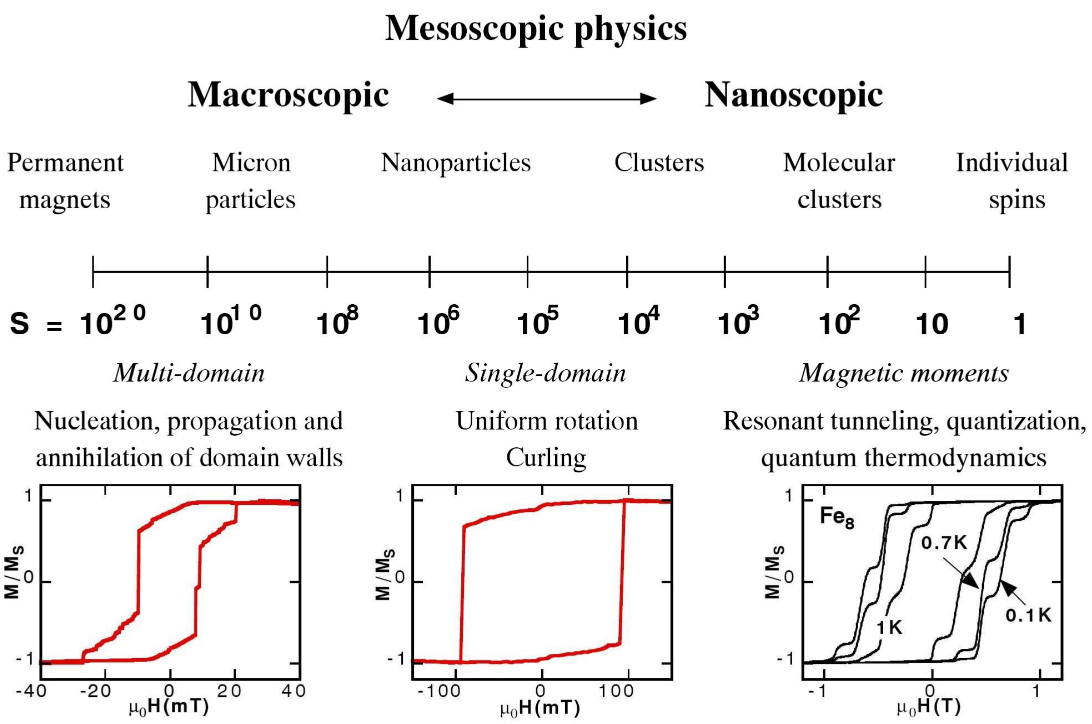

Figure 0.1: A scheme of the size effects in the magnetization dynamics [4]. The unit on the scale is the number of magnetic moments in the ferromagnetic system.

For system sizes well below the domain wall width or the exchange length, one must take explicitly into account single magnetic moments (spins) and their coupling. The final point in the minimization of the number of magnetic centers are molecular magnetic clusters. Up to now, these systems have been the most promising candidates in magnetism for observing quantum phenomena. A big advantage of the molecular magnetic complexes is their well-defined structure with a well-characterized spin ground state and magnetic anisotropy. These molecules can be easily organized into single crystals where all molecules often have the same orientation. Therefore, macroscopic measurements can give information about single molecule properties [4].

Characterization of newly produced molecular and nanoscale magnets is a very important part of this research. Studying structural and magnetic properties and the interplay between them reveals ways to improve the material and to obtain the desired properties. The main goal of this thesis is the investigation of magnetic properties of molecular magnetic clusters and magnetic nanoparticles recently synthesized by several collaborating groups. This thesis contains two main parts focusing on each of these two topics.

In the first part the fundamental studies on novel metal-organic molecular complexes are presented. Several newly synthesized magnetic complexes were investigated by means of different experimental techniques, in particular, by electron spin resonance spectroscopy. Chapter 1 in this part provides the theoretical background which is necessary for the interpretation of the effects observed in single molecular magnetic clusters. Chapter 2 introduces the experimental techniques applied in the studies. Chapter 3 contains the experimental results and their discussion. First, the magnetic properties of two Ni-based complexes are presented. The complexes possess different ligand structures and arrangements of the Ni-ions in the metal cores. This dramatically changes the properties of the molecules such as the ground state and the magnetic anisotropy. Secondly, a detailed study of the Mn_2Ni_3 single molecular magnet is described. The complex has a bistable magnetic ground state with $S = 7$ and shows slow relaxation and quantum tunnelling of the magnetization. The third section concentrates on a Mn(III)-based single chain magnet which shows a ferromagnetic ordering of the Mn-spins and a strong magnetic anisotropy. These two factors result in a hysteretic behavior of the magnetization at relatively high temperatures (up to 3 K). The last section is a detailed study of the static and dynamic magnetic properties of three Mn-dimer molecular complexes by means of static magnetization, continuous wave and pulse electron spin resonance measurements. The study reveals a dependence of the magnetic properties on the nearest ligands surrounding the Mn ions. Finally, the main results presented in the first part of the thesis are summarized.

The second part of the thesis is focussed on the magnetic properties of nanoscaled magnets such as carbon nanotubes filled with magnetic materials and carbon-coated magnetic nanoparticles. The main idea of this study points towards application of these particles as agents for magnetic hyperthermia. In this respect, their behavior in static and alternating magnetic fields is investigated and discussed. Moreover, two possible hyperthermia applications of the studied magnetic nanoparticles are presented, which are the combination of a hyperthermia agents with an anticancer drug and the possibility to spatially localize the hyperthermia effect by applying specially designed static magnetic fields.

I. Fundamental Studies of Molecular Magnetic Clusters

1 Electron Spin Resonance

Electron spin resonance (ESR) also known as electron paramagnetic resonance (EPR) is a spectroscopic method for determining the structure, dynamics, and the spatial distribution of paramagnetic species. This method is based on the resonance absorption of electromagnetic radiation of a certain frequency by a (para)magnetic center placed in a magnetic field. There is a variety of classes of systems which can be investigated by the ESR technique: transition metal and other magnetic ions, free radicals, defects in solids, metals, gases, etc. All these systems can have unpaired electrons giving rise to the electron spin resonance.

In this chapter the physical background of ESR will be described. A model of a free electron spin is used to introduce main phenomena and effects. Afterwards, in order to come closer to the real systems of interest, the physics of a many-electron ion and crystal structure influence will be discussed. Since all the compounds investigated in this work are based on $3d$-transition metal ions, the discussion will concentrate on magnetic properties of the electrons in the $3d$-shell. Further, the effective spin Hamiltonian approach will be introduced. This formalism allows a description of properties probed by ESR and magnetization experiments in terms of simple phenomenological parameters. The last part of this chapter will describe the pulse ESR method used for studying dynamic properties of paramagnetic centers.

1.1 The Magnetic Resonance Phenomenon

If a system with a spin of $S = 1/2$ (e.g. a free electron) is placed in an external homogeneous magnetic field directed along the z-axis, $\mathbf{H} = H_z\mathbf{e}_z$, its projection will quantize with respect to the field direction. Since the spin is associated with a magnetic moment,

$$\boldsymbol{\mu} = -g\mu_{\mathrm{B}}\mathbf{S}\,, \tag{1.1}$$

its direction influences the energy of the system,

$$E(m_S) \,=\, g\mu_{\mathrm{B}}\,\mathbf{S}\cdot\mathbf{H} \,=\, g\mu_{\mathrm{B}}m_SH_z\,. \tag{1.2}$$

Here, μ_{B} is the Bohr magneton, m_S is the z-component of the spin operator $\mathbf{S}$, which in the case of $S = 1/2$ possesses values of $\pm1/2$. The value of a magnetic moment of a free electron is not exactly $1\,\mu_{\mathrm{B}}$ as predicted by Uhlenbeck, Goudsmit and also by Dirac's theory, but slightly larger due to radiative corrections predicted by quantum electrodynamics. Therefore, the proportionality factor g (the gyromagnetic factor or g-factor) for the free electron differs from 2,

$$g_e \,=\, 2\,(1+\alpha/2\pi - ...) \,\approx\, 2.00232\,, \tag{1.3}$$

where α is the fine-structure constant. For many (but not all) solid state experiments it is sufficient to assume $g_S = 2$. In general, Eq. (1.2) is also valid when both orbital L and spin S momentum are present. Then S must be replaced by the total angular momentum J, and the value of g depends on the nature of the coupling between L and S. In so-called LS-coupling, the resulting angular momentum is associated with a quantum number $J = L+S$, and the appropriate value of g is given by the Landé factor,

$$g_J \,=\, \frac{3}{2} - \frac{L(L+1)-S(S+1)}{2J(J+1)}\,. \tag{1.4}$$

As it can be seen from Eq. (1.2), for $J = S$ energies corresponding to different projections of the spin m_S are different if the applied magnetic field is not zero. This splitting of the energy levels by the external magnetic field is called the Zeeman effect and the resulting $N = 2S+1$ energy levels are called Zeeman levels. In the case of a single electron there are only two possible $m_S = \pm1/2$ and, therefore, the Zeeman levels split as shown in Fig. 1.1 a. For each value of H_z the transition between Zeeman levels can be achieved by absorption or emission of an electromagnetic quantum $h\nu$ with a proper frequency. This yields a resonance condition

$$E_2 - E_1 \,=\, h\nu \,=\, g\mu_{\mathrm{B}}|\Delta m_S|H_z\,, \tag{1.5}$$

which has to be satisfied. According to the Boltzmann statistics, at a finite temperature and in the thermodynamic equilibrium the higher energy level in Eq. (1.2), $E(m_S = +1/2)$, is less occupied then the lower one, $E(m_S = -1/2)$. Since the transition rates between spin levels generally depend on their population it can be shown that the resulting effect of spin transitions is always absorption.

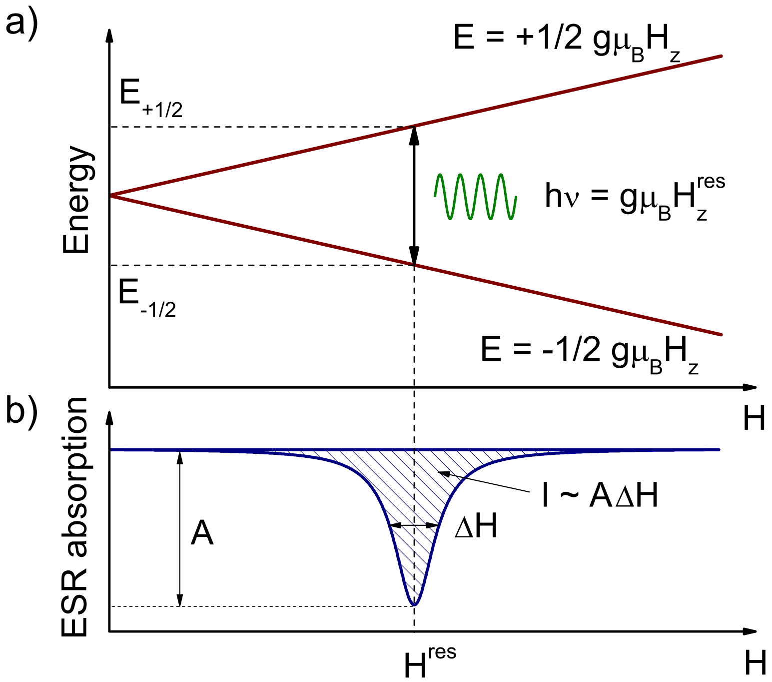

Figure 1.1: a) Zeeman levels for the system $S = 1/2$. At the resonance magnetic field H_{res}, microwave radiation $h\nu$ induces transitions between the energy states. b) ESR absorption line of Lorentzian shape. A is the amplitude at the resonance field H_{res}, ΔH is the linewidth at the half maximum. The absorbed power P is proportional to the integrated intensity of the line, $I \propto A\Delta H$.

For a system with higher spin, the number of Zeeman levels, $N = 2S + 1$, is lager than 2, and the possibilities for transitions between different spin states induced by electromagnetic radiation are restricted by the quantum mechanical selection rules,

$$\Delta L = 0, \quad \Delta S = 0, \quad \Delta m_S = \pm 1 . \tag{1.6}$$

In the case of a free electron $S = 1/2$ the selection rule becomes trivial and, therefore both above described transitions ($-1/2 \leftrightarrows +1/2$) always satisfy $\Delta m_S = \pm 1$.

1.1.1 ESR Spectrum

The resonance condition, given by Eq. (1.5), has two variable parameters which should be of a proper value in order to induce the resonance effect: the applied magnetic field and the frequency of a microwave radiation. Therefore, there are two possibilities to perform ESR measurements. One can either sweep the magnetic field at a constant frequency, or change the frequency at a constant magnetic field. Since sweeping of the magnetic field is technically much easier, most of ESR spectrometers are based on this method. A typical ESR spectrum is obtained by measuring the absorbed microwave power vs. varying applied magnetic field at a constant frequency.

The shape and the parameters of the ESR spectrum (resonance field, line width, intensity) provide the information about the studied spin system (Fig. 1.1 b).

Resonance Field

The resonance field H_{res} provides the information about the g-factor which can be found from

$$g = \frac{h}{\mu_{\text{B}}} \frac{\nu}{H_{\text{res}}} \approx \frac{1}{14} \frac{\nu(\text{GHz})}{H_{\text{res}}(\text{T})} \,. \tag{1.7}$$

Note that Eq. (1.7) is valid for $S = 1/2$ with isotropic g-factor. If the studied system is magnetically anisotropic, a complex angular dependence of the g-factor with respect to the magnetic field direction can occur. If the system has $S \geq 1$, the effects of the ligand field have to be taken into account. In this case, the magnetic anisotropy shifts the resonance magnetic field H_{res} and the g-factor is not determined by Eq. (1.7), but by the slope $\partial\nu/\partial H_{\text{res}}$ of the $\nu(H_{\text{res}})$-dependence at $H_{\text{res}} \to \infty$.

Linewidth and Lineshape

According to the resonance condition (1.5) the expected resonance line should have the form of a sharp peak $f(H) \propto \delta(H - H_{\text{res}})$. However, real measured ESR lines always have a finite width, changing from less than 1 Gauss for free radicals to the order of 10^4 Gauss for strongly interacting magnetic centers. The reason for this is that the excited spin system which is embedded in a matrix will somewhen relax into a thermal equilibrium state, due to the interaction with other spins or with the lattice itself. The lower limit of the ESR linewidth is caused by a finite lifetime τ of the occupied spin state which, according to Heisenberg's relation, is associated with an uncertainty for the transition energy $\Delta E \geq \hbar/\tau$. Thus the natural linewidth of the ESR line is given by

$$\Delta H \propto \frac{\hbar}{g\mu_\mathrm{B}} \frac{1}{\tau} \tag{1.8}$$

and depends on the lifetime of the particular occupied state. Further broadening of the ESR line is associated with the shortening of the lifetime due to different relaxation processes. The relaxation processes will be discussed in more details in section 1.4.3.

A typical lineshape of the absorbed power P as a function of the applied magnetic field H has the form of a Lorentzian (see Fig. 1.1 b),

$$P(H) \propto \frac{\Delta H}{(H - H_\mathrm{res})^2 + (\Delta H)^2} \,. \tag{1.9}$$

This lineshape corresponds to a homogeneous broadening due to fluctuations of the ESR transition frequency. In more complex systems, some interactions of the spins cause inhomogeneous broadening of the ESR line which leads to a change of the lineshape. An inhomogeneous line is composed of spin packets that have slightly different resonance fields. The resulting line shape frequently has a Gaussian character.

ESR Intensity

Since the ESR measures the absolute number of resonating spins, the intensity I of the ESR line is proportional to the local static magnetic susceptibility of the studied system. I corresponds to the integral of the ESR lineshape. In the cases when the lineshape is defined by a Lorentzian or Gaussian shape function the intensity is simply proportional to the product of the amplitude A and the linewidth ΔH [5],

$$I_\mathrm{L} = 1.57\, A\, \Delta H \quad \text{(Lorentzian)}, \tag{1.10}$$

$$I_\mathrm{G} = 1.0643\, A\, \Delta H \quad \text{(Gaussian)}. \tag{1.11}$$

1.2 Many-Electron Ions

In the previous section the free electron scenario was used to illustrate the principles of the electron spin resonance. This scenario is a very simple model which is not sufficient in most of the real cases. In real systems, such as e.g. transition metal ions, electrons contributing to the ESR signals are usually not free but bound to the matter. Instead of single electron spins, there are partially filled electron shells containing in most cases a number of electrons with both spin and orbital angular momentum. Therefore, the investigation of such systems requires to consider entire atoms where some of the electrons give rise to ESR and some do not.

1.2.1 Hund's rules

The character of the ground state of a free ion can be calculated by application of the empirical rules suggested by Hund [6]. They dictate that, in order to find the ground state of an atom with known valence shell configuration, one must:

1. choose the maximum value of S consistent with the Pauli principle;

2. choose the maximum value of L consistent with the Pauli principle and rule 1;

3. choose the total angular momentum $J = |L - S|$ if the shell is less than half-filled, and $J = |L + S|$ if the shell is more than half-filled.

Rules 1 and 2 allow to minimize the intra-atomic Coulomb repulsion among electrons in the same configuration. The third rule takes into account the magnetic (spin-orbit) interactions.

1.2.2 Many-Electron Hamiltonian

Interaction of an electron with the Coulomb potential caused by the nucleus and the other electrons is described by

$$\mathcal{H} = \sum_i \frac{p_i^2}{2m} - \sum_i \frac{Ze^2}{r_i} + \sum_{i>k} \frac{e^2}{r_{ik}} \,. \tag{1.12}$$

With a suitably averaged electrons field with central symmetry, this Hamiltonian results in grouping of the electronic levels into energetically well separated configurations; an example is $3d^3$, a ground state configuration lying $\sim 10^5\,\mathrm{cm}^{-1}$ below the first excited configuration, $3d^2 4s^1$. The residual mutual electrostatic repulsion of the electrons, not represented by a central field, gives rise to the LS (Russel-Saunders) coupling with energy splittings of order $10^4\,\mathrm{cm}^{-1}$ between terms of different L and S built from the same configuration. For example the ground term of $3d^3$, ^4F (by Hund's rules), with $S = 3/2$ and $L = 3$, is $\sim 10^4\,\mathrm{cm}^{-1}$ below the ^4P ($S = 3/2$, $L = 1$) term of the same $3d^3$ configuration [7].

1.2.3 Spin-Orbit Coupling

For a particular electron orbiting around the positively charged nucleus, a magnetic field produced at the electron's site is proportional to the angular momentum of this motion. In general, the resulting interaction between this magnetic field and the spin magnetic moment of the electron (which cannot be calculated analytically, because it depends on the unknown electrostatic potential affecting the electron) can be written in the form

$$\mathcal{H}_{\mathrm{SO}} = \zeta(\mathbf{1}\cdot\mathbf{s}) = \frac{\hbar^2}{2m^2c^2}\left(\frac{1}{r}\frac{\partial V}{\partial r}\right)(\mathbf{1}\cdot\mathbf{s})\,. \tag{1.13}$$

Here, ζ expresses the strength of the coupling. For hydrogen-like ions with only a single electron in the outermost shell the potential V is found as

$$\zeta = \frac{\hbar^2}{2m^2c^2}\frac{Ze^2}{r^3}\,. \tag{1.14}$$

In case of the LS-coupling, the total spin of an incomplete shell S is coupled to its total orbital momentum L,

$$\mathcal{H}_{\mathrm{LS}} = \lambda\,\mathbf{L}\cdot\mathbf{S}\,. \tag{1.15}$$

For ground terms obeying Hund's rules (i.e. terms with maximum spin S), $\lambda = \pm\zeta/2S$ with the upper and lower signs corresponding to electron shells less or more than half-filled, respectively. This splits a given term into a multiplet of levels with different values of J. The components of the multiplet are split by $\sim 10^2\,\mathrm{cm}^{-1}$ for $3d$ electrons and by larger amounts for ions with larger atomic numbers [7].

1.2.4 Crystal Field Symmetry

Crystal field influence on the magnetic properties of the paramagnetic ion is caused by the electrostatic interactions between the electrons of the ion and the electric charge distribution of the surrounding non-magnetic ions (ligands). The crystal field potential is generally weaker than the intra-atomic electron-electron interactions, but in some cases may be comparable with the spin-orbit coupling forces. For example, it is weak in rare earth elements and actinides, since the $4f$ and $5f$ shells are localized near the core and screened from the ligands by the outer shell electrons; and it is stronger than the spin-orbit coupling, but still

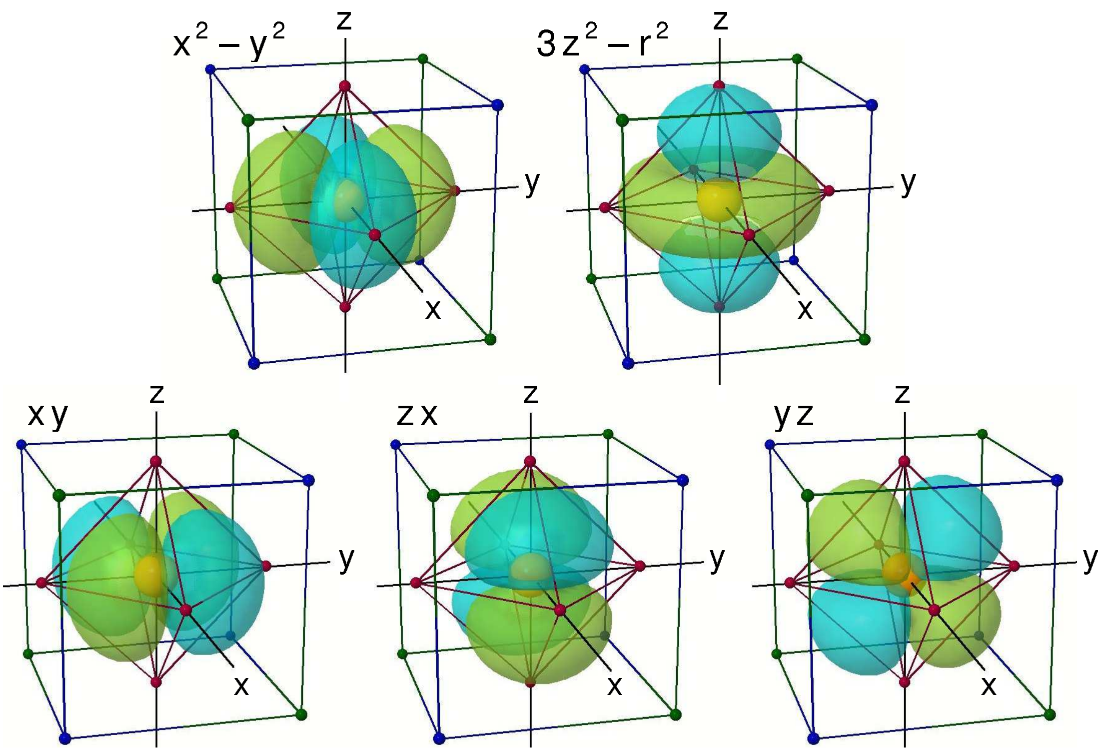

Figure 1.2: $3d$ orbitals in the cubic symmetry ligand environment. Top: e_g orbitals, in the octahedral case pointing towards ligands; bottom: t_{2g} orbitals pointing between the ligands (see text for the details).

weaker than the intra-atomic Coulomb interactions in the case of the iron-group elements.

Cubic Symmetry

One of the most important symmetry groups in solid state physics is the octahedral group O_h. The group characterizes, for example, the symmetry of the crystal field produced by six oxygen ions surrounding a central metal ion. The same group would describe a symmetry of a crystal field produced by eight atoms situated at the corners of a cube. Though the cube and the octahedron are different geometric objects, their symmetry (and thus symmetry group) is the same (see Fig. 1.2), so called “cubic symmetry”.

The details of how the energy levels of the paramagnetic ion will be split by the crystal field depend on the symmetry of the local environment of the ion. As an example, one can consider the case of a single $3d$ electron: $S = 1/2$, $L = 2$. According to the Hund’s rules, $J = 3/2$ for the ground state multiplet, which is

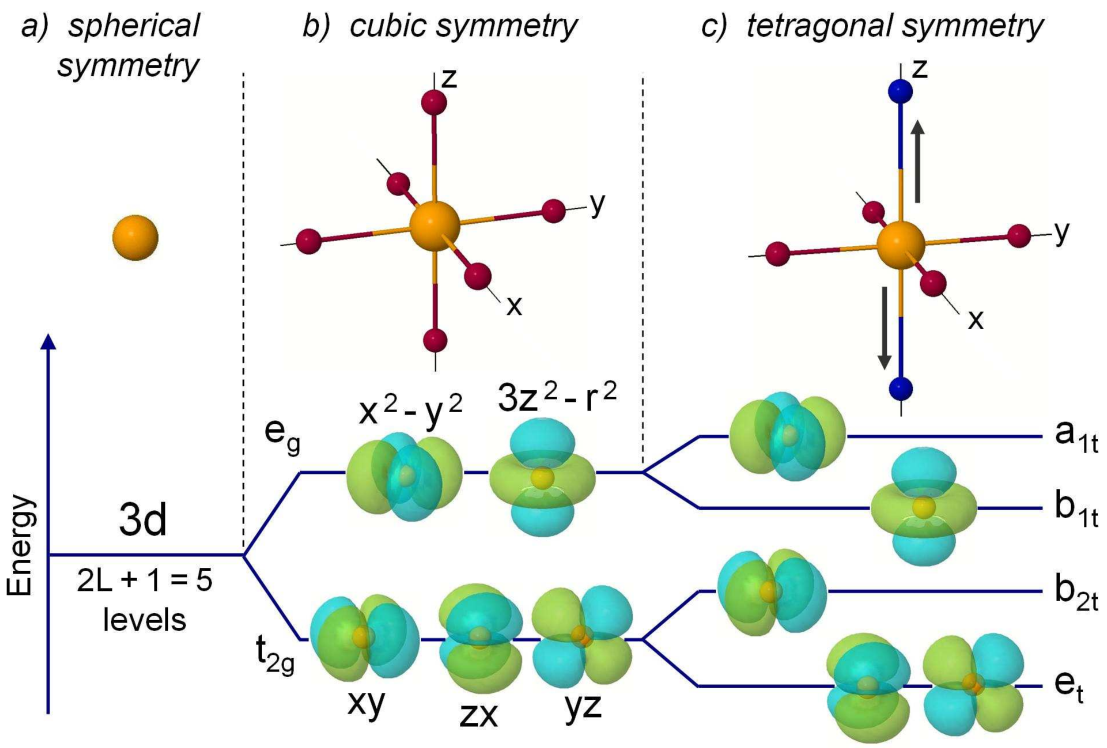

Figure 1.3: 3d-shell energy levels for different crystal field symmetries. a)Spherical symmetry (e.g. free ion). Five orbital states are degenerate. b) Cubic symmetry (e.g. octahedral environment). The degeneracy is partially lifted. c) Tetragonal symmetry further lifts the degeneracy of the energy states.

the $^2D_{3/2}$ term. Therefore, this term has a 5-fold orbital degeneracy (Fig. 1.3 a). In cartesian coordinates, these five wave-functions can be written as products of a radial function $f_2(r)$ and linearly independent polynomials: $X = yz$, $Y = zx$, $Z = xy$, $\Phi_1 = x^2 - y^2$, and $\Phi_2 = 3z^2 - r^2$ [8]. The analysis of effects of all 48 possible symmetry operations of a cube (or, which is the same, of an octahedron) upon the five-dimensional set of d functions (X, Y, Z, Φ_1, Φ_2) yields that the first triplet of functions spans a subspace which transforms into itself. The same is true for the doublet. Both subspaces are therefore closed under this group. In the language of the group theory, the original 5-dimensional subspace spans a reducible representation of the cubic point group which decomposes into, or reduces to, two irreducible representations: a 3-dimensional one, called T_2 and a 2-dimensional one, called E (also commonly called t_{2g} and e_g levels).

The group theory can provide the information about the number and the degeneracy of the levels in a given set of states. However, it can not say anything about the size of the splitting and the order of the levels. In order to obtain this information the details of the Hamiltonian have to be specified. The term describing the crystal field hamiltonian can be written as

$$\mathcal{H}_{\mathrm{CF}} = \sum_{j=1}^{N} \frac{q_j}{|\mathbf{R}_j - \mathbf{r}|} \,. \tag{1.16}$$

Here the set of N ligand ions of charges q_j located at points $\mathbf{R}_j$ produces the potential at the point $\mathbf{r}$. For the electrostatic approximation, in which the ligands are substituted by point charges, a rather simple calculation indicates which of the spin levels has the lowest energy [8]. For a single $3d$ electron, in the octahedral coordination the triplet t_{2g} is the lowest level, while in a body-centered cubic (b.c.c.) coordination or in the tetrahedral case the doublet e_g is the lowest. The splitting of the energy levels in the octahedral crystal field is schematically shown in Fig. 1.3 b. In practice, this can be easier understood as the following (see also Fig. 1.2): the orbitals of the central ion directed along the axes containing ligand ions have higher energy than those directed away from the ligands.

Lower Symmetry Crystal Field

Distortion of the octahedral coordination of the central ion along one of the main axes (for example, z-axis, as shown in Fig. 1.3 c) leads to the lowering of the symmetry from the cubic to tetragonal. In this case, in addition to the "octahedral" splitting of the energy levels, the e_g level splits into the a_{1t} and the b_{1t} levels, while t_{2g} splits further into the twofold degenerate e_t and the b_{2t}-level (Fig. 1.3 c). This axial distortion of the crystal field gives rise to the axial magnetic anisotropy for the paramagnetic center, which is essentially absent in the case of the ideal octahedron. The magnetic anisotropy will be discussed in the section 1.3.1 in more details. Further reduction of the symmetry can be achieved by an additional distortion in xy-plane, such as concurrent compression and elongation of the ligands on the x- and y-axis. This distortion leads to the orthorhombic symmetry and eventually splits the remaining degeneracy of the twofold e_t level.

1.2.5 Quenching of the Orbital Momentum

Expected magnetic ground states for a free $3d$ ion can be calculated according to the Hund's rules described in the section 1.2.1. However, the values of the predicted effective magnetic moment given by

$$\mu_{\text{eff}} = g\sqrt{J(J+1)}\,, \tag{1.17}$$

were the g-factor is the Landé factor Eq. (1.22), do not always agree with experiments. For example, the Ni^{2+} ion with $3d^8$ configuration, according to the Hund's rules, has $S = 1$ and $L = 3$, and therefore the quantum number of the total angular momentum $J = 4$. The effective magnetic moment in this case, according to Eq. (1.17), is about 5.6, while the experimentally observed value from susceptibility measurements is usually about 3.1. The reason for this difference is quenching of the orbital moment of transition metal ions embedded in a crystalline environment.

As it was discussed in the previous section, the orthorhombic symmetry of the crystal field splits $3d$ levels and reduces the degeneracy from 5-fold (free ion) to 1-fold for all five energy states. In this case, all irreducible representations become one-dimensional and the wave functions $|\psi\rangle$ are essentially real. This leads to $\langle\psi|L^z|\psi\rangle = -i\hbar\langle\psi|\partial/\partial\phi|\psi\rangle$ being purely imaginary. On the other hand, a measurable quantity (an observable) should be real. These both statements can be true only if $\langle\psi|L^z|\psi\rangle = 0$ which means that the orbital momentum is fully quenched. In the case of cubic (octahedral) symmetry, the energy levels are split into two groups: the 2-fold degenerate e_g and the 3-fold degenerate t_{2g} states. For the e_g levels, independently from the actual choice of the basis, all the three components of $\mathbf{L}$ vanish and, consequently, the orbital moment of the e_g electrons is quenched [9]. However, this is not the case for t_{2g} levels, where the wave functions can remain complex. The orbital momentum thus is defined by 3-fold degeneracy of the t_{2g} state and can be maximum equal to $L^z = 1$. This effect is called partial quenching of the orbital momentum. Coming back to the Ni^{2+} ($3d^8$) example, one can see that in the case of an octahedral crystal field the t_{2g} levels are completely filled giving no contribution to the orbital momentum, as well as two unpaired electrons in the e_g levels. Hence, the orbital momentum of the Ni^{2+} ion is fully quenched and therefore the observed effective magnetic moment is given only by the spin contribution.

1.2.6 Electron Zeeman Interaction

The interaction between an ion with a total spin $\mathbf{S}$ and total orbital momentum $\mathbf{L}$ and an external magnetic field $\mathbf{H}$ is described by the Zeeman Hamiltonian

$$\mathcal{H}_{\mathrm{Z}} = \mu_{\mathrm{B}}\,\mathbf{H}\cdot(\mathbf{L}+g_e\mathbf{S})\,. \tag{1.18}$$

Here, $\mu_{\mathrm{B}} = e\hbar/2m_e$ is the Bohr magneton and g_e is the electron g-factor (Eq. (1.3)). In the case of the LS-coupling, the Hamiltonian (1.18) can be written in terms of the total angular momentum $\mathbf{J} = \mathbf{L} + \mathbf{S}$,

$$\mathcal{H}_{\mathrm{Z}} = g\mu_{\mathrm{B}}\,\mathbf{H}\cdot\mathbf{J}\,. \tag{1.19}$$

In this case the resulting electronic magnetic moment is

$$\boldsymbol{\mu} = -g_J\mu_{\mathrm{B}}\mathbf{J}\,, \tag{1.20}$$

and g is given as

$$g_J = \frac{J(J+1)(g_L+g_e)+[L(L+1)-S(S+1)](g_L-g_e)}{2J(J+1)}\,, \tag{1.21}$$

which reduces to the Landé factor

$$g_J = \frac{3}{2} - \frac{L(L+1)-S(S+1)}{2J(J+1)} \tag{1.22}$$

if $g_L = 1$, $g_e = 2$ exactly.

Depending on the symmetry of the system the g-factor can become anisotropic. Usually, the $\mathbf{g}$ tensor's principal axes frame is considered as the crystal field frame and all interaction tensors are referred to this frame. Thus, for cubic symmetry, $g_x = g_y = g_z = g$; for axial symmetry, $g_x = g_y = g_\perp$ and $g_z = g_\|$; and for orthorhombic symmetry, $g_x \neq g_y \neq g_z$. In general, for systems with low symmetry the $\mathbf{g}$ tensor may become asymmetric [10].

In the case of a low crystal field symmetry, for a non-degenerate electronic ground state, the orbital angular momentum is quenched, $L = 0$. The deviation of the principal values of $\mathbf{g}$ from the value g_e of the free electron and the orientation dependence of the Zeeman term are caused by an interaction of the ground state and excited states, which admixes the orbital angular momentum L from the excited states to the ground state. In this case the $\mathbf{g}$ tensor is given as $\mathbf{g} = g_e\cdot\mathbf{1} + 2\lambda\boldsymbol{\Lambda}$, where $\boldsymbol{\Lambda}$ is a symmetric tensor with the elements

$$\mathbf{\Lambda}_{ij} = \sum_{n \neq 0} \frac{\langle \psi_0 | \mathbf{L}_i | \psi_n \rangle \langle \psi_n | \mathbf{L}_j | \psi_0 \rangle}{E_0 - E_n} \,. \tag{1.23}$$

The wave function ψ_0 describes the ground state with the energy E_0 occupied by the unpaired electron and ψ_n denotes the n^{th} excited state with the energy E_n. The closer the excited state to the ground state and the larger the spin-orbit coupling are, the larger becomes the deviation of the g principal values from g_e.

1.3 Effective Spin Hamiltonian

The spin Hamiltonian approach is widely used in various spectroscopies in order to simplify the interpretation and classification of obtained spectra without using fundamental theories [11]. This approach eliminates all the orbital coordinates needed to define the system, and replaces them with spin coordinates, taking advantages of the symmetry properties of the system [7]. In respect to the ESR spectroscopy, the energies of states within the ground state of a magnetic center with an effective electron spin S can be described by the effective spin Hamiltonian

$$\mathcal{H} = \mathcal{H}_{\mathrm{Z}} + \mathcal{H}_{\mathrm{ZFS}} + \mathcal{H}_{\mathrm{HF}} \,, \tag{1.24}$$

where $\mathcal{H}_{\mathrm{Z}}$ is the electron Zeeman interaction; $\mathcal{H}_{\mathrm{ZFC}}$ is the zero field splitting caused by the anisotropic crystal field; and $\mathcal{H}_{\mathrm{HF}}$ is the hyperfine interaction between the electron spin and surrounding nuclear spins I_i. In the following, each of these terms will be described in detail. Furthermore, it will be shown how the parameters of the spin Hamiltonian can be directly measured by means of the ESR spectroscopy.

1.3.1 Zeeman Term and Zero-Field Splitting

The first term in the effective spin Hamiltonian represents the electronic Zeeman interaction. By analogy with Eq. (1.19) it can be written in the form

$$\mathcal{H}_{\mathrm{Z}} = g\mu_{\mathrm{B}}\, \mathbf{H} \cdot \mathbf{S} \,. \tag{1.25}$$

If the effective spin Hamiltonian contains only the Zeeman term, in a zero external magnetic field all $2S+1$ levels, corresponding to different S_z values, have the same energy.

For systems with $S > 1/2$, the zero field splitting of the energy levels can appears due to the lower symmetry of the crystal field. This effect is expressed in the phenomenological Hamiltonian

$$\mathcal{H}_{\mathrm{ZFS}} = \mathbf{S} \cdot \mathbf{D} \cdot \mathbf{S}\,, \tag{1.26}$$

where $\mathbf{D}$ is a real symmetric tensor. Therefore Eq. (1.26) can be written in the form

$$\mathcal{H}_{\mathrm{ZFS}} = D_{xx}S_x^2 + D_{yy}S_y^2 + D_{zz}S_z^2\,. \tag{1.27}$$

Taking

$$D = D_{zz} - D_{xx}/2 - D_{yy}/2\,; \quad E = (D_{xx} - D_{yy})/2\,, \tag{1.28}$$

Eq. (1.27) can be transformed to

$$\mathcal{H}_{\mathrm{ZFS}} = DS_z^2 + E(S_x^2 - S_y^2)\,, \tag{1.29}$$

and by subtracting the constant $DS(S+1)/3$ one obtains

$$\mathcal{H}_{\mathrm{ZFS}} = D(S_z^2 - S(S+1)/3) + E(S_x^2 - S_y^2)\,. \tag{1.30}$$

With respect to the Hamiltonian (1.29), the advantage of (1.30) is that the trace of its tensor $\mathrm{Tr}\,\mathcal{H} = 0$. The effect of the Hamiltonian (1.29) or (1.30) is a splitting of the $2S + 1$ levels even in the absence of an external magnetic field (zero-field splitting). In the case of cubic (octahedral) symmetry $D_{xx} = D_{yy} = D_{zz}$, and therefore, according to (1.28), $D = E = 0$ and $\mathcal{H}_{\mathrm{ZFS}} = 0$. For the axial (tetragonal) symmetry, $D_{xx} = D_{yy}$, and therefore $E = 0$, so that only the D parameter is needed to describe the energy levels of the S multiplet.

In the following, the case of the Ni^{2+} ion in an axially distorted octahedral surrounding will be discussed. As it was already mentioned before, the Ni^{2+} ion has two unpaired electrons in the e_g energy level which result in a total spin $S = 1$. If the external magnetic field is applied along the anisotropy axis z, the eigenvalues of the Hamiltonian

$$\mathcal{H} = \mathcal{H}_{\mathrm{Z}} + \mathcal{H}_{\mathrm{ZFS}} = g\mu_{\mathrm{B}}H_zS_z + D(S_z^2 - S(S+1)/3) \tag{1.31}$$

can be written as $E_0 = -2D/3$ and $E_{\pm1} = \pm g\mu_{\mathrm{B}}H_z + D/3$. The corresponding energy level scheme is shown in Fig. 1.4 a. In such a situation the resonance conditions, Eq. (1.5), for the two allowed ESR transitions ($|-1\rangle \rightleftarrows |\,0\,\rangle$ and $|\,0\,\rangle \rightleftarrows$

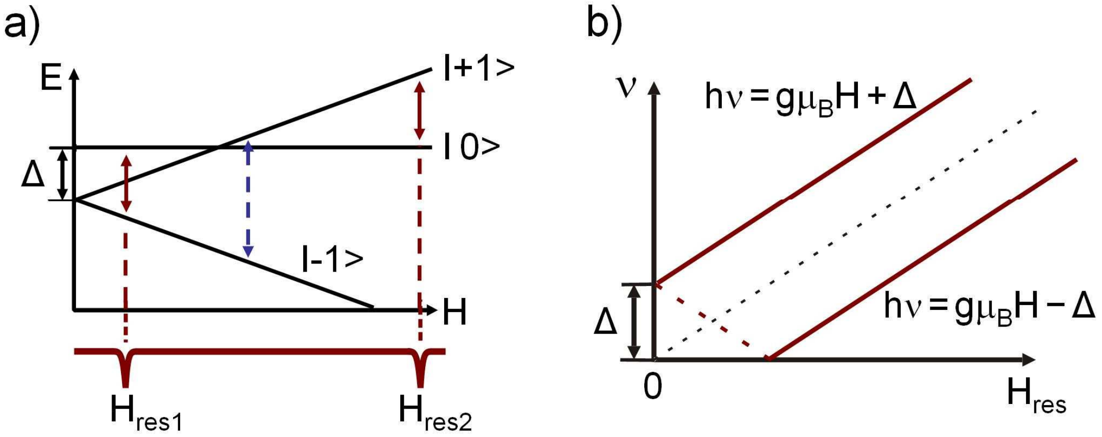

Figure 1.4: a) Energy level scheme for the Ni^{2+} ion with $S = 1$ ($D < 0$). The splitting of the levels is caused by the spin-orbit coupling and the Zeeman interactions (when $H \neq 0$). Red arrows indicate the allowed ESR transitions. Below the energy level scheme the corresponding ESR spectrum is shown. Blue dashed arrow indicates the "forbidden" ESR transition (see text for detailes). b) Expected frequency vs. resonance magnetic field $\nu(H_{\mathrm{res}})$ diagram for the two allowed ESR transitions.

$|+1\rangle$; $\Delta m_s = \pm 1$) are different, and in the ESR spectrum one can observe two separate absorption lines (Fig. 1.4 a). The frequency vs. resonance field $\nu(H_{\mathrm{res}})$ dependencies (so-called resonance branches) for these ESR lines are sketched in Fig. 1.4 b. The slope of the resonance branches is proportional to the g-factor. The frequency at which the upper line crosses the zero field is proportional to the anisotropy energy gap Δ which is associated with the anisotropy parameter D as $\Delta = |D|(S^2 - (S-1)^2)$.

Depending on the sign of D either E_0 or $E_{\pm 1}$ takes the lowest position yielding either singlet ("easy plain") or bistable magnetic ("easy axis") ground state, respectively. In the ESR spectrum, at a finite temperature, the sign of D reflects in different relative intensities of the absorption lines. Thus, for $D < 0$ (see Fig. 1.4 a), the energy level $|-1\rangle$ is more populated than $|+1\rangle$, according to Boltzmann distribution. Therefore, the probability of the leftmost transition is higher and the intensity is larger. The same is valid for the rightmost transition in the case of $D > 0$.

In general, for an arbitrary angle θ between the anisotropy axis z and magnetic field direction z' the Hamiltonian is given as

$$\mathcal{H} = \mathcal{H}_{\mathrm{Z}} + \mathcal{H}_{\mathrm{ZFS}} = g\mu_{\mathrm{B}}H_{z'}S_{z'} + D(S_z^2 - S(S+1)/3) \tag{1.32}$$

The energy states for such a system can be found as eigenvalues by the diagonalization of the Hamiltonian matrix

$$\begin{array}{|c|c|c|c|}
\hline
S_{z'} & -1 & 0 & +1 \\
\hline
-1 & \begin{array}{c}\frac{1}{6}\,D\,(3\cos^2\theta-1)\\ -g\mu_{\mathrm{B}}H\end{array} & \frac{\sqrt{2}}{4}\,D\sin 2\theta & \frac{1}{2}\,D\sin^2\theta \\
\hline
0 & \frac{\sqrt{2}}{4}\,D\sin 2\theta & -\frac{1}{3}\,D\,(3\cos^2\theta-1) & -\frac{\sqrt{2}}{4}\,D\sin 2\theta \\
\hline
+1 & \frac{1}{2}\,D\sin^2\theta & -\frac{\sqrt{2}}{4}\,D\sin 2\theta & \begin{array}{c}\frac{1}{6}\,D\,(3\cos^2\theta-1)\\ +g\mu_{\mathrm{B}}H\end{array} \\
\hline
\end{array} \tag{1.33}$$

Non-diagonal elements of this matrix yield mixing of the energy states. In this case, the eigenfunctions do not simply correspond to different projections of the spin (pure states, as it was for $\theta = 0$, Eq. (1.31)), but each of them is a linear combination of all pure states. This mixing of the energy states yields a finite probability of so-called "forbidden" transitions with $\Delta m_s = \pm 2$ (blue dashed arrow in Fig. 1.4 a) which can be observed in the ESR spectrum as an absorption line with a doubled slope of the resonance branch, $h\nu = g\mu_{\mathrm{B}}H|\Delta m_s| = 2g\mu_{\mathrm{B}}H$.

1.3.2 Hyperfine Interaction

The last term in the Hamiltonian (1.24) describes the interactions of the electronic spin S with magnetic nuclei which may be present in the system. These interactions are called hyperfine and usually described by

$$\mathcal{H}_{\mathrm{HF}} = \mathbf{S}\cdot\mathbf{A}\cdot\mathbf{I}\,, \tag{1.34}$$

where $\mathbf{I}$ is the nuclear spin operator and $\mathbf{A}$ is a tensor describing the electron-nucleus magnetic interaction. By a suitable choice of axes, which usually means the principal axes of the g-factor, Eq. (1.34) can be reduced to the form

$$\mathcal{H}_{\mathrm{HF}} = A_{xx}S_xI_x + A_{yy}S_yI_y + A_{zz}S_zI_z\,. \tag{1.35}$$

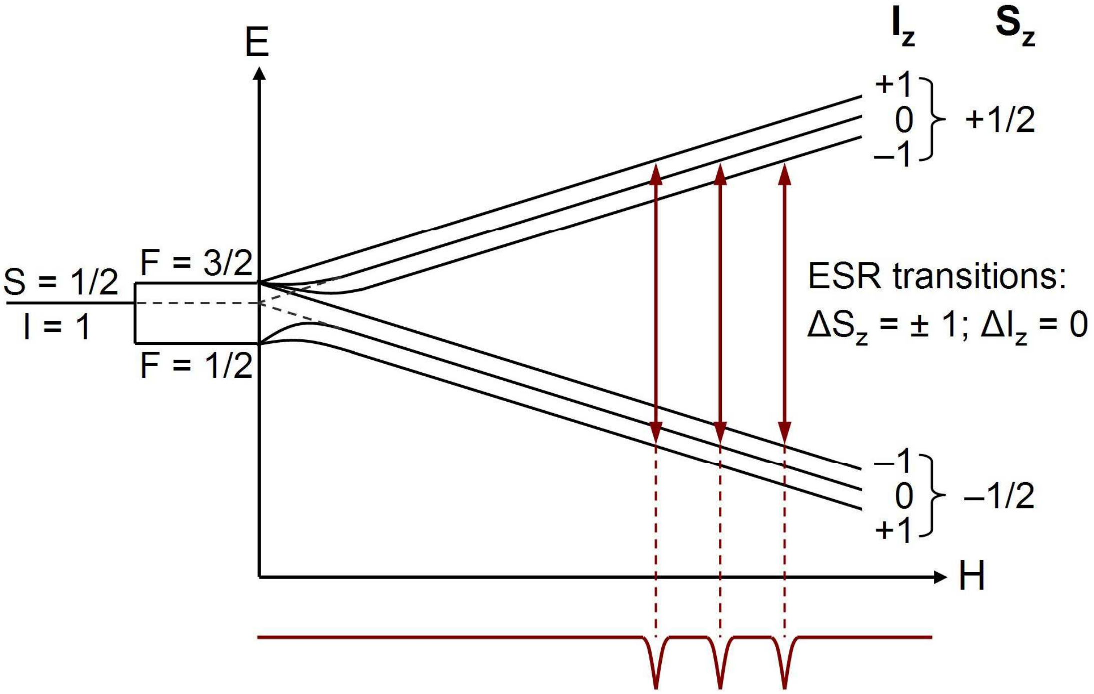

Figure 1.5: Energy level scheme and allowed ESR transitions for the case of a hyperfine coupling between $S = 1/2$ and $I = 1$ with no anisotropy.

In the case of an axial symmetry, $A_{xx} = A_{yy} = A_\perp$ and $A_{zz} = A_\parallel$. For the cubic symmetry, $A_{xx} = A_{yy} = A_{zz} = A$ and the Hamiltonian can be written in the form

$$\mathcal{H}_{\mathrm{HF}} = A\,\mathbf{S}\cdot\mathbf{I}\,. \tag{1.36}$$

In order to illustrate the hyperfine splitting, in the following, the case of $S = 1/2$ and $I = 1$ with no anisotropy will be discussed. The corresponding energy levels are shown in Fig. 1.5. In zero magnetic field, the six levels split into a quadruplet corresponding to a total angular spin $F = 3/2$ and a doublet $F = 1/2$. In strong magnetic fields ($A \ll g\mu_{\mathrm{B}}H$), the levels diverge linearly and in first approximation are given by

$$E = g\mu_{\mathrm{B}}HS_z + AS_zI_z\,, \tag{1.37}$$

where $S_z = \pm 1/2$ and $I_z = +1$, 0 or -1. The allowed transitions, corresponding to the electron spin resonance without change in the nuclear spin orientation, are shown by arrows in Fig. 1.5. These transitions are equally spaced at

$$h\nu = g\mu_{\mathrm{B}}H + AI_z \tag{1.38}$$

and equally intense at all ordinary temperatures ($kT \gg A$), since the three (or, more generally, $2I + 1$) nuclear orientations are equally probable.

1.3.3 Spin-Spin Exchange Coupling

A system of two magnetic centers can be described using the formalism of the effective spin Hamiltonian (1.24) by summing the Hamiltonians for the non-interacting centers and adding an interaction term. The simplest form of the interaction between two spins is given by

$$\mathcal{H}_{\mathrm{SS}} = \mathbf{S}_1 \cdot \mathbf{J_{12}} \cdot \mathbf{S}_2 \,, \tag{1.39}$$

where $\mathbf{S}_1$ and $\mathbf{S}_2$ are the spin operators for center 1 and 2, respectively, and $\mathbf{J_{12}}$ is a tensor describing the spin-spin magnetic interaction. After the decomposition of $\mathbf{J_{12}}$ into different contributions, Eq. (1.39) can be written in the form

$$\mathcal{H}_{\mathrm{SS}} = J_{12}\mathbf{S}_1 \cdot \mathbf{S}_2 + \mathbf{S}_1 \cdot \mathbf{D_{12}} \cdot \mathbf{S}_2 + \mathbf{d}_{12} \cdot (\mathbf{S}_1 \times \mathbf{S}_2) \,. \tag{1.40}$$

The first term is the isotropic, the second therm is the anisotropic, and the last term is the antisymmetric contribution to the spin-spin interaction. The isotropic first term tends to keep the spins either parallel or antiparallel to each other; the third term tends to cant them by 90 °. The second term tends to orient the spins along a given orientation in the space [11].

In many cases the first term can be considered as dominant, introducing the other terms as perturbation. Under this conditions the total spin $\mathbf{S} = \mathbf{S}_1 + \mathbf{S}_2$ remains a good quantum number with values according to

$$|S_1 - S_2| \leq S \leq S_1 + S_2 \,. \tag{1.41}$$

Every allowed S represents a spin multiplet with energies of states given by

$$E_S = \frac{1}{2} J_{12} \left[S(S+1) - S_1(S_1+1) - S_2(S_2+1) \right] . \tag{1.42}$$

$J_{12} > 0$ corresponds to an antiferromagnetic (AFM) and $J_{12} < 0$ to a ferromagnetic (FM) exchange coupling between S_1 and S_2.

1.4 Electron Spin Dynamics

This section will concentrate on dynamic effects in electron spin systems, such as relaxation processes and spin echo. One of the efficient methods for studying the dynamic properties of the electron spins is pulse ESR. In general, the basic concepts of pulse ESR are rather similar to those of pulse nuclear magnetic resonance (NMR) spectroscopy [12]. However, there is a number of modifications which have to be applied to the NMR theory in order to describe the dynamics of the electron spins. These modifications have their origin in major differences between electron and nuclear spin systems, for example in the relative size of the magnetic interactions and in the relaxation times which are approximately three orders of magnitude shorter in ESR than in NMR [10].

A rigorous theory of ESR must be based on quantum mechanics, because spins are quantum objects and involved in the processes on a microscopic level. However, experiments are usually done on ensembles of electron spins. The macroscopic magnetization of the sample due to these spins is created and manipulated by applying external static or time-dependent magnetic fields. Thus, one may expect that at least some of the basic aspects of such experiments can be understood in a classical picture.

1.4.1 Classical Interpretation of Resonance Phenomenon

The motion of the magnetization vector $\mathbf{M}$ can be treated in analogous way to that of a single classical magnetic moment, as long as relaxation is neglected. In the thermal equilibrium, $\mathbf{M}$ is aligned parallel to the external static magnetic field $\mathbf{H}_0$. The direction of $\mathbf{H}_0$ is chosen as the z^{L}-axis of the laboratory frame with coordinates x^{L}, y^{L}, z^{L}.

In the presence of an arbitrary and possibly time-dependent magnetic field, the equation of motion of the magnetization vector is given by

$$\frac{d\mathbf{M}(t)}{dt} = -\frac{g\mu_{\mathrm{B}}}{\hbar}\,\mathbf{M}(t) \times \mathbf{H}(t)\,. \tag{1.43}$$

For the static magnetic field $\mathbf{H}(t) = \mathbf{H}_0$, the magnetization $\mathbf{M}$ is invariant if it is aligned along the z^{L}-axis. Otherwise, there is always a torque perpendicular to $\mathbf{M}$. In this case, only the angle θ between $\mathbf{M}$ and z^{L}-axis and the length of $\mathbf{M}$ are invariant, and the vector $\mathbf{M}$ precesses on a cone about $\mathbf{H}_0$ (Fig. 1.6 a). The frequency of precession in angular frequency units

$$\omega = \frac{g\mu_{\mathrm{B}} H_0}{\hbar} \tag{1.44}$$

is called the Larmor frequency. This picture of precession, which is valid for the magnetization vector $\mathbf{M}$, should not be taken literally for a single spin which is a quantum object.

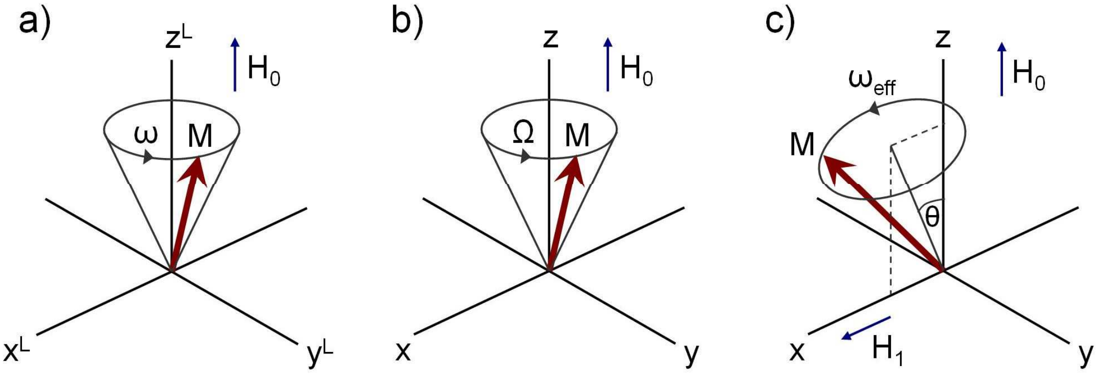

Figure 1.6: Motion of the magnetization vector. a) Free precession about the static magnetic field direction with the angular frequency ω in the laboratory frame. b) Free precession with the precession frequency $\Omega = \omega - \omega_{\mathrm{mw}}$ in the rotating frame. c) Nutation of the magnetization vector in the presence of off-resonant MW radiation (see text for details).

Application of a microwave (MW) radiation in ESR technics provides an additional time-dependent circularly polarized magnetic field $\mathbf{B}_1$ with components

$$\begin{aligned} H_{1x^{\mathrm{L}}}(t) &= H_1 \cos(\omega_{\mathrm{mw}} t)\,, \\ H_{1y^{\mathrm{L}}}(t) &= H_1 \sin(\omega_{\mathrm{mw}} t)\,, \\ H_{1z^{\mathrm{L}}}(t) &= 0\,. \end{aligned} \tag{1.45}$$

Since $\mathbf{M}$ is continuously precessing about $\mathbf{H}_0$ in the same sense as $\mathbf{H}_1$, it is easier to visualize the time dependence of $\mathbf{M}$ in a rotating coordinate frame. The rotating frame has coordinates x, y, z, the z-axis parallel to the z^{L}-axis of the laboratory frame, and the x-axis parallel to $\mathbf{H}_1$ direction. This frame is rotating about the z^{L}-axis with the frequency ω_{mw} of $\mathbf{H}_1$. In such a frame, the equations of motion for $\mathbf{M}$ are given by

$$\begin{aligned} \frac{\mathrm{d}M_x}{\mathrm{d}t} &= -(\omega - \omega_{\mathrm{mw}})M_y = -\Omega M_y\,, \\ \frac{\mathrm{d}M_y}{\mathrm{d}t} &= (\omega - \omega_{\mathrm{mw}})M_x - \frac{g\mu_{\mathrm{B}}H_1}{\hbar}M_z = \Omega M_x - \omega_1 M_z\,, \\ \frac{\mathrm{d}M_z}{\mathrm{d}t} &= \frac{g\mu_{\mathrm{B}}H_1}{\hbar}M_y = \omega_1 M_y\,. \end{aligned} \tag{1.46}$$

In the absence of MW radiation ($\mathbf{H}_1 = 0$), $\mathbf{M}$ precesses about the z-axis with the resonance offset frequency (Fig. 1.6 b)

$$\Omega = \omega - \omega_{\mathrm{mw}}\,. \tag{1.47}$$

In the presence of MW radiation, there is an additional precession about the $\mathbf{H}_1$ direction with the frequency

$$\omega_1 \;=\; \frac{g\mu_{\mathrm{B}}H_1}{\hbar}\,. \tag{1.48}$$

A superposition of both precessions leads to a nutation about an effective magnetic field (Fig. 1.6 c). The axis of the effective field is inclined by an angle

$$\theta \;=\; \arctan\left(\frac{\omega_1}{\Omega}\right) \tag{1.49}$$

with respect to the static field direction z, and the nutation frequency is given by

$$\omega_{\mathrm{eff}} \;=\; \sqrt{\Omega^2 + \omega_1^2}\,. \tag{1.50}$$

For the resonance case where $\omega_{\mathrm{mw}} = \omega$ and thus $\Omega = 0$, the magnetization vector is invariant in the absence of MW radiation. However, even a weak MW field induces a precession about the rotating frame x-axis. On the other hand, far off-resonant radiation ($\Omega \gg \omega_1$) does not significantly influence the motion of $\mathbf{M}$, as $\theta \approx 0$ and $\omega_{\mathrm{eff}} \approx \Omega$ in this case.

Note that in most ESR experiments a linearly polarized MW field $H_{1x^{\mathrm{L}}}(t) = 2H_1\cos(\omega_{\mathrm{mw}}t)$, $H_{1y^{\mathrm{L}}}(t) = H_{1z^{\mathrm{L}}}(t) = 0$ is applied. Experimentally, such a field is much easier to generate. A linearly polarized field can be considered as a superposition of a right-hand and left-hand rotating circularly polarized fields, $\mathbf{H}_1^{\mathrm{r}}$ and $\mathbf{H}_1^{\mathrm{l}}$, with

$$\begin{aligned}
H^{\mathrm{r}}_{1x^{\mathrm{L}}}(t) \;&=\; H^{\mathrm{l}}_{1x^{\mathrm{L}}}(t) \;=\; H_1\cos(\omega_{\mathrm{mw}}t)\,,\\
H^{\mathrm{r}}_{1y^{\mathrm{L}}}(t) \;&=\; -H^{\mathrm{l}}_{1y^{\mathrm{L}}}(t) \;=\; H_1\sin(\omega_{\mathrm{mw}}t)\,,\\
H^{\mathrm{r}}_{1z^{\mathrm{L}}}(t) \;&=\; H^{\mathrm{l}}_{1z^{\mathrm{L}}}(t) \;=\; 0\,.
\end{aligned} \tag{1.51}$$

In the rotating frame, $H^{\mathrm{r}}_{1x} = H_1$, $H^{\mathrm{r}}_{1y} = H^{\mathrm{r}}_{1z} = 0$ and $H^{\mathrm{l}}_{1x} = H_1\cos(2\omega_{\mathrm{mw}}t)$, $H^{\mathrm{l}}_{1y} = H_1\sin(2\omega_{\mathrm{mw}}t)$, $H^{\mathrm{l}}_{1z} = 0$, and thus only the right-hand polarized field $\mathbf{H}_1^{\mathrm{r}}$ can be resonant, the left-hand polarized field $\mathbf{H}_1^{\mathrm{l}}$ is off-resonant by approximately $2\omega_{\mathrm{mw}}$. Since usually $2\omega_{\mathrm{mw}} \gg \omega_1$, $\mathbf{H}_1^{\mathrm{l}}$ can be neglected and, therefore, Eq. (1.46)-(1.50) can be also applied for a linearly polarized MW field.

1.4.2 Effect of a MW Pulse

The effect of a MW pulse on an electron spin system can be easier understood in the simple case of resonance radiation ($\Omega = 0$) with the MW field direction

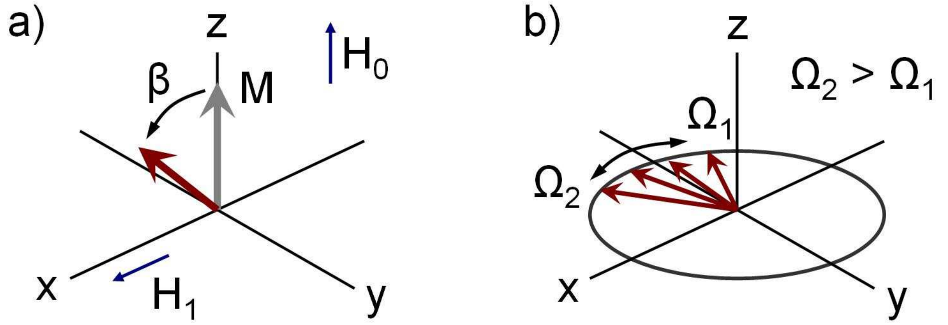

Figure 1.7: a) The effect of a resonant MW pulse along the x-axis on the magnetization vector $\mathbf{M}$. During the pulse the magnetization vector is rotated by a flip angle β about the x-axis. b) Defocusing of the transverse magnetization due to the different resonance offset Ω of different spin packets.

along the rotating frame x-axis. A MW pulse of length t_p starts at time $t = 0$ and ends at $t = t_\mathrm{p}$. During such a pulse, the magnetization vector $\mathbf{M}$, which was in thermal equilibrium at $t = 0$ ($M_z = M_0$, $M_x = M_y = 0$), precesses about the x-axis and at $t = t_\mathrm{p}$ becomes

$$\begin{aligned} M_x &= 0\,, \\ M_y &= -M_0 \sin\left(\omega_1 t_\mathrm{p}\right), \\ M_z &= M_0 \cos\left(\omega_1 t_\mathrm{p}\right), \end{aligned} \tag{1.52}$$

This means that during such a resonant pulse the magnetization vector $\mathbf{M}$ is rotated by a flip angle

$$\beta = \omega_1 t_\mathrm{p} \tag{1.53}$$

about the x-axis as shown in Fig. 1.7 a. Thus in the resonant case any desired rotation of $\mathbf{M}$ can be realized by appropriately timed and phased MW pulses. This is also valid for small resonance offsets $\Omega_S \ll \omega_1$, where the Larmor precession about $\mathbf{H}_0$ may be neglected during the pulses, however, the influence of $\mathbf{H}_0$ still has to be considered during the time intervals without MW pulses. Such intervals are called intervals of free precession or free evolution of the spins. The magnetization vector $\mathbf{M}$ in this case is given by

$$\begin{aligned} M_x(t) &= M_0 \sin\beta \sin\left(\Omega t\right), \\ M_y(t) &= -M_0 \sin\beta \cos\left(\Omega t\right), \\ M_z(t) &= M_0 \cos\beta\,. \end{aligned} \tag{1.54}$$

M_z is called longitudinal magnetization and cannot be detected directly with usual experimental setups. M_x and M_y are the components of the transverse magnetization in the xy-plane and can be measured because they are coupled to the MW resonator [10].

1.4.3 Relaxation

From the above discussed formalism it follows that once the spin system has been excited the magnetization vector would remain precessing forever. This, however, does not agree with the real experimental observations where the excited system always goes back to the thermal equilibrium. Therefore, there must be a process which restores the equilibrium state. The mechanism of such relaxation processes cannot be discussed in a classical picture, since single-spin events are involved [10]. However it is possible to describe the relaxation phenomenologically using the formalism of magnetization vectors.

The static magnetic field $\mathbf{H}_0$ introduces an anisotropy of space and generates a unique axis along the z-direction. The longitudinal magnetization (M_z) relaxes towards its thermal equilibrium value M_0. Assuming an exponential relaxation (a first order process), the longitudinal relaxation T_1 term for the M_z-component is given by

$$\frac{\mathrm{d}M_z}{\mathrm{d}t} = \frac{-(M_z - M_0)}{T_1} \,.$$

The transverse magnetization in the xy-plane vanishes by relaxation and the time constant for this decay, in general, differs from T_1. Assuming an exponential decay with the transversal relaxation time T_2, the corresponding relaxation terms are given by

$$\frac{\mathrm{d}M_{x,y}}{\mathrm{d}t} = \frac{-M_{x,y}}{T_2} \,.$$

The extension of Eq. (1.46) by these terms yields the rotating-frame Bloch equations

$$\begin{aligned}
\frac{\mathrm{d}M_x}{\mathrm{d}t} &= -\Omega M_y - \frac{M_x}{T_2} \,, \\
\frac{\mathrm{d}M_y}{\mathrm{d}t} &= \Omega M_x - \omega_1 M_z - \frac{M_y}{T_2} \,, \\
\frac{\mathrm{d}M_z}{\mathrm{d}t} &= \omega_1 M_y - \frac{M_z - M_0}{T_1} \,.
\end{aligned} \tag{1.55}$$

Solutions of the Bloch equations are superposition of nutation shown in Fig. 1.6 c and of exponential relaxation of the magnetization vector components. In general, the magnitude of $\mathbf{M}$ is not a constant of motion, because $\mathbf{M}$ is not a single magnetic moment, but there are many independent spins contributing to it. For example, if these spins have slightly different fluctuating resonance offset Ω, the transverse magnetization fans out in the xy-plane and eventually averages (Fig. 1.7 b).

Solution of the Bloch equations for the case of one-pulse experiment introduced in the previous section yields the transverse magnetization components

$$\begin{aligned} M_x(t) &= M_0 \sin\beta \sin(\Omega t) \exp\left(-\frac{t}{T_2}\right), \\ M_y(t) &= -M_0 \sin\beta \cos(\Omega t) \exp\left(-\frac{t}{T_2}\right). \end{aligned} \tag{1.56}$$

The complex signal which is proportional to $M_y - iM_x$ is called a free induction decay (FID)

$$V(t) \propto \exp(i\Omega t) \exp\left(-\frac{t}{T_2}\right). \tag{1.57}$$

Note that the Bloch equations and the corresponding magnetization vector model are not applicable if more than two energy levels are involved in the experiment and they cannot be described as a superposition of independent two-level systems [10].

1.4.4 Electron Spin Echoes

The phenomenon of the spin echo is based on the non-linear behavior of an ensemble of spins with different Larmor frequencies [13]. In the thermal equilibrium, the magnetization vector is oriented along the z-axis. The $\pi/2$ MW pulse ($\beta = \pi/2$) along the x-axis turns the magnetization to the $-y$-direction. After the pulse, different spin packets begin to precess about the z-axis with their individual Larmor frequencies. This results in the defocusing of the transverse magnetization (Fig. 1.8). Time τ after the first pulse, the π pulse along the x-axis rotates all the magnetization vectors by 180° about the x-axis. Since the direction of rotation of the magnetization vectors did not change, after the next time τ the refocusing of the transverse magnetization takes place. The resulting net magnetization is called electron spin echo or primary echo. In general, the amplitude of such a

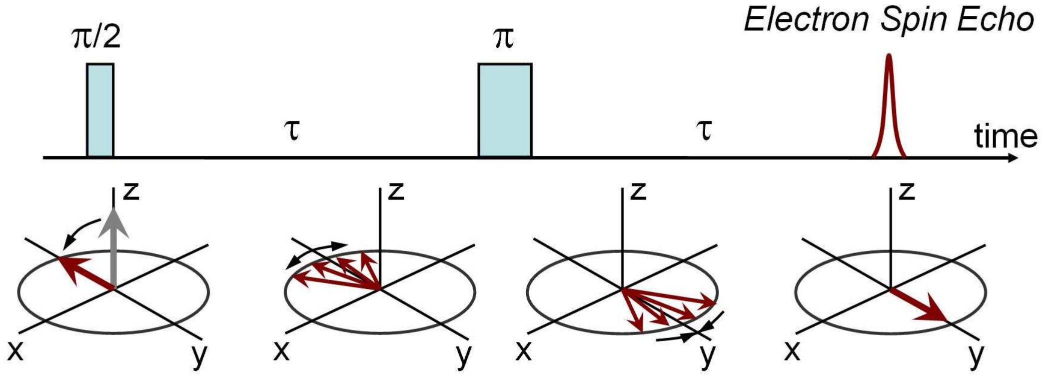

Figure 1.8: Pulse sequence and the motion of the magnetization vector in the primary echo experiment.

spin echo is a function of the pulse spacing τ and, its decay is described by the so-called phase memory time T_{m} or T_2^*. Therefore, the two-pulse sequence is the most simple and straightforward way to determine T_{m} in a two-level system [10].

The stimulated echo is a more complex echo effect which can be observed in an electron spin two-level system. In a stimulated echo experiment with the sequence $\pi/2 - \tau - \pi/2 - t - \pi/2 - \tau - echo$, the time t between the second and third pulse can be of the order of T_1, that enables the determination of this parameter, whereas in the primary echo experiments with variable τ the observation of the echo is limited by the phase memory time T_{m}. The first $\pi/2$ rotates the magnetization vector about the x-axis by 90° where the defocusing takes place. After the time τ, the second $\pi/2$ pulse rotates the magnetization vectors of each spin packet about the x-axis by another 90°. This moves some of the magnetization vectors completely back in line with the z-axis. Some of the magnetization vectors are partially moved towards the z-axis; and the rest stays along the x-axis. The components that remain in the xy-plane will be lost since they dephase completely during the time t, while the components directed along the z-axis decay with a much longer T_1 relaxation time towards the thermal equilibrium. The third $\pi/2$ pulse transfers the z-components of the magnetization again into the xy-plane where they refocus, and, after time τ, the stimulated echo is formed.

In general, there are many different echo experiments with various pulse sequences which are used in the pulse ESR spectroscopy, such as four-pulse and multiple pulse echos, edge echoes, rotary echoes and driven echoes. All these experiments provide different information about the electron spin dynamics [10].

2 Measurement Techniques

2.1 High-Field/Frequency Electron Spin Resonance

High-field electron spin resonance (HF-ESR) in static magnetic fields was studied with a Millimeterwave Vector Network Analyzer (MVNA) from AB Millimetré used for generation of millimeter- and submillimeter microwaves and phase-sensitive detection of a signal. The MVNA is a tunable high frequency device designed for operation between 16 and 800 GHz. The generation and

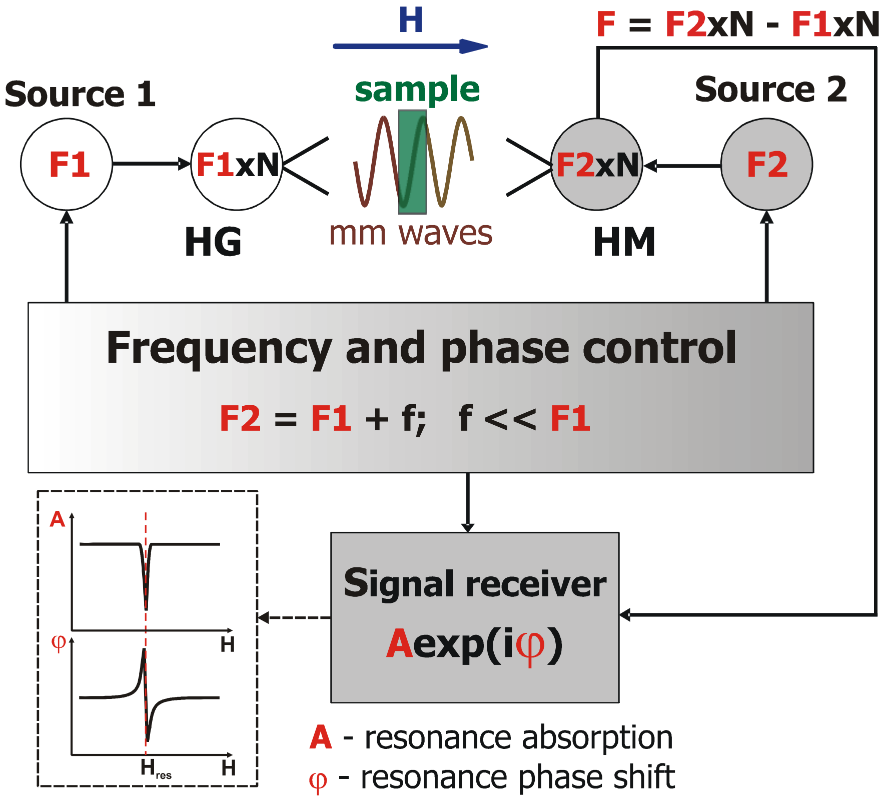

Figure 2.1: The principle scheme of the MVNA based high-field ESR spectrometer with the phase-locked source and detection system.

detection of the radiation is realized electronically by application of non-linear solid state devices. The phase-sensitive detection of the mm/sub-mm waves is achieved by means of a phase-locked source and detection system [14]. The principle scheme of the MVNA based spectrometer is shown in Fig. 2.1. Here, 'Source 1' provides a frequency $F1$ which is further multiplied using a Schottky diode multiplier (harmonic generator **HG**) and transferred to the sample. After passing through the sample the resulting frequency ($F1 \times N$) is mixed with the second frequency from the 'Source 2' ($F2 \times N$) by means of a second Schottky diode (harmonic mixer **HM**). This operation allows to produce an intermediate frequency signal ($F = F2 \times N - F1 \times N = f \times N$) suitable for the detection and analysis. The MVNA was used in combination with a superconducting magneto-cryostat (Oxford Instruments) allowing the ESR measurements in magnetic fields up to 15 T at temperatures between 4 and 300 K.

2.2 X-Band Continuous Wave and Pulse ESR Spectroscopy

X-band (9.56 GHz) continuous wave ESR measurements were performed by means of a commercial X-band Bruker EMX spectrometer with a Bruker rectangular resonator 4104OR-C/0801. In order to substantially increase the signal-to-noise ratio a method of magnetic field modulation is used in this setup. This method, as shown in Fig. 2.2, leads to the detection of the ESR spectra in the form of the

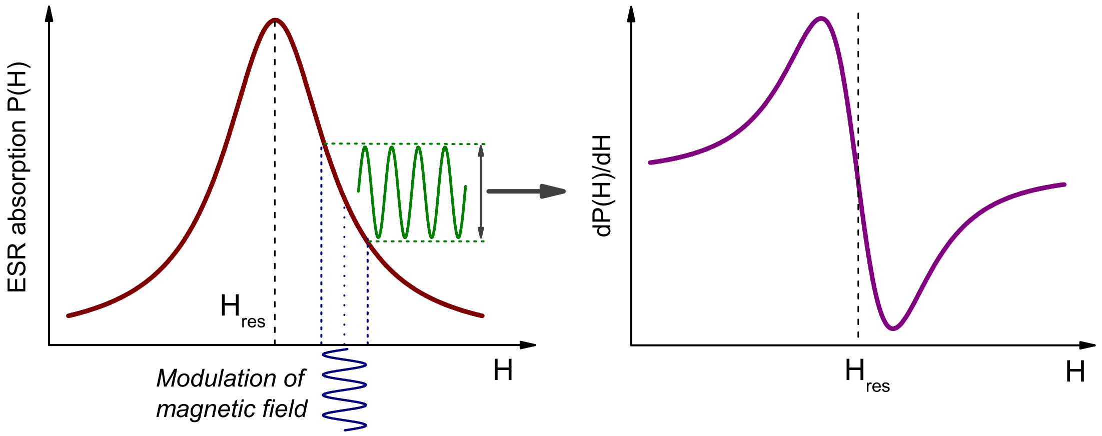

Figure 2.2: The principle of the magnetic field modulation and the ESR spectra detection in a Bruker EMX X-band spectrometer.

first derivative of the absorbed microwave power $dP(H)/dH$. The temperature control was carried out using a helium gas-flow cryostat and a temperature controller ITC503 (Oxford Instruments) which allow measurements at temperatures between 3.4 and 300 K.

Pulse ESR experiments were done in a collaboration with the Zavoisky Physical-Technical Institute, Kazan, Russia. The measurements were performed at X-band frequencies with a Bruker Elexsys E-580 spectrometer equipped with a Bruker cylindrical dielectric resonator ER4118-MD5-W1. Phase coherence times T_2 were measured by applying primary echo sequence $\pi/2$ - τ - π - τ - *echo* (ref. to section 1.4.4) with 8 ns long $\pi/2$ pulse. To measure longitudinal relaxation times T_1 stimulated echo sequence $\pi/2 - \tau - \pi/2 - t - \pi/2 - \tau - echo$ (ref. to section 1.4.4) with the fixed τ value of 120 ns and variable time t (length of $\pi/2$ pulse is equal to 8 ns) was performed. The obtained electron spin echo signal was recorded using PulseSPEL (Pulse SPEctroscopy Language) pulse program for different τ (T_2 measurements) and t (T_1 measurements). To remove unwanted effects such as the imbalance in the acquisition channels of the spectrometer, dc-offset and others, 4-step phase cycling (CYCLOPS) was used. After acquiring experimental data points the absolute values of the echo signal were obtained and the integrated echo intensity was calculated. The sample temperature was controlled using a helium gas-flow cryostat and a temperature controller ITC503 (Oxford Instruments).

2.3 Magnetization Measurements

Static magnetization measurements in magnetic fields up to 5 T were performed by means of a superconducting quantum interference device (SQUID) magnetometer MPMS-XL5 (magnetic properties measurement system) from Quantum Design. The measurements in magnetic fields up to 7 T were done using a Quantum Design MPMS SQUID-VSM (vibrating sample magnetometer). Both devices enable temperature dependent magnetization measurements in the temperature range between 1.8 and 400 K.

Magnetization measurements in magnetic fields up to 15 T were carried out by means of a home made VSM (Foner Magnetometer [15]) [16]. High-field magnetization measurements in pulsed magnetic fields were performed in the Dresden High Magnetic Field Laboratory (HLD) at the Rossendorf Research Center [17].

The setup provides a magnetic field up to 60 T within 5 ms with total pulse duration of 30 ms using the inductive technique. Since the two above described setups do not allow to determine precisely the absolute values of the magnetization, the resulting data were calibrated with the values obtained with the MPMS.

2.4 Modelling and Simulations

The analysis and simulation of the ESR spectra were done by means of the EasySpin toolbox for Matlab [18]. The analysis and simulation of the temperature dependence of the magnetic susceptibility $\chi(T)$ were done by means of the ***julX*** simulation program [19].

3 Single Molecule Magnetic Complexes

A fascinating approach to obtain nanoscale magnets is the synthesis of metal-organic molecular complexes containing a finite number of paramagnetic ions. The ionic moments are strongly magnetically coupled via organic bridge ligands and therefore form a magnetic cluster with a well-isolated ground state. The main objective for the synthesis of such clusters is a system which can be described by a single large spin with a well-pronounced uniaxial magnetic anisotropy. In this regard, molecules with large effective spins have been successfully realized [11], such as the ferromagnetically-coupled Mn_{19} cluster with a spin $S = 83/2$ in the ground state [20].

The most prominent representative of those species is the Mn_{12}Ac compound,

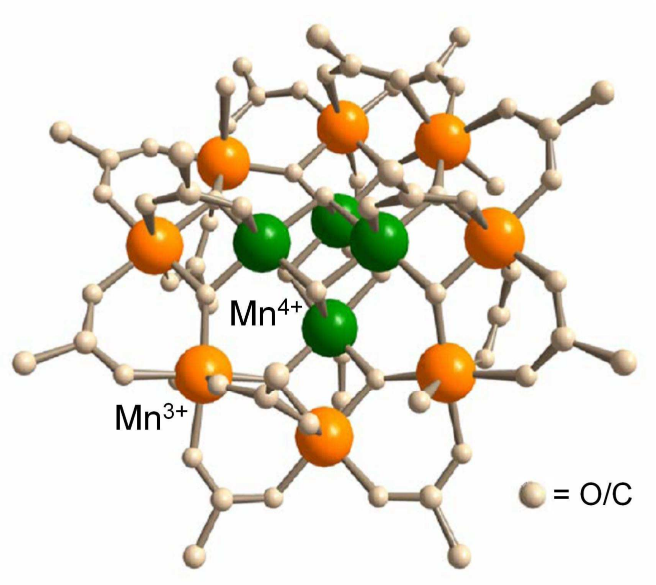

Figure 3.1: Structure of the Mn_{12}Ac-core [21]. The four inner ions are Mn^{4+}. The eight ions in the outer ring are Mn^{3+}. (See text for details)

whose chemical formula is $\mathrm{Mn_{12}O_{12}(CH_3COO)_{16}(H_2O)_4}$. $\mathrm{Mn_{12}Ac}$ was first synthesized by Lis [22] in 1980. In this cluster, the four inner Mn^{4+} ($3d^3$, $S_{\mathrm{Mn}} = 3/2$) ions (see Fig. 3.1) are ferromagnetically coupled and form a unit with spin 6. This unit is antiferromagnetically coupled to the outer ring of Mn^{3+} ($3d^4$, $S_{\mathrm{Mn}} = 2$) ions, yielding a total spin $S = 10$ for the ground state of the molecule. There is a pronounced negative axial magnetic anisotropy ($D = -0.72\,\mathrm{K}$) which removes the $(2S+1)$-fold degeneracy of the ground state multiplet. The $S = 10$ ground state splits into $2S+1 = 21$ levels, $m_S = \pm 10, \pm 9, ..., \pm 1, 0$ (see Fig. 3.2 a). Since the states with $m_S = \pm 10$ have the same energy, this ground state is bistable which is characteristic for single-molecule magnets (SMM). Consequently, the two lowest states are separated by the energy barrier

$$\Delta E = |D|(S_{z,\max}^2 - S_{z,\min}^2)\,. \tag{3.1}$$

For temperatures $T \sim \Delta E/k_{\mathrm{B}}$ the relaxation time of the magnetization depends on the height of the barrier according to the Arrhenius equation,

$$\tau = \tau_0 \exp(\Delta E/k_{\mathrm{B}}T)\,, \tag{3.2}$$

where τ_0 is the pre-exponential factor. Therefore, the relaxation slows down when the ratio $\Delta E/k_{\mathrm{B}}T$ is increased. This leads to a hysteresis in the magnetic field dependence of the magnetization a below certain temperature regime. Since this hysteretic behavior is of purely molecular origin, such complexes are called single-molecular magnets.

Thermal activation is not the only mechanism which causes the relaxation of the magnetization. In 1996 unusual steps were found in the hysteresis loop of $\mathrm{Mn_{12}Ac}$ [23, 24]. The mechanism of this additional relaxation pathway is denoted

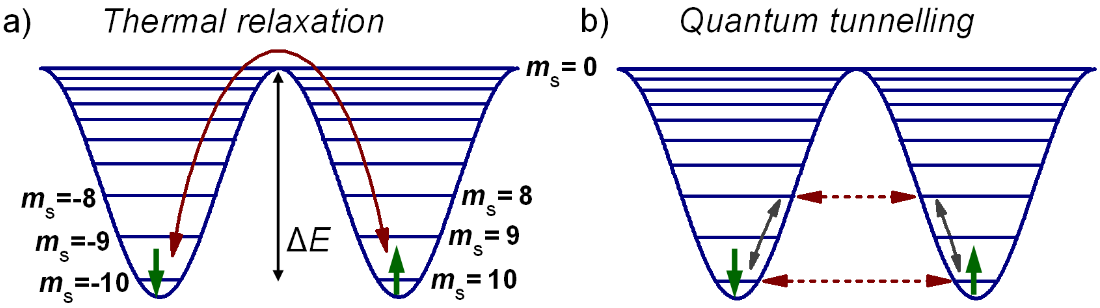

Figure 3.2: Energy barrier and splitting of the energy levels due to the single ion anisotropy. a) Thermal relaxation of the magnetization. b) Quantum tunnelling of the magnetization.

as quantum tunnelling of the magnetization (QTM) through the energy barrier (Fig. 3.2 b). This effect is related to the symmetry of the system: transverse (in-plane) and higher order anisotropy may yield an admixture of the iso-energetic quantum states on different sides of the barrier and therefore a finite probability of transition between them.

In the following sections a detailed study of several new molecular magnetic complexes will be described. The complexes were studied by means of static magnetization measurements and electron spin resonance (ESR) spectroscopy. The measurements enabled the determination of all relevant parameters of the magnetic complexes, such as total spin value, magnitude and sign of the magnetic anisotropy, value of the exchange coupling between the magnetic ions. Some of the complexes were also studied by means of pulse ESR, which allows one to estimate the spin relaxation times and to identify the relaxation mechanisms.

3.1 Ni(II) Dimer and Trimer Complexes

Over the past decades much interest has arisen in the synthesis and characterization of polynuclear transition-metal thiolate complexes [25–28]. The interest in these compounds is mainly due to their biological relevance as simple model compounds for the active sites of metalloenzymes [29–31], and their intriguing magnetic and electronic properties [32–34]. Macrocyclic ligands are often employed as supporting ligands as their complexes are more stable than those of their acyclic counterparts. In addition, the metal ions are fixed in close proximity and can be arranged in almost any topology which has important implications for the metal-metal interactions [35, 36].

An attractive feature of the hexaaza-dithiophenolate ligand (H_2L^1 [37]) and its various derivatives is the possibility to derive a magneto-structural correlation between the sign of the exchange parameter J and the Metal-S-Metal bond angle [37]. For di-nickel(II) complexes, for example, the spins of the Ni(II) ions couple ferromagnetically if the average Ni-S-Ni angles are of $\sim 90 \pm 5^\circ$ [38–41]. Smaller or larger angles give rise to antiferromagnetic exchange interactions between the metal centers. Thus with increasing deviation from the 90° bonding geometry the antiferromagnetic contribution to the total exchange will grow and eventually produce a change in the sign of J. Although such interplay is rather well understood since pioneering works of Goodenough, Kanamori and Anderson (GKA-rules, see, e.g. [42]), the actual dependence of J on the bond angle can often be significantly affected by specific details of the local coordination and particular bonding features [43, 44].

In this context, studying the magnetic behavior of newly-synthesized materials is important to understand the relationship between a specific bonding topology and the magnetic interactions between metal ions. Specifically, magneto-structural correlations are of importance for the targeted assembly of molecular-based magnetic materials [45–47]. Therefore, it was of interest to synthesize novel nickel(II) amino-thiophenolate complexes with different Ni-S-Ni angles and to characterize their magnetic properties. In this section, a detailed magnetic study of two novel binuclear and trinuclear Ni(II) complexes by means of static magnetization measurements and high-field electron spin resonance spectroscopy is presented.

3.1.1 Molecular Structures

Two Ni(II)-based dinuclear and trinuclear molecular complexes have been recently synthesized in Leipzig by the group of Prof. Kersting. The synthesis details and the full structural and spectroscopic characterization of these complexes were published in Ref. [48]. It was shown that the Ni_2-complex is formed as the paramagnetic I_2 adduct $[\mathrm{Ni}^{\mathrm{II}}_2\mathrm{L}^1(\mathrm{OAc})\cdot\mathrm{I}_2][\mathrm{I}_5]$ from the reaction of $[\mathrm{Ni}^{\mathrm{II}}_2\mathrm{L}^1(\mathrm{OAc})][\mathrm{ClO}_4]$ with five equivalents of diiodine. The crystal structure analysis confirmed the presence of the dinuclear diiodine adduct and a V-shaped pentaiodide counteranion. The molecular structure of the Ni_2-complex is presented in Fig. 3.3 a. Here, the two Ni(II) ions have similar distorted octahedral $\mathrm{N}_3\mathrm{S}_2\mathrm{O}$ coordination environments with average Ni-N, Ni-S, and Ni-O distances of 2.209(5) Å, 2.515(2) Å, and 1.987(4) Å, respectively. The Ni-Ni distance is 3.601(1) Å, and Ni-S(1)-Ni and Ni-S(2)-Ni angles are 88.4° and 94.7°, respectively. Such a topology of the Ni_2-core suggests two almost equivalent magnetic exchange paths between the two Ni^{2+} ($3d^8$, $S_{\mathrm{Ni}} = 1$) spins which can be effectively described by a single exchange

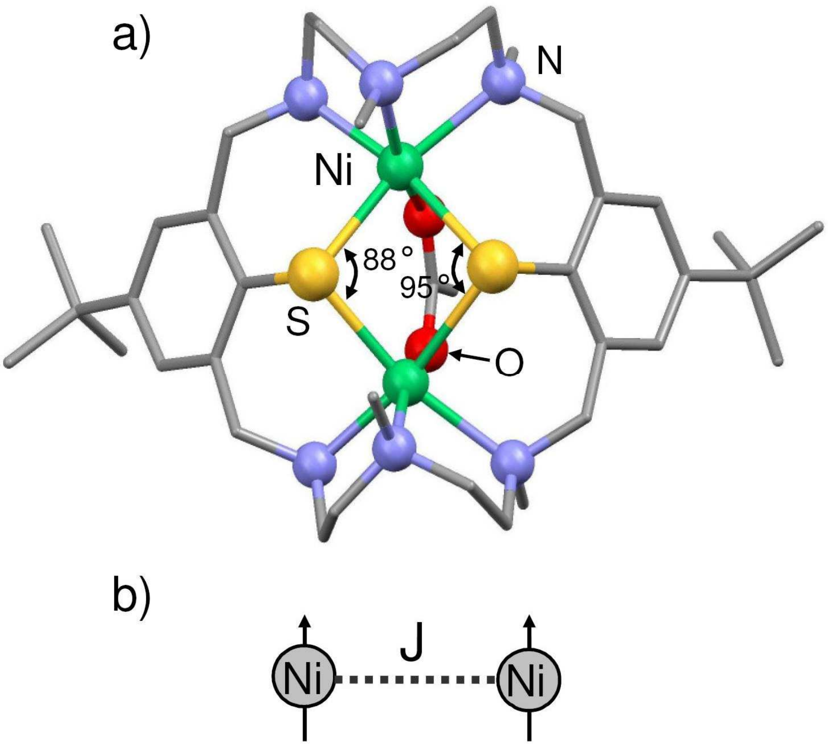

Figure 3.3: a) Molecular structure of the Ni_2-complex (the I_2 is omitted for reasons of clarity). b) Scheme of the expected magnetic coupling of the two Ni^{2+} ions in the Ni_2-core.

coupling parameter J (cf. Fig. 3.3 b, to be discussed later).

The Ni_3-complex formed rather unexpectedly during attempts to prepare a dinuclear complex. The crystal structure contains trinuclear $[Ni_3L(OAc)_2]^{2+}$ dications, BPh_4^- anions and MeCN and MeOH solvate molecules. The molecular structure of the $[Ni_3L(OAc)_2]^{2+}$ dication is presented in Fig. 3.4 a. The macrocycle supports a trinuclear complex, with distorted octahedral $N_2S_2O_2$ and N_2SO_3 coordination environments for the central and the terminal Ni(II) ions, respectively. The bond lengths and angles around the central and terminal Ni atoms differ slightly, as one might expect. The average Ni-N, Ni-S, and Ni-O distances are 2.098(3) Å, 2.316(1) Å and 2.091(2) Å for the terminal Ni ions and 2.233(3) Å,

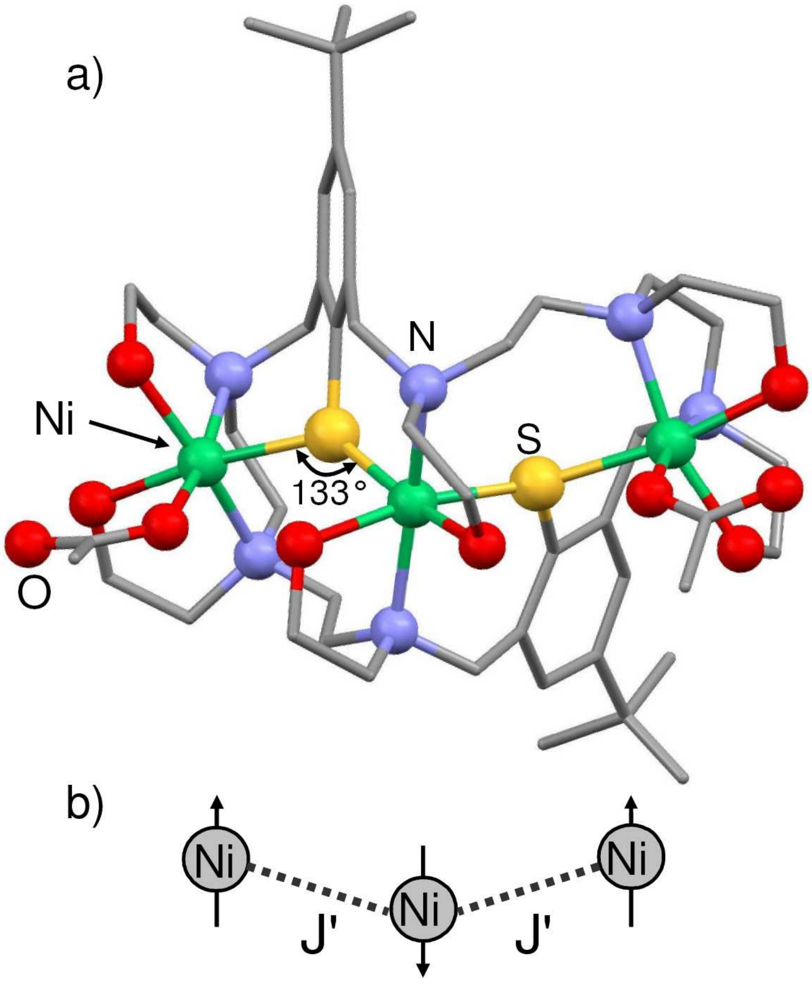

Figure 3.4: a) Molecular structure of the Ni_3-complex (BPh_4^- anions and MeCN and MeOH solvate molecules are omitted for clarity). b) Scheme of the expected magnetic coupling of the tree Ni^{2+} ions in the Ni_3-core.

2.296(1) Å and 2.132(2) Å for the central one, respectively. The Ni-S-Ni angles are 132.8° and 133.5°. The Ni-Ni distances are 4.229 Å and 4.234 Å. The topology of the Ni_3-core suggests a single magnetic exchange coupling J' between the three Ni^{2+} ($3d^8$, $S_{Ni} = 1$) ions via the sulphur bridges (cf. Fig. 3.4 b). This appreciably simplifies the experimental data analysis and the interpretation of the magnetic properties of the Ni3-complex (cf. section 3.1.3).

3.1.2 Magnetic Properties of the Dinuclear Ni(II) Complex

Static Magnetization Measurements

The static magnetization M of the Ni_2-complex was measured by A. Parameswaran on microcrystalline powder samples in the temperature range $T = 2{-}300\,\mathrm{K}$ and in magnetic fields $\mu_0 H$ up to 5 T with the SQUID magnetometer MPMS-XL5. The field dependence of the magnetization $M(H)$ at low temperatures (2 K and 4.2 K) is shown in Fig. 3.5. The measurements reveal a saturation magnetization M_S of about 4.6 μ_B/2Ni which corresponds to the magnetic ground state of the molecule with a total spin $S_{tot} = 2$. This observation implies ferromagnetic (FM) coupling between the two Ni^{2+} ions ($3d^8$, $S_{Ni} = 1$). This conclusion is confirmed

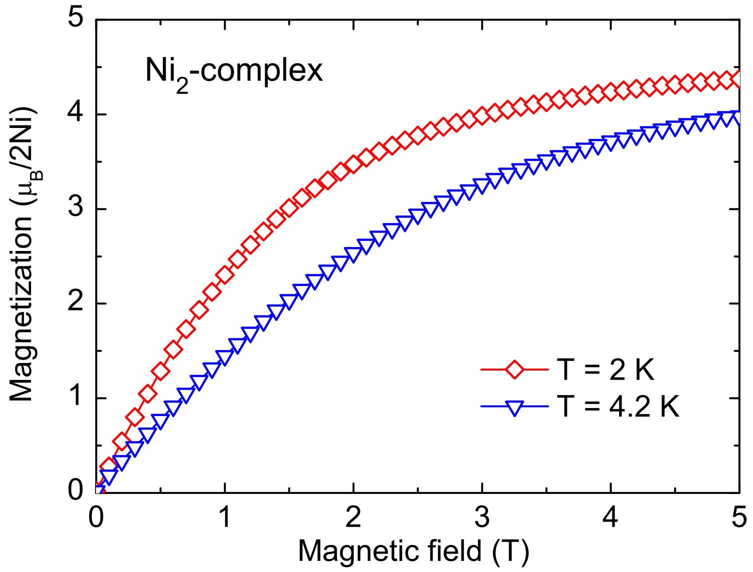

Figure 3.5: Field dependence of the magnetization $M(H)$ of the Ni_2-complex at $T = 2\,\mathrm{K}$ and $T = 4.2\,\mathrm{K}$.

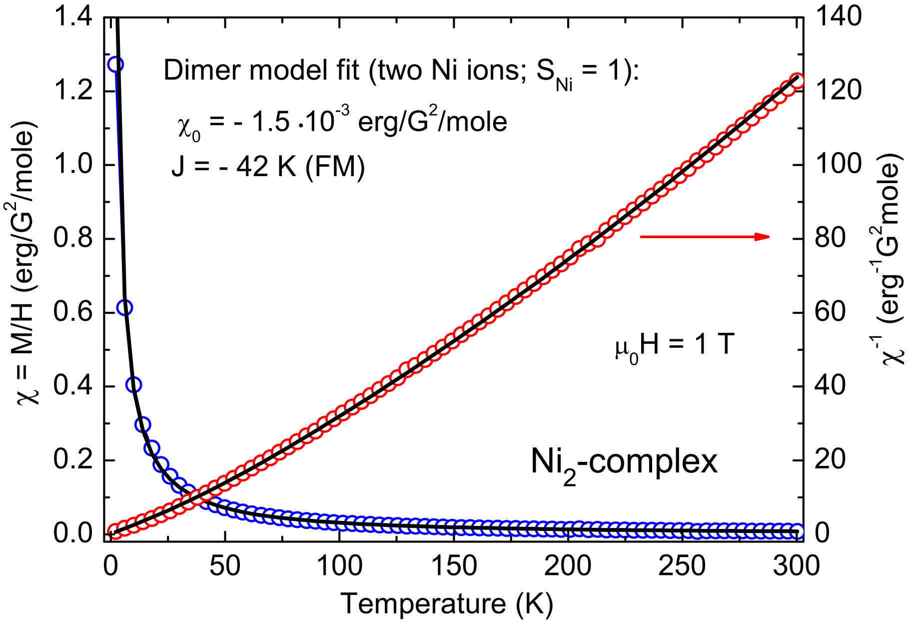

Figure 3.6: Temperature dependencies of the static susceptibility $\chi(T) = M(T)/H$ and the inverse susceptibility $\chi^{-1}(T)$ of the Ni$_2$-complex in a magnetic field of 1 T (circles). The black lines represent a numerical model fit using the Hamiltonian (3.4). A temperature-independent contribution χ_0 is included into the fit.

by the temperature dependence of the static susceptibility $\chi(T) = M(T)/H$ and the inverse susceptibility $\chi^{-1}(T)$ presented in Fig. 3.6. As will be shown below, these data can be well described by means of the FM dimer model.

High-Field ESR Measurements

High-field ESR (HF-ESR) of the Ni$_2$-complex in static magnetic fields was measured with the Millimeterwave Vector Network Analyzer MVNA (see chapter 2). The measurements were performed on a loose powder sample in magnetic fields $\mu_0 H$ up to 15 T at frequencies $\nu = 80 - 350$ GHz. The small powder particles self-oriented in the magnetic field during the measurements due to the presence of the "easy axis" magnetic anisotropy (see below). A typical ESR spectrum at $T = 30$ K exhibits four separate ESR lines. The respective frequency ν vs. resonance field H_{res} dependencies (resonance branches) of all observed lines together with representative ESR spectra are shown in Fig. 3.7. The slopes of the resonance branches reveal a g-factor of 2.3 for all four ESR lines. The extrapolation

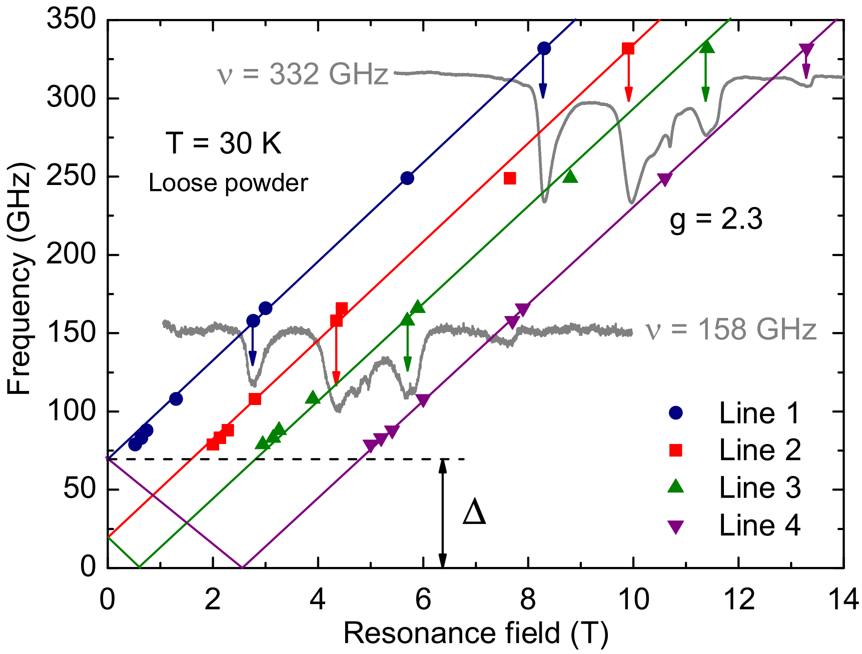

Figure 3.7: Frequency vs. resonance field $\nu(H_{\mathrm{res}})$-dependencies of the ESR resonance modes (resonance branches) for the Ni_2-complex at $T = 30\,\mathrm{K}$.

of the $\nu(H_{\mathrm{res}})$-dependence of line 1 to $H_{\mathrm{res}} = 0$ implies a magnetic anisotropy gap $\Delta \approx 70\,\mathrm{GHz}$ (3.4 K). The T-dependence of the ESR spectrum of the Ni_2-complex is presented in Fig. 3.8. Here, one can see a transfer of the spectral weight to lower magnetic fields at low temperatures, which indicates a negative axial magnetic anisotropy of the molecule ($D_{\mathrm{S}} < 0$).

Analysis

The observation of four separate ESR lines at all measurement temperatures (up to 60 K) and the fact that no additional ESR lines appeared a high T give evidence that the observed ESR spectra correspond to the ground state of the molecule. Therefore, for the analysis of the ESR spectra a minimal model describing only the ground state has been introduced. Here, we assume that each molecule has a single total spin $S = S_{\mathrm{tot}} = 2$, and possesses a g-factor of 2.3 and a magnetic anisotropy gap $\Delta = |D_S|(S^2 - (S-1)^2) = 70\,\mathrm{GHz}$. In this case a minimal effective spin Hamiltonian can be introduced in the form

$$\mathcal{H} = D_S(S_z^2 - S(S+1)/3) + E_S(S_x^2 - S_y^2) + g\mu_{\mathrm{B}}\,\mathbf{H}\cdot\mathbf{S}\,. \tag{3.3}$$

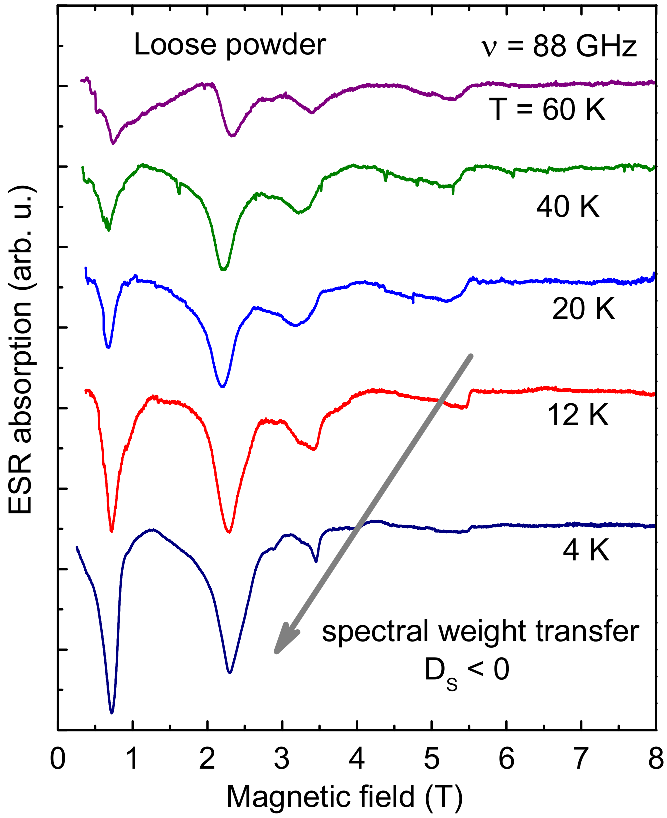

Figure 3.8: T-dependence of the ESR spectrum of the Ni$_2$-complex at $\nu = 88\,\text{GHz}$. Note, the relative intensity of the ESR lines changes with the temperature so that the low field lines become dominant.

Here, the first two terms describe the zero-field splitting of the spin states caused by an anisotropic ligand crystal field potential comprising axial and rhombic terms, respectively. D_S is the axial magnetic anisotropy parameter and E_S is the transverse magnetic anisotropy parameter of the complex. Generally, D_S and E_S are determined by the single ion anisotropies of the individual metal ions due to the ligand crystal fields, with possible contributions arising from the anisotropic part of the Ni-Ni magnetic exchange interaction. The last term is the Zeeman interaction of the total spin with the external magnetic field H. The solution of the Hamiltonian (3.3) yields the eigenvalues $E_i(D_S,E_S,H,g)$ and eigenfunctions $\psi_i(D_S,E_S,H,g)$ of the energy levels. After plugging in the estimates of D_S, E_S and g obtained from the raw experimental data, the knowledge of E_i and ψ_i allows to simulate the ESR spectra. The adjustment of the simulated spectra to the measured ones by fine tuning of D_S, E_S and g enables accurate refinement and verification of these parameters.

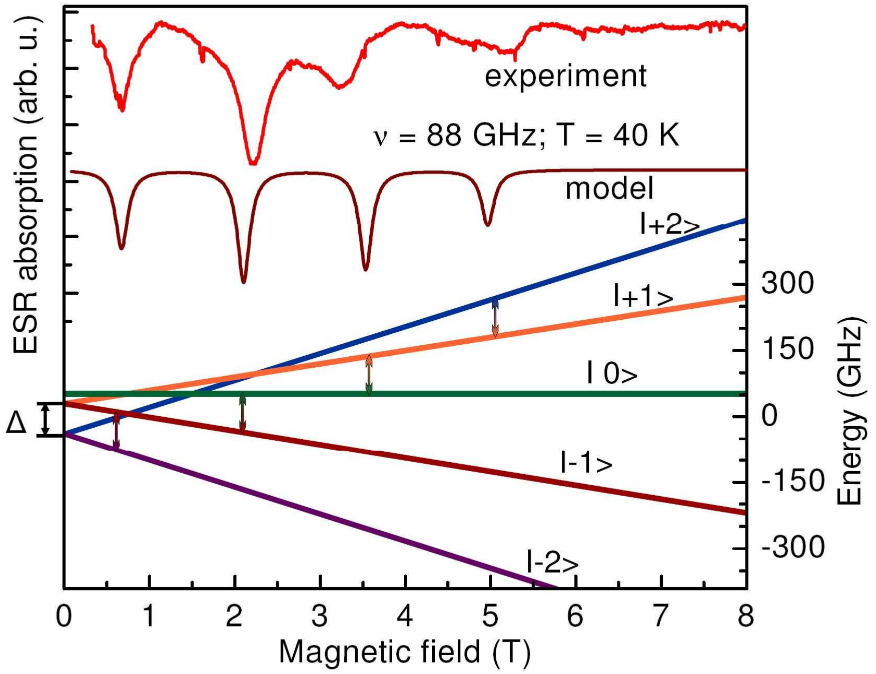

Figure 3.9: Measured and simulated ESR spectra at $\nu = 88\,\mathrm{GHz}$ and $T = 40\,\mathrm{K}$ and the calculated energy level scheme of the spin states of the Ni_2-complex.

The simulations of the ESR spectra were performed for the parallel orientation of the magnetic anisotropy axis to the applied magnetic field. A simulated spectrum at $\nu = 88\,\mathrm{GHz}$, $T = 40\,\mathrm{K}$ together with a representative experimental spectrum of the Ni_2-complex and calculated energy levels is presented in Fig. 3.9. The simulation shows that the observed number of the ESR lines (four) is defined by the total spin of the Ni_2-complex $S_{\mathrm{tot}} = 2$ and the zero field splitting of the energy levels. Note, that magnetic anisotropy of the Ni_2-complex can be well described only by an axial magnetic anisotropy parameter D_S (i.e. $E_S = 0$). The model confirms the experimentally-determined value of $\Delta = 3|D_S| = 70\,\mathrm{GHz}$ (3.4 K) and the negative sign of the axial magnetic anisotropy $D_S = -23.3\,\mathrm{GHz}$ ($-1.1\,\mathrm{K}$). Note, that the negative sign of D_S implies an “easy” magnetic anisotropy axis for the Ni_2-complex and, therefore, a bistable magnetic ground state.

In order to analyze the magnetic behavior of the Ni_2-complex at higher temperatures (up to 300 K), where the contribution from the excited spin states cannot be omitted, an additional term describing the intramolecular magnetic exchange interaction between individual spins of Ni ions is included in the effective spin

Hamiltonian (3.3),

$$\mathcal{H}' = D_{\rm eff}\sum_{i=1}^{N}(S_{iz}^2 - S_i(S_i+1)/3) + E_{\rm eff}\sum_{i=1}^{N}(S_{ix}^2 - S_{iy}^2) + g\mu_{\rm B}\sum_{i=1}^{N}\mathbf{H}\cdot\mathbf{S}_i + J\sum_{i>j}\mathbf{S}_i\cdot\mathbf{S}_j\,, \qquad (3.4)$$

where N is the number of ions in the complex. The first two terms of the Hamiltonian describe the zero-field splitting of the spin states of each Ni ion, the third term is the Zeeman interaction of the Ni spins with the external magnetic field H and the last term describes the isotropic intramolecular magnetic coupling between the neighboring Ni ions ($J < 0$ denotes ferromagnetic (FM) coupling). The topology of the $\mathrm{Ni_2}$-core suggests two equivalent exchange paths between the two $\mathrm{Ni^{2+}}$ ions effectively described by a single exchange coupling parameter J (cf. Fig. 3.3). The parameters of the magnetic anisotropy were assumed to be equal for the two Ni ions. Therefore $D_{\rm eff}$ stands here for an effective magnetic anisotropy parameter of each Ni ion. It was determined from the analysis of the ESR spectra of the ground state of the complex ($S_{\rm tot} = 2$) as $D_{\rm eff} = D_S(S_{\rm tot}^2 - (S_{\rm tot}-1)^2) = -\Delta$. Solving numerically the Hamiltonian allows for a simulation of the temperature dependence of the magnetic susceptibility $\chi(T)$. The simulated $\chi(T)$ and $\chi^{-1}(T)$ curves are presented together with the experimental data in Fig. 3.6. One can see that the model curves fully reproduce the experimental results. Specifically, the modelling reveals a ferromagnetic coupling $J = -42\,\mathrm{K}$ between the two Ni ions and a temperature independent diamagnetic component $\chi_0 = -1.5\cdot 10^{-3}\,\mathrm{erg/G^2/mole}$ caused by the diamagnetic susceptibility of the organic ligands.

3.1.3 Magnetic Properties of Trinuclear Ni(II) Complex

Static Magnetization Measurements

The static magnetization M of the $\mathrm{Ni_3}$-complex was measured by A. Parameswaran on a microcrystalline powder sample in the temperature range $T = 2 - 300\,\mathrm{K}$ and in magnetic fields H up to 5 T with the SQUID magnetometer MPMS-XL5. The field dependence of the magnetization $M(H)$ at low temperatures (2 K and 4.2 K) is presented in Fig. 3.10. These measurements reveals a magnetic moment of $1.94\,\mu_{\rm B}/3\mathrm{Ni}$ at $\mu_0 H = 5\,\mathrm{T}$. Although the magnetization is not saturated

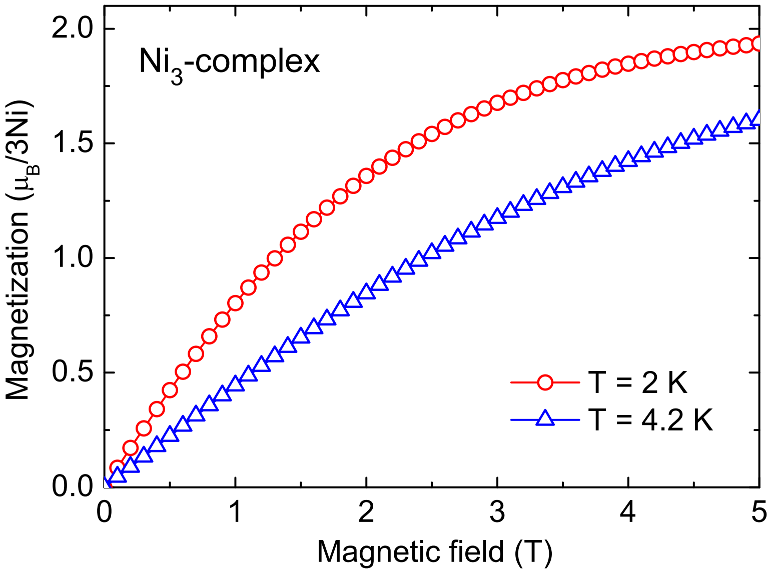

Figure 3.10: Field dependence of the magnetization $M(H)$ of the Ni$_3$-complex at $T = 2\,\mathrm{K}$ and $T = 4.2\,\mathrm{K}$.

at $\mu_0 H = 5\,\mathrm{T}$, the shape of the curve implies an approach to the saturation of the magnetic moment corresponding to the magnetic ground state of the molecule with a total spin $S^{\mathrm{tot}} = 1$ ($\mu_{\mathrm{S}} = 2.2\,\mu_{\mathrm{B}}/3\mathrm{Ni}$). In contrast to the Ni$_2$-complex, $S^{\mathrm{tot}} = 1$ here implies an antiferromagnetic (AFM) coupling between the three Ni^{2+} spins ($3d^8$, $S_{\mathrm{Ni}} = 1$). The temperature dependence of the static magnetic susceptibility $\chi(T) = M(T)/H$ and the inverse susceptibility $\chi^{-1}(T)$ of the Ni$_3$-complex are shown in Fig. 3.11. Here, we observe a strong non-linearity of $\chi^{-1}(T)$ which, as will be discussed below, corresponds to the thermal activation of higher energy spin multiplets ($S_1^{\mathrm{tot}} = 2$, $S_2^{\mathrm{tot}} = 3$).

High-field ESR Measurements

HF-ESR measurements were performed on a powder sample for $\mu_0 H = 0 - 15\,\mathrm{T}$ and $\nu = 80 - 350\,\mathrm{GHz}$ by means of the MVNA (see chapter 2). A typical ESR spectrum of the Ni$_3$-complex at a low temperature ($T = 4\,\mathrm{K}$) consists of a sharp stand-alone line at a resonant field H_{res} of around 2.5 T (line 1) and a group of lines distributed in the magnetic field range from 3.5 to 7.5 T (lines 2 - 7). The resonance branches of these lines together with representative ESR spectra are shown in Fig. 3.12. The slopes of the resonance branches $2 - 7$ correspond to a g-factor of 2.2. Branch 1 has an almost twice steeper slope which can be

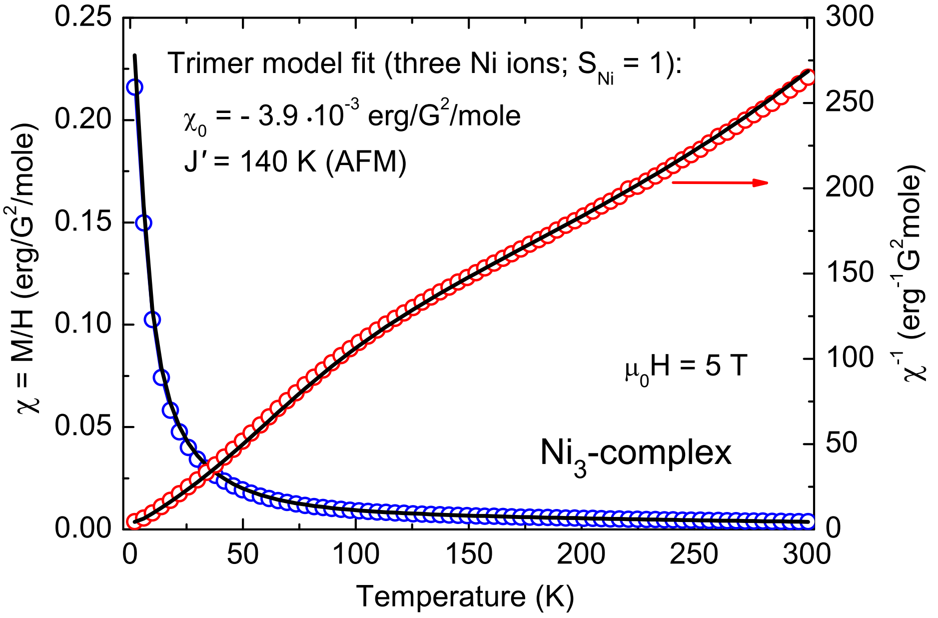

Figure 3.11: Temperature dependencies of the static susceptibility $\chi(T)$ and the inverse susceptibility $\chi^{-1}(T)$ of the Ni$_3$-complex in $\mu_0 H = 5\,\mathrm{T}$ (open circles). The black lines represent a numerical model fit using the Hamiltonian (3.4). A temperature independent contribution χ_0 is included into the fit.

described by a phenomenological "effective" g-factor of 4.0. Linear extrapolation of $\nu(H_{\mathrm{res}})$ of line 2 to $H_{\mathrm{res}} = 0$ reveals a magnetic anisotropy gap $\Delta \approx 60\,\mathrm{GHz}$ (2.9 K) which, in the case of $S_{\mathrm{tot}} = 1$, is equal to the axial magnetic anisotropy of the molecule, $\Delta = |D_S|(S_{\mathrm{tot}}^2 - (S_{\mathrm{tot}} - 1)^2) = |D_S|$.

The observed number of the seven ESR lines is not expected for an $S = 1$ system with parallel orientation of the anisotropy axes, however it can be the case for a powder spectrum where all possible orientation are present. This observation indicates that the loose powder did not self-orient in the applied magnetic fields which gives the first indication of the "easy plane" situation for this complex.

The T-dependence of the ESR spectrum is presented in Fig. 3.13. The intensity of the ESR lines substantially decreases with increasing temperature, whereas the shape of the ESR spectrum does not significantly change. In particular, no additional ESR lines appear in the spectrum at higher temperatures. These facts give evidence that all detected ESR lines correspond to the ground state of the molecule $S_0^{\mathrm{tot}} = 1$. In contrast, the activation of higher-energy spin multiplets ($S_1^{\mathrm{tot}} = 2$, $S_2^{\mathrm{tot}} = 3$) is not detected by the ESR measurements, which suggests

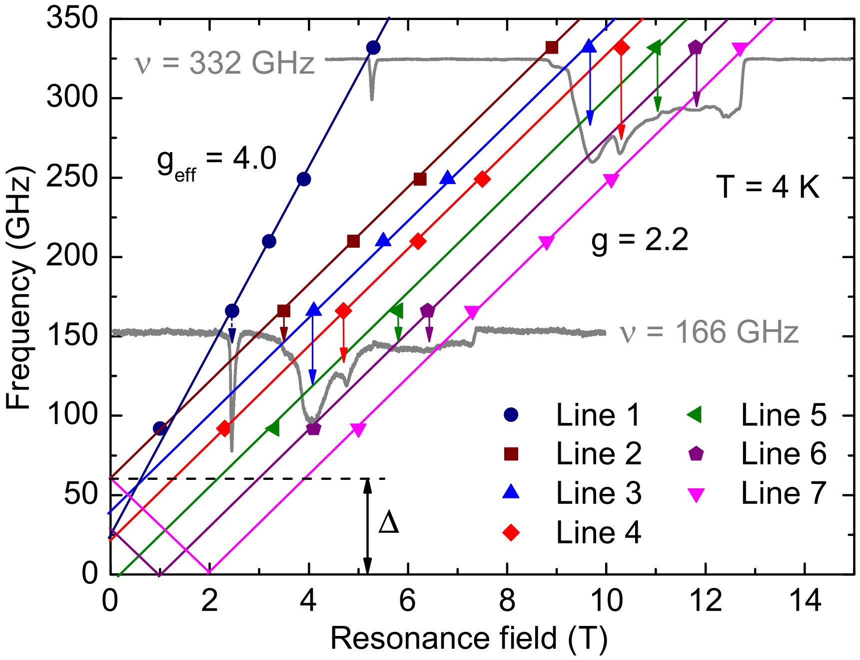

Figure 3.12: Frequency vs. resonance field $\nu(H_{\mathrm{res}})$-dependencies of the ESR resonance modes (resonance branches) for the Ni$_3$-complex at $T = 4\,\mathrm{K}$.

a large intramolecular coupling rendering the ground state well isolated from higher-spin multiplets.

Analysis

As it was mentioned before, the ESR spectrum of the Ni$_3$-complex at $T = 4\,\mathrm{K}$ contains only lines corresponding to the ground state of the molecule ($S_0^{\mathrm{tot}} = 1$). Therefore, the minimal effective spin Hamiltonian (3.3) describing only the ground state was used for the analysis of the ESR spectra. Based on the experimental data, it is assumed that each molecule has a single spin $S = S_0^{\mathrm{tot}} = 1$ with a g-factor of 2.2 and a magnetic anisotropy $\Delta = |D_S|(S^2 - (S-1)^2) = 60\,\mathrm{GHz}$. A simulated powder spectrum for $\nu = 166\,\mathrm{GHz}$ and $T = 4\,\mathrm{K}$ is presented in Fig. 3.14 b. Comparison of the calculated result (b) with the experimental ESR spectrum of a microcrystalline powder sample (a) on that Figure shows that the experimental data are well reproduced by the model. However, one can observe a slight difference between the simulated and measured spectra, such as different relative intensities of the lines 3 and 4. This difference can be attributed to a partial orientation (texturing) of the microcrystalline powder sample.

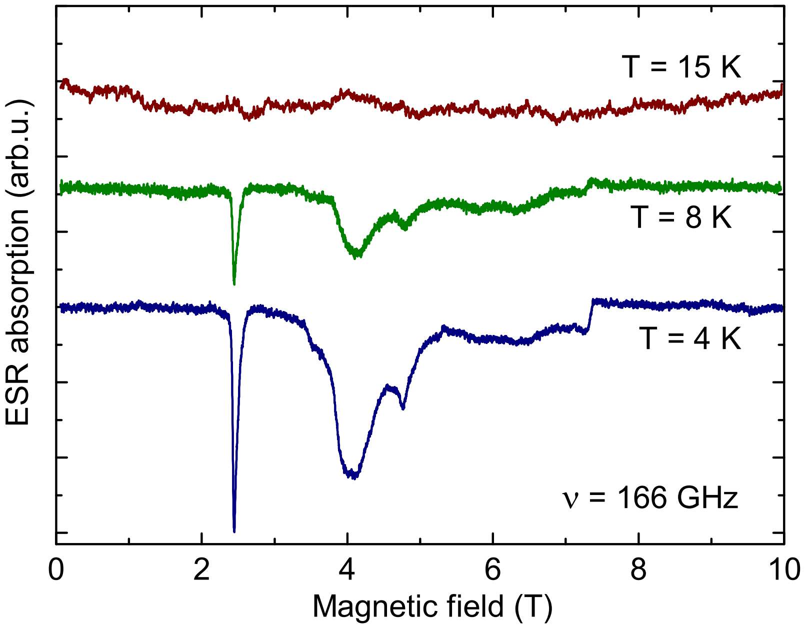

Figure 3.13: T-dependence of the ESR spectrum of the Ni$_3$-complex at $\nu = 166\,\mathrm{GHz}$.

The analysis demonstrates that the applied model describes the Ni$_3$-complex at low temperatures very well. In particular, the ground state of the molecule with $S_0^{\mathrm{tot}} = 1$ and the g-factor of 2.2 are confirmed. Moreover, the modelling yields a positive sign of the axial anisotropy $D_S = +60\,\mathrm{GHz}$ (2.9 K) and a substantial transverse anisotropy $E_S = 10\,\mathrm{GHz}$ (0.5 K) which implies an "easy plane" situation for the molecule with an easy axis in the plane. In addition, this analysis reveals that the ESR lines 2 - 7 correspond to "allowed" resonance transitions between neighboring energy levels according to the ESR selection rule $\Delta S_z = \pm 1$ and, therefore, the observed number of lines can be explained by the powder averaging of the ESR spectrum. Line 1 corresponds to the so-called "forbidden" transition with $\Delta S_z = \pm 2$ for which an almost doubled slope of the $\nu(H_{\mathrm{res}})$ branch is observed ($g_{\mathrm{eff}} \sim 2g$, see Fig. 3.12). A non-zero intensity of this transition indicates the mixing of the spin energy states due to the anisotropic ligand crystal field and the spin-orbit coupling.

The temperature dependence of the magnetic susceptibility of the Ni$_3$-complex can be analyzed by taking into account the topology of the Ni$_3$-core which suggests a single exchange coupling J' between the three Ni^{2+} ions via the sulphur bridges (cf. Fig. 3.4). Similar to the Ni$_2$-complex, for the simulation of $\chi(T)$, the parameters of the magnetic anisotropy were assumed to be equal for all three

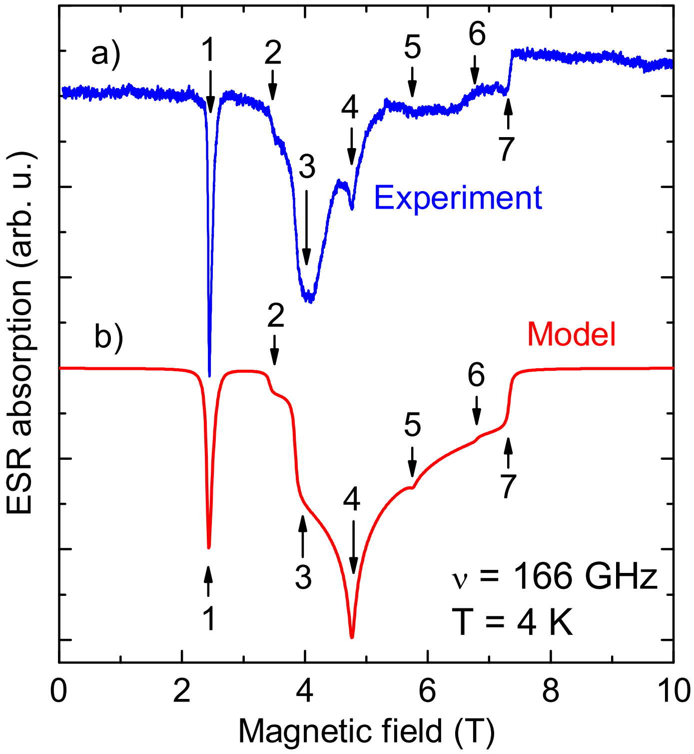

Figure 3.14: ESR spectra of the Ni_3-complex at $\nu = 166\,\mathrm{GHz}$ and $T = 4\,\mathrm{K}$: a) experimental spectrum; b) simulated spectrum.

ions and were taken as $D_{\mathrm{eff}} = D_S = 2.9\,\mathrm{K}$ and $E_{\mathrm{eff}} = E_S = 0.5\,\mathrm{K}$ from the analysis of the ESR spectra. The simulated $\chi(T)$ and $\chi^{-1}(T)$ dependencies fully reproduce the experimental results (cf. the black lines in Fig. 3.11) and reveal an antiferromagnetic (AFM) coupling $J' = 140\,\mathrm{K}$ between the Ni ions. The energy levels of the spin states of the Ni_3-complex, calculated according to the model, are shown in Fig. 3.15. This scheme illustrates the energy gap of 140 K between the ground state $S_0^{\mathrm{tot}} = 1$ and the first excited state $S_1^{\mathrm{tot}} = 2$ caused by the magnetic coupling J'. This result confirms that the strong non-linearity of $\chi^{-1}(T)$ in the temperature range $T = 100 - 150\,\mathrm{K}$ (cf. Fig. 3.11) is caused by the thermal activation of the higher energy spin multiplet ($S_1^{\mathrm{tot}} = 2$). Note, that the modelling reveals a rather large temperature independent diamagnetic component $\chi_0 = -3.9 \cdot 10^{-3}\,\mathrm{erg/G^2/mole}$ which is in agreement with a significant diamagnetic susceptibility of the organic ligands of the complex.

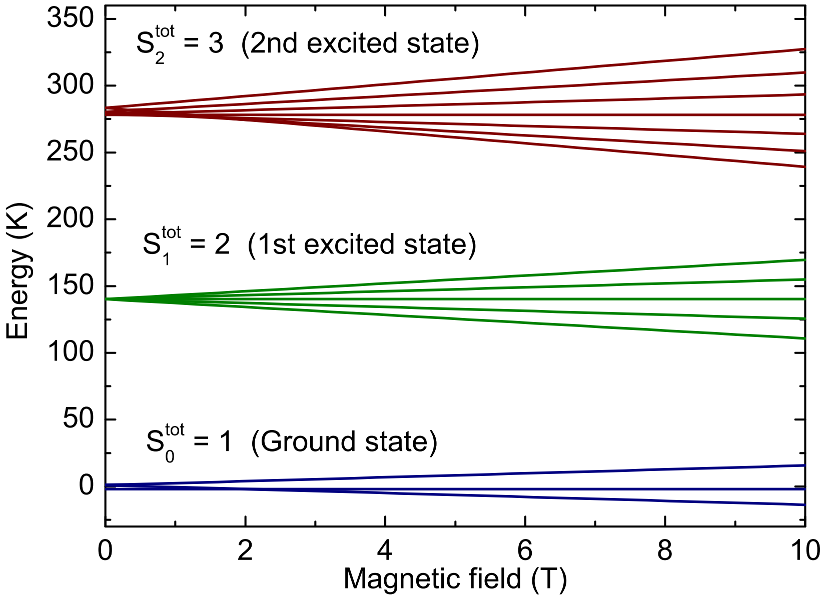

Figure 3.15: Calculated energy spectrum of the spin states of the Ni_3-complex.

3.1.4 Conclusion

The structural analysis of the Ni_2- and Ni_3-complexes reveals a totally different arrangement of the atoms in the two cores. In the Ni_3-core adjacent Ni ions are connected via one bridging thiophenolate sulphur atom, whereas in the Ni_2-core the metal ions are bridged by two S atoms which leads to very different Ni-S-Ni bridging angles in these two complexes. The large value of about 133° in the case of the Ni_3-complex is attributed to the fact that the Ni ions lie on opposite faces of the thiophenolate planes. The dinuclear Ni complex, on the other hand, has the Ni ions on the same side of the thiophenolate plane, and shows much smaller Ni-S-Ni angles. The values do not deviate much from 90°. As expected for such strongly different bonding geometries, the HF-ESR and magnetization data show different magnetic exchange interactions in these compounds. The Ni_2-complex reveals a ferromagnetic coupling $J = -42\,\mathrm{K}$, while for the Ni_3-complex we observe a strong antiferromagnetic coupling $J' = 140\,\mathrm{K}$. These differences can be attributed to the different Ni-S-Ni bridging bond angles.

Moreover, the different structure of the ligands in the Ni_3- and Ni_2-complexes causes opposite signs of the single ion magnetic anisotropy. Thus, in the Ni_3-complex the ligand structure yields a positive axial anisotropy and, therefore, an “easy plane” situation for the molecule. In contrast, for the Ni_2-complex we observe a negative axial anisotropy, which yields an “easy” magnetic anisotropy axis for the molecule and a bistable magnetic ground state.

Thus, the variation of the angles of the sulphur bridging bonds and of the ligand structure has a very strong impact on the magnetic properties of the studied Ni(II)-based complexes. Such a control of exchange interactions and single ion anisotropy suggests a pathway for a targeted assembly of single molecular magnetic complexes with predetermined magnetic properties.

3.2 Mn_2Ni_3 Single Molecular Magnet

The combination of different metal ions in a single cluster for achieving large magnetic anisotropy and high-spin ground states significantly extends the structural landscape for SMM. Mixed transition metal molecular magnetic complexes include MnCu [49], Mn_2Ni_2 [50, 51], $Mn_{11}Cr$, Fe_4Ni_4 [52], Mn_6Cr [53], and Mn_3Ni [54], some of them showing slow relaxation and quantum tunnelling of the magnetization. Recently, the synthesis of a new family of heterometal SMM has been started in the group of Prof. Meyer (University of Göttingen). These relatively small pentanuclear systems $[\mathrm{Mn}_2^{\mathrm{III}}\mathrm{Ni}_3^{\mathrm{II}}\mathrm{L}_4(\mathrm{LH})_2\mathrm{X}_2(\mathrm{H_2O})_2]$ (X = Cl/Br) feature a ferromagnetic $S_{\mathrm{tot}} = 7$ ground state, substantial uniaxial magnetic anisotropy, and pronounced quantum tunnelling steps in the magnetization hysteresis loops [55]. In the following, the detailed magnetic study of the first member in this new family of SMM will be described.

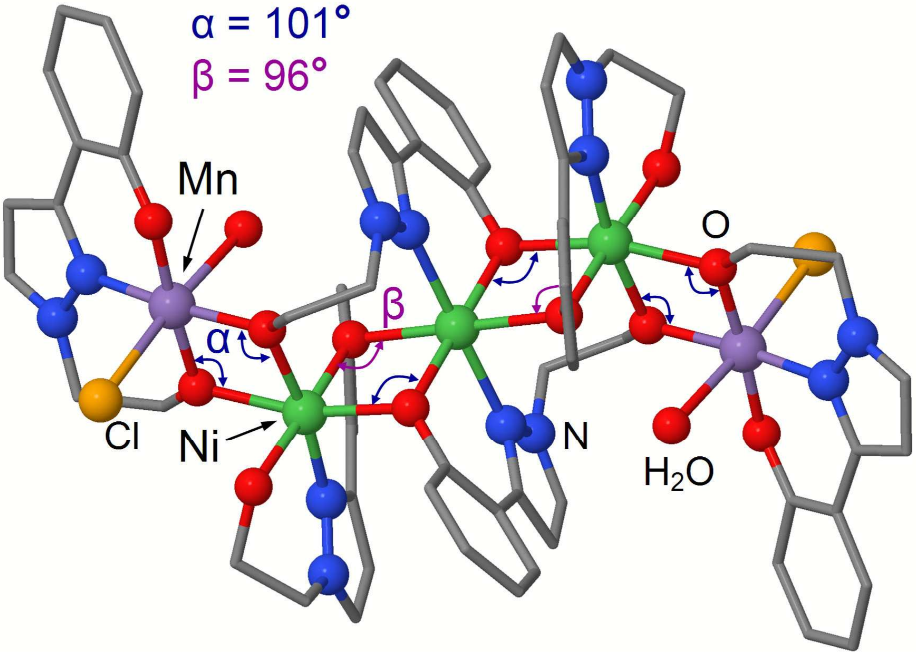

Figure 3.16: Molecular structure of the Mn_2Ni_3-complex. The complex has a $[Mn_2Ni_3(\mu\text{-}O)_8]$ core where two Mn^{3+} and three Ni^{2+} ions are bound by four double oxygen bridges.

3.2.1 Molecular Structure

The studied Mn_2Ni_3-complex was synthesized and characterized as described in Ref. [55]. Its molecular structure is presented in Fig. 3.16. The complex contains a $[Mn_2Ni_3(\mu\text{-}O)_8]$ core where the coordination number of all metal atoms is six and the coordination environment is distorted octahedral. Oxidation states of the metal ions, Mn^{3+} and Ni^{2+}, are confirmed by bond valence sum calculations [56] and by the relatively short bonds for the Mn^{3+} ions. The three Ni^{2+} ions are doubly bridged by phenoxy-O atoms, while both peripheral Mn^{3+} ions are linked to the Ni_3^{2+} core via double alkoxy-O bridging. Mn^{3+} ions are found in an NO_4Cl environment with the equatorial position occupied by the ONO site of a tridentate ligand and an alkoxo-O of another ligand, and with the terminal Cl and a water molecule in the axial positions. As expected, the Mn^{3+} ions exhibit a strong Jahn-Teller elongation along the Cl-Mn-OH_2 axis (Fig. 3.17 a) with Mn-O/Cl distances of 2.34/2.61 Å. In the case of nickel the octahedral environment is more regular featuring for the central Ni^{2+} a N_2O_4 and for two other Ni^{2+} NO_5 coordination spheres. With respect to the magnetic properties, it is also important to note that the Jahn-Teller axes of the Mn^{3+} ions at both ends of the

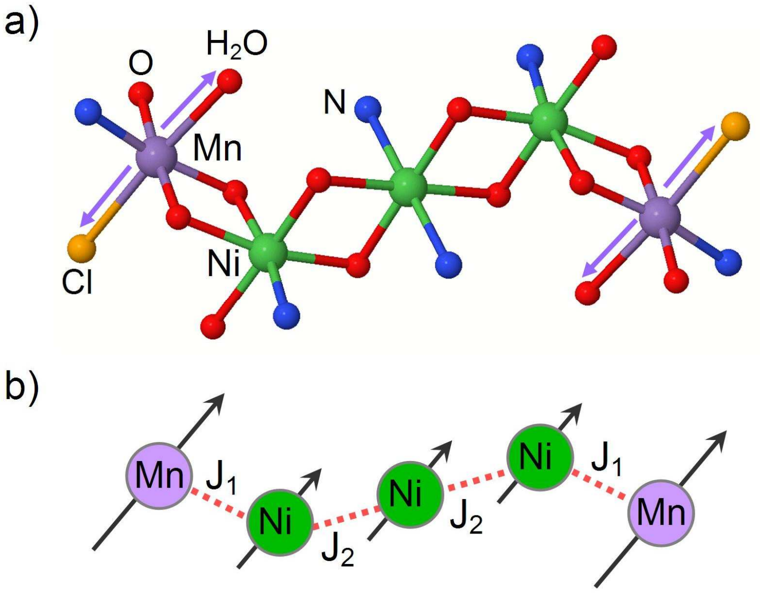

Figure 3.17: a) Coordination environment of the metal ions in the Mn_2Ni_3-complex. The arrows indicate the Jahn-Teller axes. b) Expected magnetic coupling between the spins in the Mn^{3+}-Ni^{2+}-Ni^{2+}-Ni^{2+}-Mn^{3+} core.

quasi-linear Mn^{3+}-Ni^{2+}-Ni^{2+}-Ni^{2+}-Mn^{3+} core are roughly parallel to each other. The topology of the core suggests two different exchange constants J_1 and J_2 for Mn-Ni and Ni-Ni interactions, respectively (cf. Fig. 3.17 b).

3.2.2 Static Magnetization

The static magnetic properties of the Mn_2Ni_3-complex were investigated using the magnetometer MPMS SQUID-VSM in magnetic fields $\mu_0 H$ up to 7 T at temperatures between 1.8 and 300 K. The results of the field-dependent magnetization $M(H)$ measurements for a polycrystalline powder sample at three different temperatures ($T = 1.8$, 4, 10 K) are shown in Fig. 3.18. The measurements reveal a saturation magnetization of about 14 μ_B per molecule, which corresponds to the magnetic ground state of the complex with a total spin $S_{tot} = 7$. This observation implies ferromagnetic (FM) coupling between the two Mn^{3+} ions ($3d^4$, $S_{Mn} = 2$) and three Ni^{2+} ions ($3d^8$, $S_{Ni} = 1$) as schematically illustrated in Fig. 3.17 b.

The temperature dependence of the static magnetic susceptibility $\chi(T)$ and inverse susceptibility $\chi^{-1}(T)$ of the Mn_2Ni_3-complex in a magnetic field of 1 T is presented in Fig. 3.6 (the measurements were performed by K. Gieb, University of Erlangen-Nuremberg). At high temperatures ($T > 100$ K), $\chi^{-1}(T)$ is linear

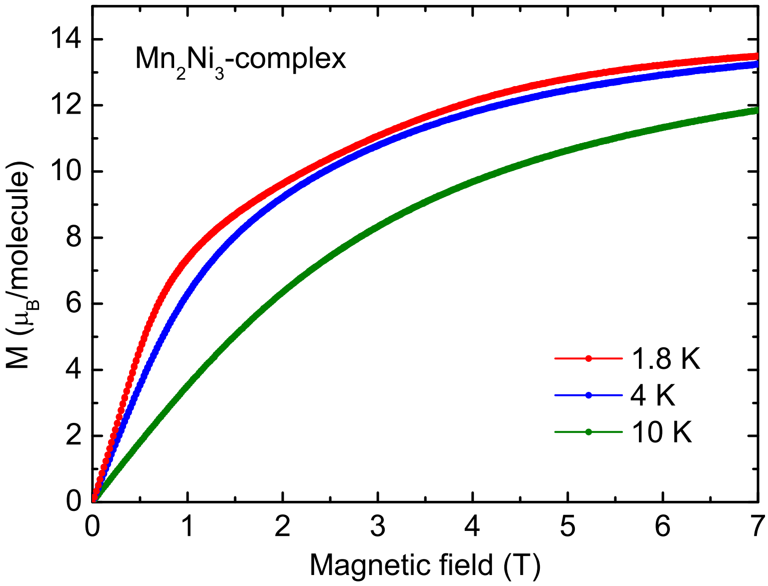

Figure 3.18: Field dependence of the static magnetization $M(H)$ of the Mn_2Ni_3-complex at different temperatures.

following the Curie-Weiss law, however, at $T < 100\,\mathrm{K}$, there is a strong non-linearity of $\chi^{-1}(T)$. Assuming an isotropic coupling between the spins with two different exchange constants (see Fig. 3.17 b), the experimental data can be fitted using the Heisenberg model. The effective spin Hamiltonian in this case can be given in the form

$$\begin{aligned}\mathcal{H} \;=\; & J_1(S_{\mathrm{Mn1}}S_{\mathrm{Ni1}} + S_{\mathrm{Mn2}}S_{\mathrm{Ni3}}) \;+\; J_2(S_{\mathrm{Ni1}}S_{\mathrm{Ni2}} + S_{\mathrm{Ni2}}S_{\mathrm{Ni3}}) \\ & + g\mu_{\mathrm{B}}\sum_{j=1}^{2}\mathbf{H}\cdot\mathbf{S}_{\mathrm{Mn}j} \;+\; g\mu_{\mathrm{B}}\sum_{j=1}^{3}\mathbf{H}\cdot\mathbf{S}_{\mathrm{Ni}j}\,. \qquad (3.5)\end{aligned}$$

Since the $\mathrm{Mn_2Ni_3}$-complex has a rather big number of spins (five), in order to simplify the model, the magnetic anisotropy terms were not included into the Hamiltonian. The neglect is also motivated by the fact that the magnetic anisotropy parameters are significantly smaller than the coupling constants (see ESR measurements). From the numerically calculated best fit, shown as black lines in Fig. 3.6, one obtains $J_1 \approx -44\,\mathrm{K}$ (FM) for the Mn-Ni coupling and $J_2 \approx -19\,\mathrm{K}$ (FM) for the Ni-Ni coupling constant and an average g-factor $g_{\mathrm{av}} = 2.06$ which is in a good agreement with the value directly measured by ESR, $g_{\mathrm{av}}^{\mathrm{ESR}} = 2.08$.

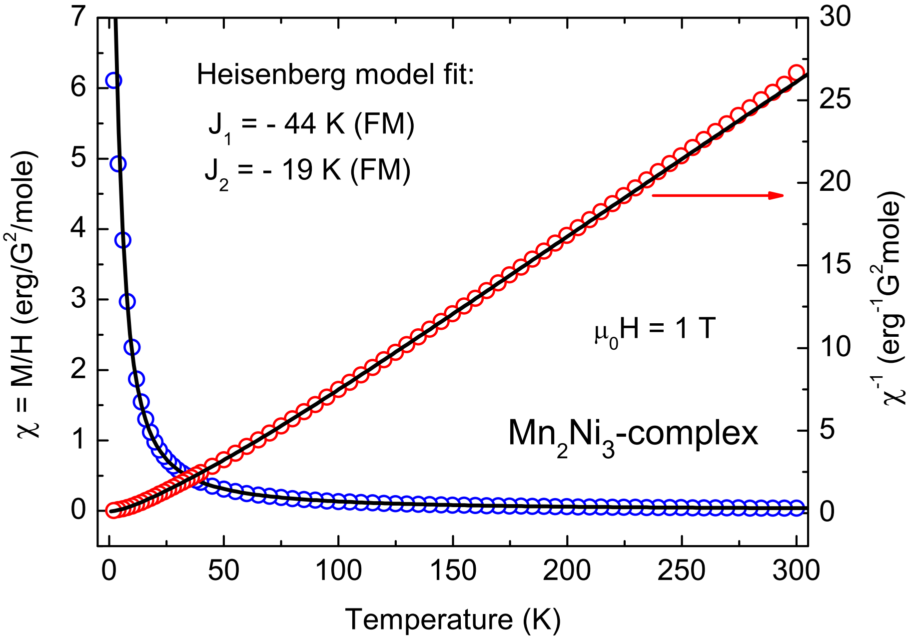

Figure 3.19: Temperature dependencies of the static susceptibility $\chi(T) = M(T)/H$ and the inverse susceptibility $\chi^{-1}(T)$ of the $\mathrm{Mn_2Ni_3}$-complex in $\mu_0 H = 1\,\mathrm{T}$ (open circles). The black lines represent a numerical model fit using the Hamiltonian (3.5).

3.2.3 High-Field Electron Spin Resonance

High-field electron spin resonance (HF-ESR) measurements in magnetic fields up to 15 T were performed by means of the MVNA (see chapter 2) on an oriented powder sample of the Mn_2Ni_3-complex. Owing to a strong magnetic anisotropy (see below) the single crystalline powder particles in the sample were aligned in the magnetic field along their crystalline magnetic anisotropy axis. Typical ESR spectra at $T = 20\,\mathrm{K}$ are shown in Fig. 3.20. The spectra feature a relatively simple structure consisting of well-defined and almost equally spaced absorption lines with a separation of the resonance fields H_{res} by $\sim 1\,\mathrm{T}$. Measurements at different excitation frequencies reveal a linear relationship between ν and H_{res} for each absorption line. The respective ν vs. H_{res} dependencies (resonance branches) are plotted together in Fig. 3.20. The slope of all resonance branches is almost identical. This enables a straightforward determination of the average g-factor

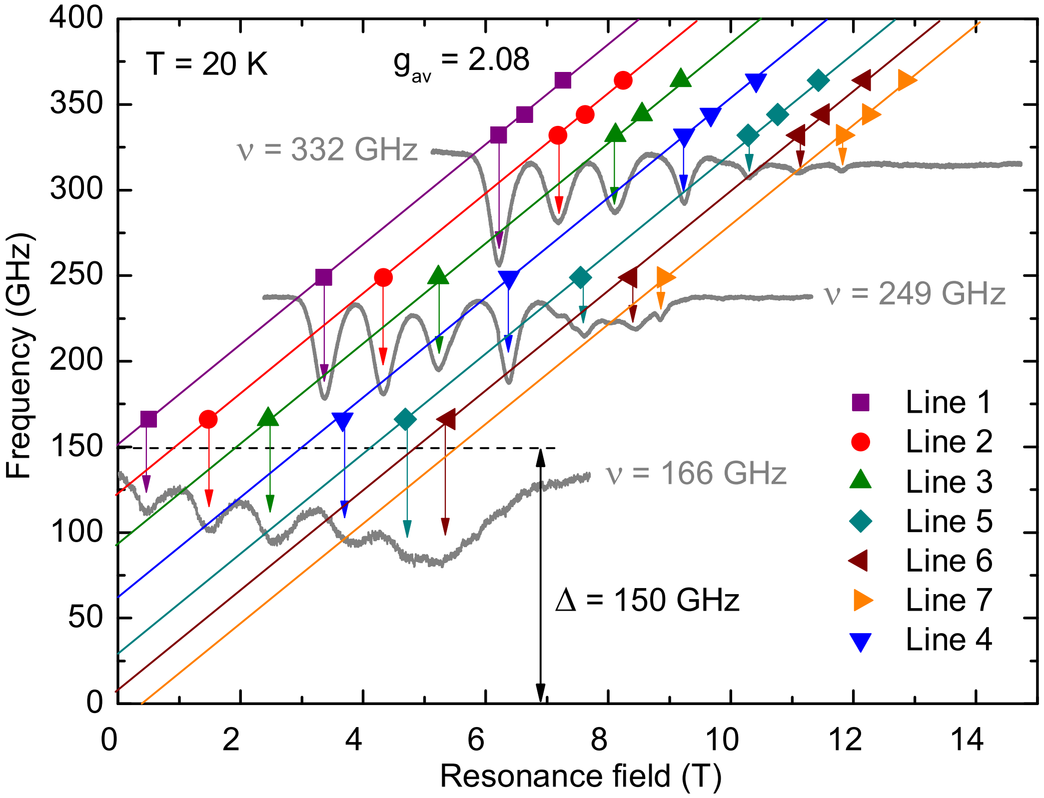

Figure 3.20: Frequency ν versus resonance magnetic field H_{res} dependence of the ESR lines (symbols) and representative ESR spectra of the Mn_2Ni_3-complex at $T = 20\,\mathrm{K}$. Solid lines are linear fits to the experimental data points.

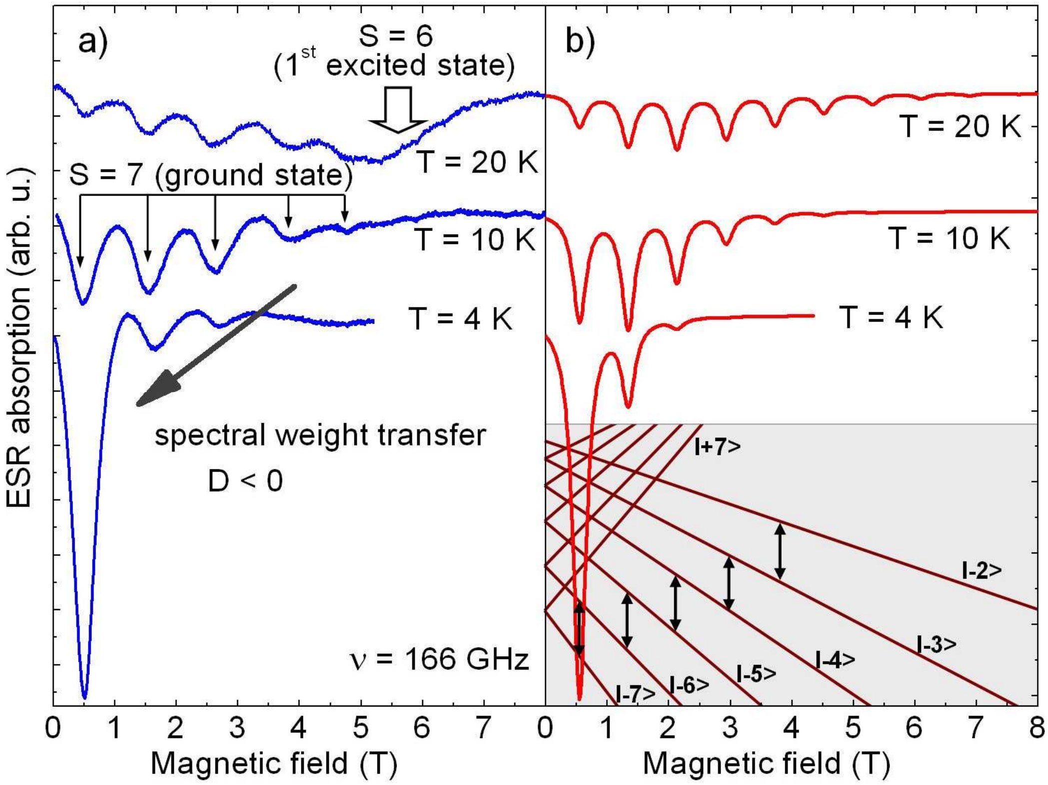

Figure 3.21: Temperature dependence of the ESR spectra of the Mn_2Ni_3-complex at $\nu = 166$ GHz. a) Experimentally obtained ESR spectra; b) ESR spectra and energy levels calculated using the simplest model (Eq. (3.6)), with the parameters obtained from the magnetization and ESR measurements ($S_{\mathrm{tot}} = 7$; $D_{\mathrm{mol}} = -0.55$ K; $g_{\mathrm{av}} = 2.08$).

$g_{\mathrm{av}} = 2.08$. As shown in Fig. 3.20 the extrapolation of the $\nu(H_{\mathrm{res}})$ dependence of the leftmost line in the ESR spectrum (line 1) to zero magnetic field yields the magnitude of the magnetic anisotropy gap Δ amounting to 150 GHz (~ 7.2 K). Since Δ is related to the anisotropy parameter D_{mol} of the molecular complex as $|D_{\mathrm{mol}}| = \Delta/(S_{\mathrm{tot}}^2 - (S_{\mathrm{tot}} - 1)^2)$, with $S_{\mathrm{tot}} = 7$ one obtains the absolute value $|D_{\mathrm{mol}}| = 11$ GHz (0.55 K) for the Mn_2Ni_3-complex.

The sign of D_{mol} can be unambiguously determined from the temperature dependence of the ESR spectrum which is presented in Fig. 3.21 a. Here, one observes a clear transfer of the spectral weight to lower magnetic fields at low temperatures whereas the positions of the absorption lines do not change. Such kind of redistribution of the ESR spectral weight occurs in the case of a spin doublet ground state $| \pm S_{\mathrm{tot}}^z\rangle$ corresponding to a negative sign of D_{mol}, whereas for the case of a singlet state $|0\rangle$, i.e., for a positive sign of D_{mol}, the spectral weight should shift to higher fields (ref. to section 1.3.1). This is illustrated by the energy level diagram in Fig. 3.21 b. For $D_{\mathrm{mol}} < 0$ and at low T, the lowest state $|-7\rangle$ is the most populated one yielding the strongest intensity for the leftmost line in the ESR spectrum. With increasing T, higher energy levels become more populated and therefore a larger number of ESR lines is observed. Thus the HF-ESR results give clear evidence for a bistable "easy axis" ground state of the Mn_2Ni_3-complex with a substantial anisotropy barrier $U = S_{\mathrm{tot}}^2|D_{\mathrm{mol}}| = 27$ K between the two degenerate ground states $S_{\mathrm{tot}}^z = +7$ and $S_{\mathrm{tot}}^z = -7$.

Using the experimentally-obtained parameters, the ESR spectra of the Mn_2Ni_3-complex were modelled for the case of the parallel orientation of the "easy axis" of the complex to the direction of the magnetic field, i.e., the situation which is expected for an oriented powder sample. This model, with the effective spin Hamiltonian

$$\mathcal{H} \;=\; D_{\mathrm{mol}}[(S_{\mathrm{tot}}^z)^2 - S_{\mathrm{tot}}(S_{\mathrm{tot}}+1)/3] \;+\; g_{\mathrm{av}}\mu_{\mathrm{B}} H S_{\mathrm{tot}}^z\,, \tag{3.6}$$

describes only the ground state of the molecule. Here, the first term describes the zero field splitting of the spin states caused by an anisotropic ligand crystal field, and the second term is the Zeeman interaction of the total spin with the external magnetic field H. As can be seen in Fig. 3.21 the simulation captures well the main features of the experimentally-observed ESR spectrum: the extent of the fine structure of the spectrum, the number of lines and their relative intensities. Discrepancies between the model and the experiment could be due to a non-perfect alignment of the powder particles as well as to the simplifications of the model which neglects intra- and intermolecular interactions. Beyond the model description, in the experimental ESR spectrum at $T = 20$ K an additional wide absorption line emerges at around 5.5 T (see Fig. 3.21 a). Since the temperature of 20 K is of the order of the intramolecular coupling between the spins, this feature can be, most probably, attributed to transitions inside the higher-energy spin multiplets.

3.2.4 Single Molecular Magnet Behavior

To further investigate the properties of the Mn_2Ni_3-complex, AC susceptibility measurements were performed. Furthermore, a micro-Hall-bar magnetometer was used in order to perform low-temperature single-crystal DC magnetization mea-

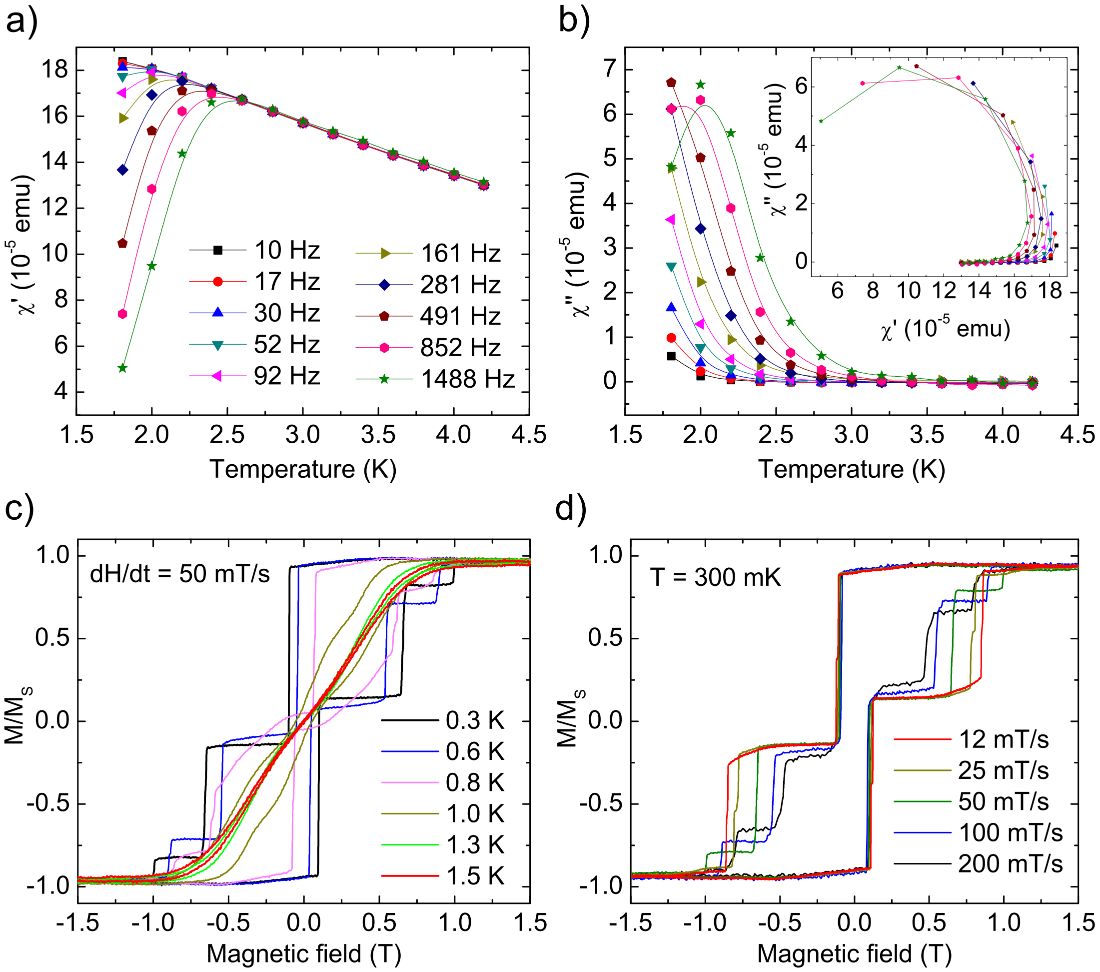

Figure 3.22: Top: AC susceptibility versus temperature for a powder sample of the Mn_2Ni_3-complex. a) In-phase component χ'; b) out-of-phase component χ''. The data were collected in an AC magnetic field of 2.56 Oe oscillating at the indicated frequencies. The inset in b) shows a Cole-Cole plot (χ'' vs. χ'). Bottom: Low-temperature DC magnetization measurements on a single crystal of the Mn_2Ni_3-complex performed by means of a micro-Hall-bar magnetometer. Measurements: a) at different temperatures; b) at different magnetic field sweep rates.

surements. Both kinds of measurements were done at the University of Erlangen-Nürnberg by the group of Prof. Müller.

The results of the AC susceptibility measurements on a microcrystalline powder sample are shown in Fig. 3.22 a,b. The inset in Fig. 3.22 b is a so-called Cole-Cole (Argand) plot. The dispersion data presented in this way reveal an almost perfect semi-circle. This is clear evidence of a relaxation process with a single relaxation time τ_0 [11] and suggests SMM behavior of the studied complex.

For the low-temperature DC magnetization measurements, the crystals were oriented with the easy axis approximately parallel to the applied magnetic field. Measurements were performed at several temperatures in the range of 0.3 - 1.5 K (Fig. 3.22 c), and magnetic field sweep rates in the range of 12 - 200 mT/s (Fig. 3.22 d). These measurements reveal a hysteretic behavior of the magnetization below the blocking temperature T_B of approximately 1.5 K and sharp steps indicating flipping of the magnetization vector due to quantum tunnelling.

An exemplary low-temperature hysteresis loop of the Mn_2Ni_3-complex measured at 300 mK and a field sweep rate of 200 mT/s is compared in Fig. 3.23 with the energy level scheme of the ground state multiplet calculated using the above described model, Eq. (3.6). The model qualitatively describes the main features of the magnetization behavior such as the number and the approximate positions of the relaxation steps which correspond to the level crossing points in the diagram. The correspondence between the crossing points and the positions of the steps is closest for the highest sweep rate of the magnetization measurement and

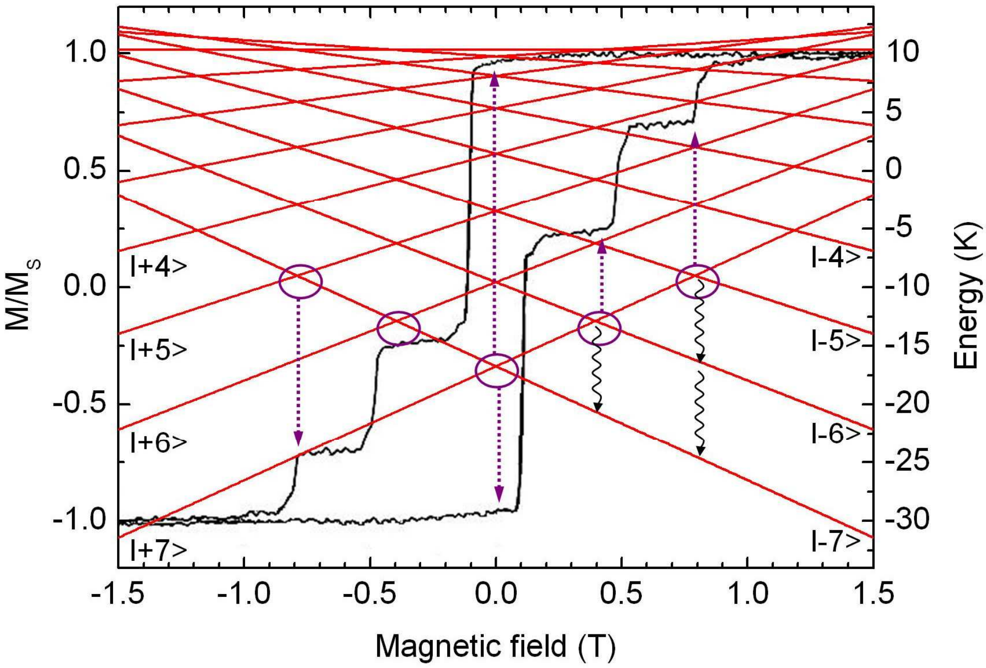

Figure 3.23: Magnetization vs. DC magnetic field hysteresis loops for a single crystal of the Mn_2Ni_3-complex measured at $T = 300$ mK and a field sweep rate of 200 mT/s (black line), together with the calculated energy level scheme.

gets worse for smaller sweep rates. Indeed, the rate of the spin flips in the ESR experiment is determined by the excitation frequency and orders of magnitude higher. Thus the level diagram derived from the ESR data should correspond to a magnetization measurement performed at a virtually infinite sweep rate.

Note that the observed sweep rate dependence of the relaxation steps positions and the fact that the first step in the hysteresis loop is above the zero crossing of the magnetic field cannot be described by the applied model. It is reasonable to assume that these features are mainly determined by relaxation paths caused by a ferromagnetic intermolecular interaction. Possibly owing to the smallness of intermolecular interactions in comparison with the measurement temperature and broadness of the absorption lines the ESR spectra do not exhibit characteristic splitting of the resonance lines due to the exchange bias as, for example, it was observed by Hill et al. in an exchange-coupled dimer of Mn_4 single molecular magnets [57].

3.2.5 Conclusion

The studied heterometallic Mn_2Ni_3-complex exhibits relatively strong ferromagnetic intramolecular couplings of 44 K and 19 K between Mn-Ni and Ni-Ni ions, respectively. This yields a high-spin ground state for the molecule with the total spin $S_{\mathrm{tot}} = 7$. A substantial uniaxial magnetic anisotropy with an energy barrier to thermal relaxation of the magnetization $U = 27\,\mathrm{K}$ is observed, leading to a SMM behavior of the studied complex. Noteworthy are the pronounced quantum tunnelling steps in the hysteresis curve of the magnetization, which are partially described by the simple model based on the ESR measurement results.

3.3 Mn(III) Single Chain Magnet

Besides single molecular magnets (SMM), single chain magnets (SCM) [58–61] are also attracting high attention. In general, these materials are composed of well-isolated ferro- or ferrimagnetic chains usually based on transition metal ions. Similarly to SMM, highly anisotropic ligand electrical fields yield a strong negative uniaxial anisotropy and therefore a slow relaxation of the magnetization below the so-called "blocking temperature".

One of the families of 1-dimensional magnetic systems are coordination polymers composed of Mn-porphyrine and radical molecule pairs. Many such compounds may be obtained by various ligand substitutions and their magnetic properties may be tuned in a broad range [62–65]. Recently, Mn(III) tetra(*ortho*-fluorophenyl)porphyrin-tetracyanoethylene was synthesized and characterized and its magnetic properties were reported in Ref. [61]. This compound consists of ferrimagnetic chains, in which magnetic moments of the Mn^{3+} ions ($S = 2$) in the center of porphyrin discs and of tetracyanoethylene radicals, TCNE^{-} ($s = 1/2$) are antiferromagnetically coupled with the exchange constant of $J_{\mathrm{AFM}}^{ortho} = 217\,\mathrm{K}$ [61]. At low temperatures, slow magnetic relaxation (below 13 K) and irreversible magnetic behavior (below 4.5 K) were observed. For such compounds, special attention is paid to the fluorine atom which can be attached at different positions of the phenyl rings. It is interesting to see how the strongly electronegative fluorine ions influence the magnetic exchange and the anisotropy of the Mn(III) ions. Therefore, the same group of chemists synthesized the Mn(III) tetra(*meta*-fluorophenyl)porphyrin-tetracyanoethylene with the *meta*-position of the fluorine ion. The goal of this study was the magnetic characterization of the Mn(III)-*meta*-compound in order to check its SCM properties and to probe the influence of the position of the fluorine ion on the magnetic behavior of the Mn(III)-chains.

3.3.1 Crystal Structure

The crystallographic structure of the studied Mn(III)-chain, as determined by X-ray analysis, is shown in Fig. 3.24. The structure belongs to the monoclinic space group C_2/c with four crystallographically equivalent porphyrin-TCNE molecular pairs in the elementary crystal cell. These molecular pairs are alternatively ordered along two symmetry related chains running along two diagonals of the *ab* crystal cell wall. The angle between these diagonals is 66°. The manganese ions

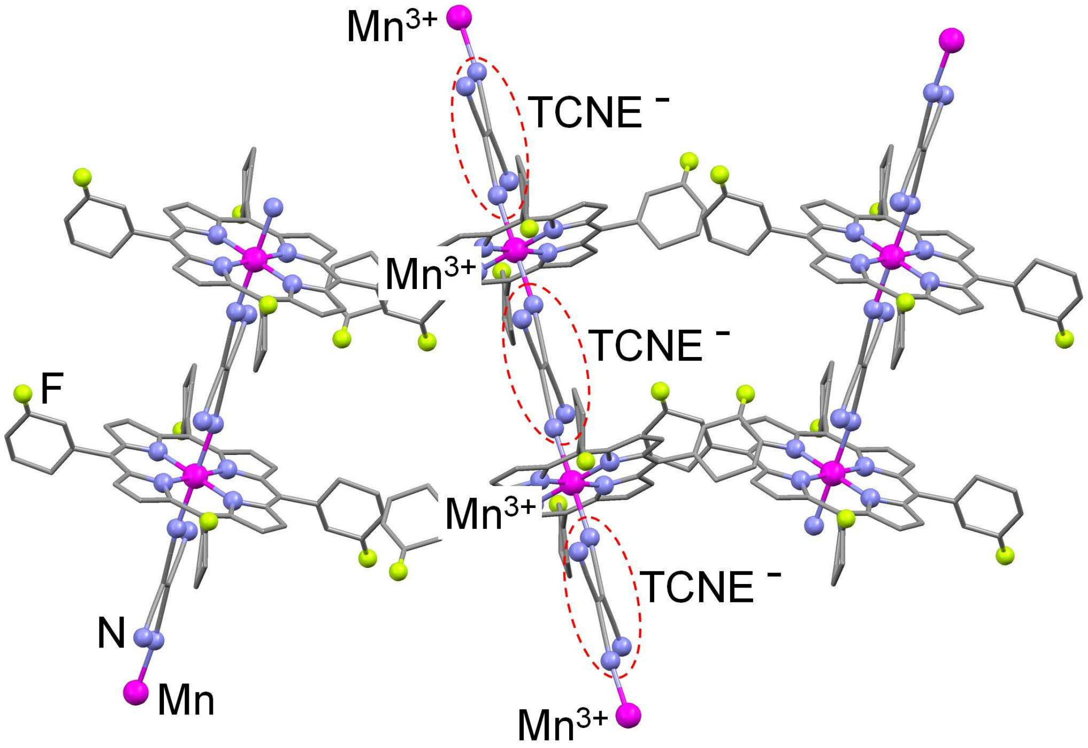

Figure 3.24: Structure of the Mn(III)-chain and packing of the chains in a crystal.

are located in the inversion centers. The surrounding of the Mn ions is an N_6 axially-distorted octahedra. The Mn-N distance is 2.008 Å and 2.013 Å in the porphyrin plane, and 2.327 Å perpendicular to the plane.

Samples. The samples were provided in two forms: microcrystals and fine powder. The microcrystals have an elongated shape with a maximum grain size of 0.5 mm. The fine powder corresponds to crystals which were ground in order to minimize the shape anisotropy. Through-out this section the microcrystalline sample is named as "crystalline" and the fine powder sample as "powder".

3.3.2 Static Magnetization

Static magnetization measurements on the Mn(III)-chain were performed on both "powder" and "crystalline" samples. Firstly, the magnetic field dependent magnetization measurements $M(H)$ were done on the "powder" sample at $T = 4.2\,\mathrm{K}$ in magnetic fields up to 5 T by means of the MPMS XL5 SQUID magnetometer. The result of these measurements is shown in Fig. 3.25 as blue circles. Since

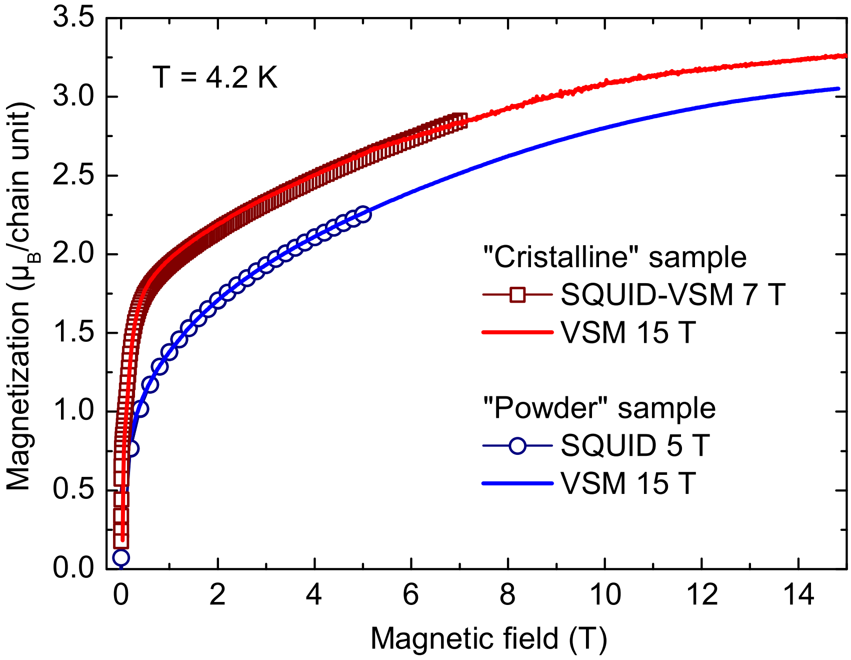

Figure 3.25: Magnetic field dependence of the static magnetization $M(H)$ of the "powder" sample (blue) and the "crystalline" sample (red). The saturation of magnetization is not reached even in a magnetic field of 15 T.

in the magnetic field of 5 T the magnetization of the sample is far from saturation, measurements in higher magnetic fields were necessary in order to study the ground state of the Mn(III)-chain. Measurements in magnetic fields up to 15 T were performed on the same sample at the same temperature ($T = 4.2\,\mathrm{K}$) by means of a home-made VSM (see chapter 2). The obtained data (blue line in Fig. 3.25) are in a very good agreement with the SQUID results. The absence of the complete saturation even at 15 T implies a need for higher magnetic fields.

Another possibility to reach the saturation at moderate fields is to use the "crystalline" sample which could be partially oriented either due to the shape anisotropy of the microcrystals (texturing of the sample) or self-oriented in a magnetic field due to the magnetic anisotropy. The measurement results on the "crystalline" sample of the Mn(III)-chain are shown in Fig. 3.25 in red color. The magnetization increases steeper at low magnetic field as compared to the powder sample. This behavior confirms the expected orientation of the microcrystals. However, saturation is not reached for the "crystalline" sample either, therefore measurements in higher magnetic fields are definitely required.

In the framework of collaboration with the Dresden High Magnetic Field Lab-

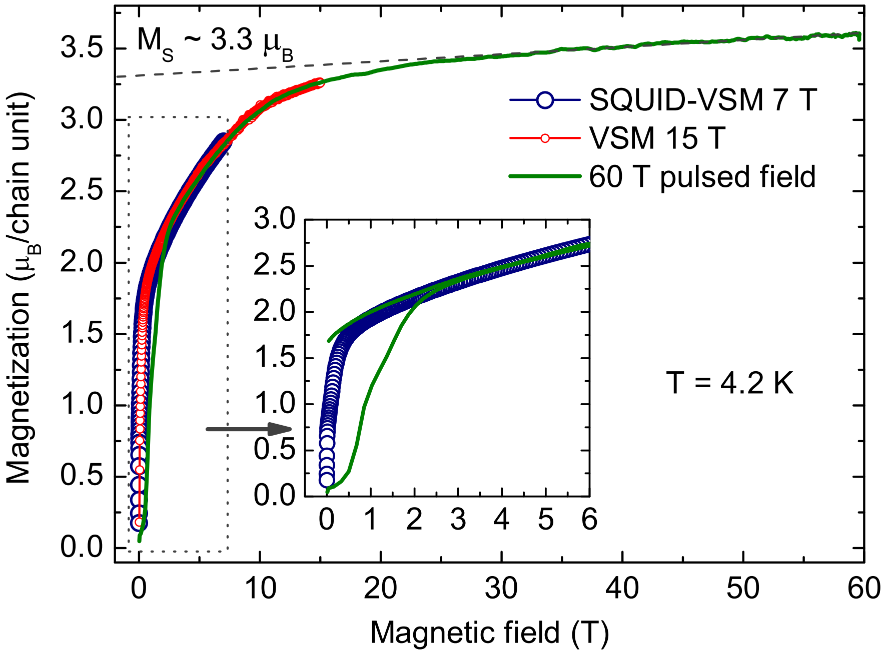

Figure 3.26: $M(H)$ of the "crystalline" sample in the magnetic fields up to 60 T. Inset: different behavior of the magnetization during the quasi-static DC and pulsed-field measurements.

oratory (HLD) at the Rossendorf Research Center, measurements of $M(H)$ up to 60 T in pulsed magnetic fields were performed. The obtained $M(H)$ curve for the "crystalline" sample at $T = 4.2\,\mathrm{K}$ is presented in Fig. 3.26 together with the results from the SQUID and VSM measurements. Here, it seems that the saturation of magnetization is not reached even at 60 T, however, from $\sim 30\,\mathrm{T}$, the magnetization grows linearly. This behavior can be treated as the interplay of three phenomena linear with the field: diamagnetism, Van Vleck paramagnetism and the breaking of antiferromagnetic couplings within the chain. Note that the background of the pulsed-field measurements might also give a contribution. Subtraction of these linear effects gives a saturation magnetization value of $3.3\,\mu_\mathrm{B}$ per chain unit. Taking the g-factor of 1.8 from the ESR measurements (see below), the effective spin value $S_\mathrm{eff} = 1.83$ was found for the Mn^{3+}-TCNE^{-} chain unit. This value is slightly larger than the expected $S = 3/2$ in case of antiferromagnetic coupling between the Mn spin $S_\mathrm{Mn} = 2$ (Mn^{3+} in high-spin state) and the radical spin $s = 1/2$. However, in case of ferromagnetic coupling between Mn and radical spins the effective spin value would be $5/2$ which is significantly larger than the experimentally observed $S_\mathrm{eff} = 1.83$.

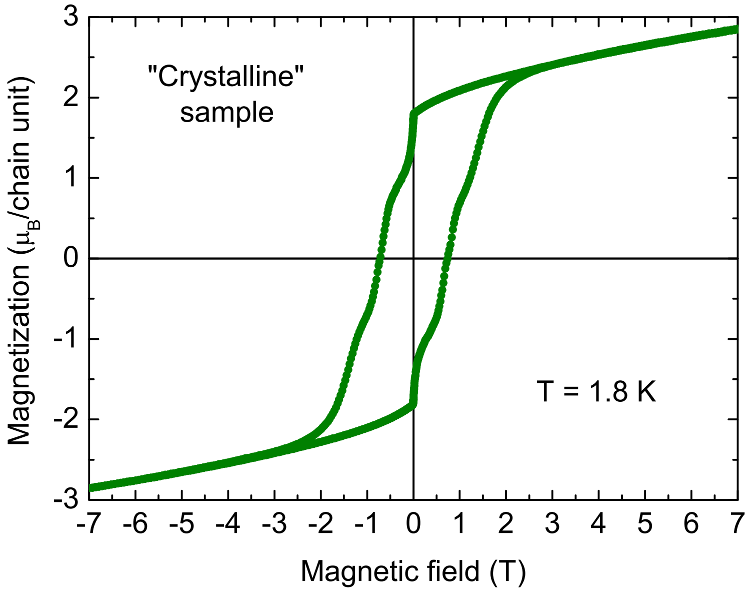

Figure 3.27: $M(H)$ of the “crystalline” sample at $T = 1.8\,\mathrm{K}$. The sample possesses a pronounced hysteresis. (measured quasi-statically)

The inset in Fig. 3.26 shows that the measurement results obtained during the quasi-static DC and pulsed-field measurements differ at magnetic fields below 2 T. In DC field measurements at $T = 4.2\,\mathrm{K}$, the sample shows no visible hysteresis, while in pulsed-fields there is a clear evidence for a hysteretic behavior of the magnetization. This indicates a slow relaxation of the magnetization of the Mn(III)-chain which is not visible on the time scale of DC measurements at $T = 4.2\,\mathrm{K}$, but becomes significant in the pulsed-field experiments, for which the pulse length is 30 ms.

In order to prove that the system has a slow relaxation of the magnetization, DC magnetization measurements at a low temperature $T = 1.8\,\mathrm{K}$ were done. As it can be seen from Fig. 3.27, the studied sample possesses pronounced hysteretic properties which imply a rather large magnetic anisotropy in the Mn(III)-chain. Moreover, reproducible steps in the magnetization curve are observed. The nature of these steps cannot be exactly deduced from these measurements, however the fast relaxation that corresponds to these steps is probably a sign of quantum tunnelling of the magnetization.

To study the magnetic properties of the Mn(III)-chain at higher temperatures and possibly estimate the intra-chain magnetic coupling of the spins, the temperature dependence of the static magnetization was measured on the “crys-

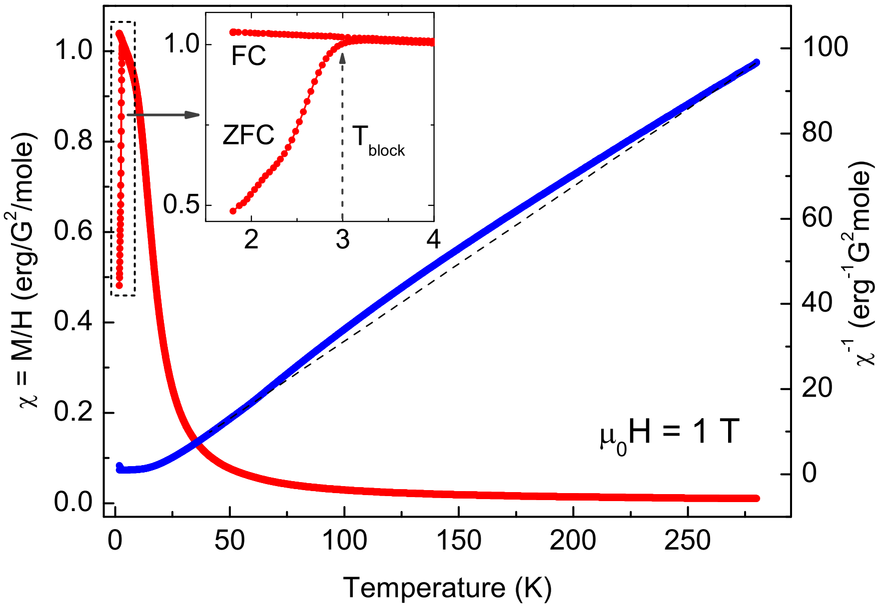

Figure 3.28: Temperature dependence of the static susceptibility $\chi(T) = M(T)/H$ (red) and inverse susceptibility $\chi^{-1}(T)$ (blue) of the Mn(III)-chain in a magnetic field of 1 T. Inset: difference between ZFC and FC measurement results.

talline" sample. Figure 3.28 presents the temperature dependence of the static susceptibility $\chi(T) = M(T)/H$ (red) and inverse susceptibility $\chi^{-1}(T)$ (blue). The inset focuses on the difference between the zero-field-cooled (ZFC) and field-cooled (FC) measurement regimes. In the ZFC case the sample was cooled down to 1.8 K in zero magnetic field, and, after applying the magnetic field of 1 T, the magnetization measurements were performed upon warming. For the FC measurements the sample was cooled in the same magnetic field and the magnetization was measured in the warming cycle. The difference between ZFC and FC results indicates the slow relaxation of the magnetization and allows to estimate the blocking temperature $\mathrm{T}_{\mathrm{block}}$ of around 3 K. This is in agreement with the observed hysteresis at $T = 1.8$ K and its absence at $T = 4$ K.

A non-linear behavior of $\chi^{-1}(T)$ is observed in the whole range of measurement temperatures (1.8 - 280 K). At temperatures above ~ 50 K, the inverse susceptibility curve shows clear evidence for the activation of higher energy spin states. This observation supports the expected antiferromagnetic AFM coupling J_{AFM} of the TCNE$^-$ radicals and Mn^{3+} ions spins in the Mn(III)-chain (Fig. 3.24). In order to get the exact value of the coupling energy a numerical simulation would be necessary. Below ~ 50 K, the curvature of the $\chi^{-1}(T)$-dependence indicates ferromagnetic interactions which could be probably attributed to a ferromagnetic coupling J_{FM} between effective Mn^{3+}-TCNE^{-} chain units.

3.3.3 Electron Spin Resonance

High-field/frequency electron spin resonance measurements on the M(III)-chain were performed in the frequency range $\nu = 332$ - 648 GHz and in magnetic fields up to 15 T by means of the MVNA (see section 2.1). Typical ESR spectra of the "powder" sample at $T = 4$ K and frequencies of 372, 440 and 528 GHz are shown in Fig. 3.29. Each spectrum comprises an intense absorption line (line 1) and several partially resolved weak satellite peaks on the high-field side of line 1 (lines 2 - 4). Variation of the excitation frequency ν yields a systematic parallel shift of the position H^i_{res} of all lines, $i = 1$ - 4. The dependencies ν_i vs. H^i_{res} (resonance branches) for all observed ESR lines are plotted in Fig. 3.29. The slopes of the branches are practically the same yielding a common g-factor of 1.8. This implies a common origin of the main absorption line and the satellites. A

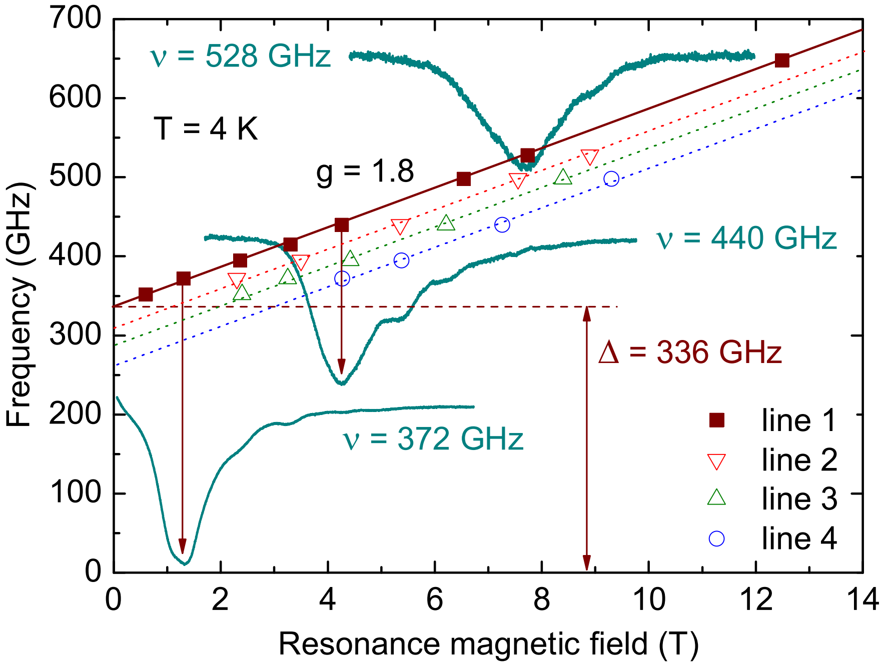

Figure 3.29: Frequency vs. resonance magnetic field diagram $\nu(H_{res})$ and representative ESR spectra of the "powder" sample of the Mn(III)-chain at $T = 4$ K

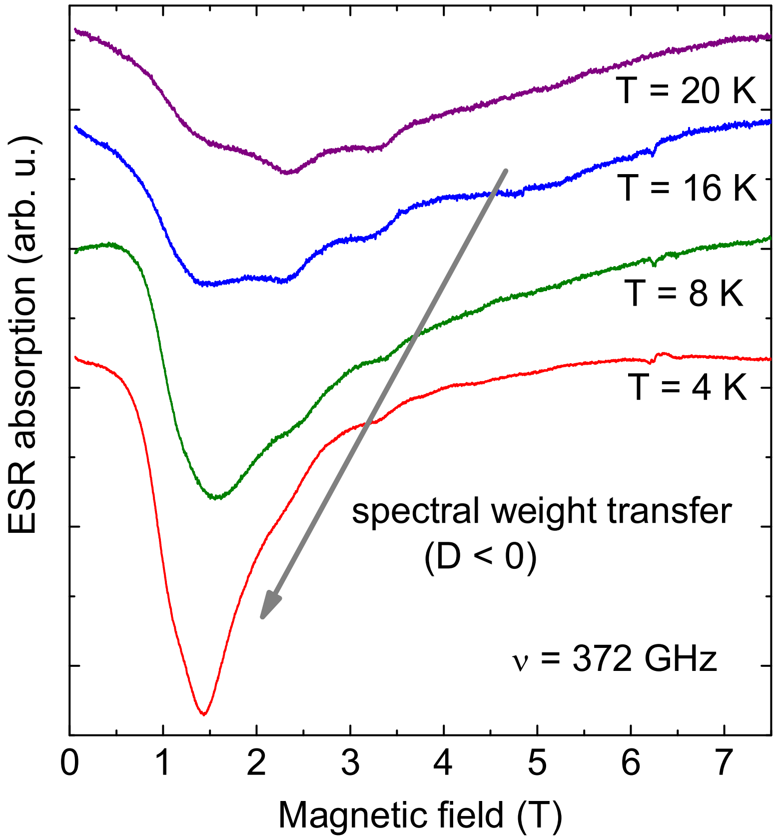

Figure 3.30: Temperature dependence of the ESR spectrum of the "powder" sample of the Mn(III)-chain at a frequency of 372 GHz.

linear extrapolation of the leftmost resonance branch (line 1) to zero magnetic field yields an anisotropy gap $\Delta = 336\,\text{GHz}$ (17 K) which is directly connected with the effective magnetic anisotropy of the chain. The occurrence of almost equidistant lines in the ESR spectrum gives evidence for the zero-field splitting of the S_z energy states due to the ligand electrical field and the spin-orbit coupling. However, in the case of an infinite chain the presence of satellite lines is not expected. Therefore, these lines probably indicate that in the "powder" sample the chains are not infinite.

A representative set of the ESR spectra of the "powder" sample at a fixed frequency $\nu = 372\,\text{GHz}$ and at different temperatures is presented in Fig. 3.30. An appreciable change of the relative intensities of lines 1 - 4 with temperature is observed. Here, a transfer of the spectral weight to higher magnetic fields at higher temperatures takes place whereas the position of each line is preserved. Such a transfer is a result of the thermal activation of the higher energy spin

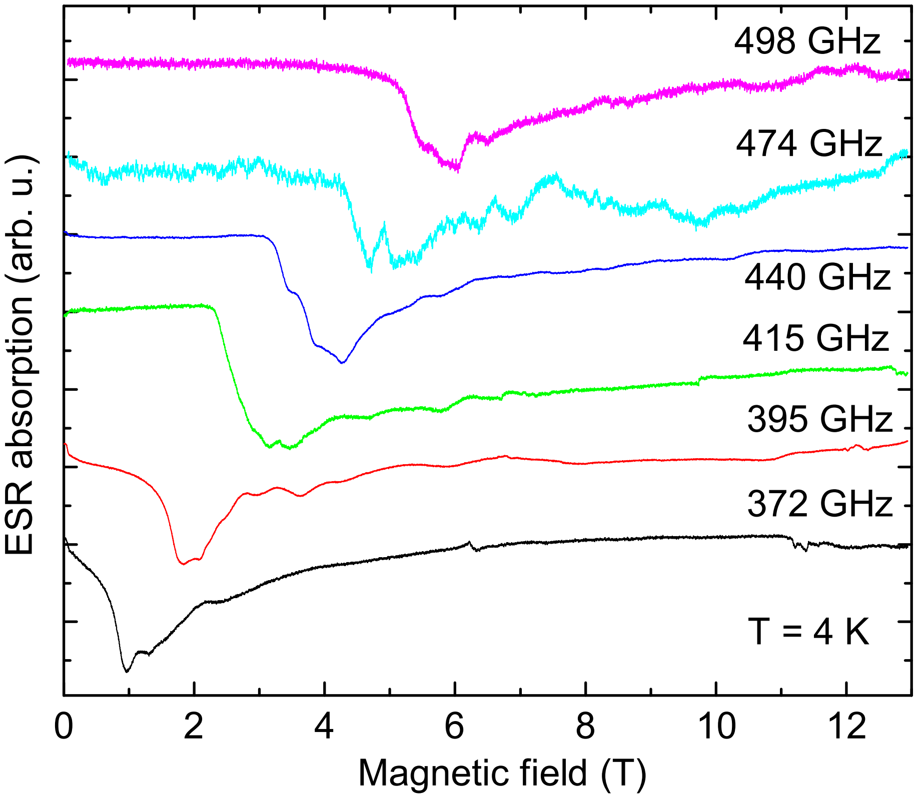

Figure 3.31: The ESR spectra at different frequencies obtained on the ground and pressed "crystalline" sample. The spectra are not well reproducible due to the reorientation of the microcrystalline particles in external magnetic fields.

states with rising temperature and indicates a negative sign of the axial magnetic anisotropy ($D < 0$) of the chain corresponding to an "easy axis" bistable ground state.

Since the magnetization measurements showed a difference between the "powder" and "crystalline" samples of the Mn(III)-chain (Fig. 3.25), the ESR measurements were performed on the "crystalline" sample, too. However, it was not possible to obtain reproducible ESR spectra most probably due to the reorientation of the microcrystalline particles during each field sweep. The only possibility was to slightly grind and press the sample. The ESR spectra obtained after this procedure are shown in Fig. 3.31. Though the spectra were still not perfectly reproducible, it was possible to estimate the position of the main line and to plot its $\nu(H_{\mathrm{res}})$-dependence. This data yields a g-factor of 1.8 which is the same as in the case of the "powder" sample. The value of the anisotropy gap was found to be 350 GHz which is slightly higher than for the "powder" sample. This might be connected with the inaccurate determination of the resonance line positions due to the rather large line width in the case of the "powder" sample and the less meaningful ESR spectra in the case of "crystalline" sample.

3.3.4 Conclusion

The Mn(III) tetra(*meta*-fluorophenyl)porphyrin-tetracyanoethylene was studied by means of static magnetization measurements up to 60 T and HF-ESR spectroscopy. The chain possesses a hysteretic behavior below the blocking temperature $T_{\mathrm{block}} \approx 3\,\mathrm{K}$ which is a clear property of a single chain magnet. The observed saturation magnetization yields an effective spin $S_{\mathrm{eff}} = 1.83$ which is slightly larger than the expected $S = 3/2$ in case of antiferromagnetic coupling J_{AFM} between the Mn spin ($S_{\mathrm{Mn}} = 2$) and the radical spin ($s = 1/2$). HF-ESR measurements revealed a magnetic anisotropy gap $\Delta = 17\,\mathrm{K}$ and a g-factor of 1.8. Moreover, the observed changes in the shape of the ESR spectrum at different temperatures indicate the axial nature of the magnetic anisotropy which is in agreement with the observed hysteretic behavior of the magnetization. The observed blocking temperature $T_{\mathrm{block}} \sim 3\,\mathrm{K}$ in the case of the Mn(III)-*meta*-compound is remarkably lower than the one observed for the Mn(III)-*ortho*-chain ($T_{\mathrm{block}}^{ortho} \approx 4.5\,\mathrm{K}$). Thus, the position of the fluorine ion has a significant influence on the magnetic anisotropy in the Mn(III)-chains.

3.4 Binuclear Mn(I) Complexes

Electronic structure and magnetic properties of Mn-containing compounds continue to be a major research area because of the fascinating physical properties observed in these materials, such as single molecule magnetism of multinuclear Mn complexes [66–68], or colossal magnetoresistance of manganese-based perovskite oxides [69]. These properties are closely related to the diversity of oxidation states and the effective exchange coupling between Mn ions provided by different short bridging ligands, such as O^{2-}, OH^-, CN^-, N_3^-, $RCOO^-$, $C_2O_4^{2-}$, pyrazolate [70, 71]. Surprisingly, no enough data on the magnetism of complexes containing Mn^{+1} ions is available though in this oxidation state it is isoelectronic to Fe^{+2} that is often found in a magnetic high spin (HS) state. The Mn^{+1} ion could be used for construction of molecular magnets by combining it with bridging ligands capable of charge transfer. In this respect the 1,2-diphospha-3,4,5-triphenylcyclopentadienide anion should combine the ability to bridge metal atoms with the feasibility of charge transfer that may lead to new interesting magnetic properties of Mn based metal-organic complexes. With the aim to investigate this interplay a series of binuclear Mn(I) complexes has been prepared in the A. E. Arbuzov Institute of Organic and Physical Chemistry in Kazan by the group of Dr. Miluykov. This section of the thesis describes the detailed magnetic study of

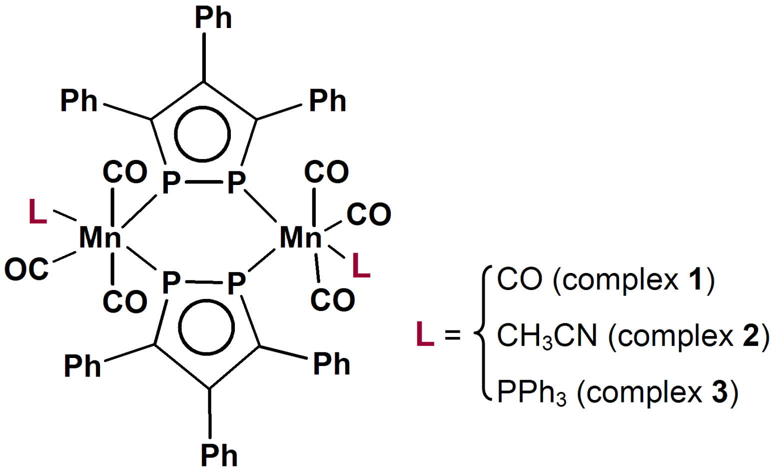

Figure 3.32: Chemical formula of the Mn dimer complexes. Two Mn atoms are doubly bridged by 3,4,5-triphenyl-1,2-diphosphacyclopentadienyl ligands. The ligand L is different for the tree studied complexes; L = CO (complex **1**); L = CH_3CN (complex **2**); L = PPh_3 (complex **3**).

three binuclear Mn(I) complexes by means of static magnetization measurements as well as continuous wave (CW) and pulse electron spin resonance.

3.4.1 Molecular Structure

Three studied binuclear Mn complexes were prepared as described in Ref. [72]. Fig. 3.32 presents the chemical formula for these complexes, here L is a variable ligand which changes from L = CO in the first complex to L = CH_3CN in the second complex and to L = PPh_3 in the third one. The molecular structure of complex **1** obtained by X-ray single-crystal diffraction is shown in Fig. 3.33. The complex has two Mn atoms doubly bridged by 3,4,5-triphenyl-1,2-diphosphacyclopentadienyl ligands in an μ:η^1,η^1-fashion. Only two examples of such coordination mode were described earlier for 1,2,4-triphosphacyclopentadienyl ligands with nickel and copper [73, 74]. In the complexes studied here, each manganese atom has a slightly distorted octahedral environment. The geometry of the 3,4,5-

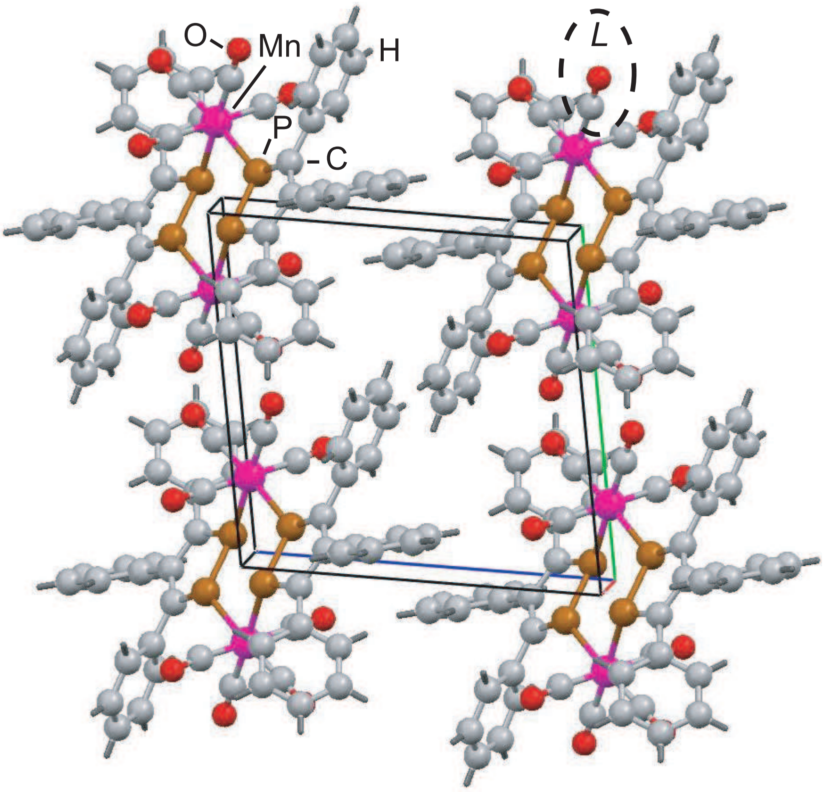

Figure 3.33: Unit cell of the Mn-dimer complex **1** obtained by X-ray single-crystal diffraction. It comprises four Mn-dimer molecules.

triphenyl-1,2-diphosphacyclopentadienide ligand in complex **1** and in sodium salt [75] is nearly the same, except for the slightly shorter P-C bonds in the case of the Mn complex. All four Mn-P bonds in complex **1** are equal in length within experimental error and the lengths amount to 2.372 Å. This result is within the range 2.34 - 2.38 Å observed for the majority of Mn(I) complexes with trivalent phosphorus ligands and is shorter than the P-Mn(II) bond, e.g., 2.430(1) Å, in manganese clusters [68].

The sum of the covalent radii of phosphorus and Mn in a low-spin state [76] is 2.46 Å while this value is significantly larger for Mn in a high-spin state (2.68 Å). The P-C bond lengths in complex **1** vary from 1.736(4) to 1.759(4) Å and are shorter than the sum of the covalent radii P-C(sp^2), i.e. 1.80 Å. The P-P bonds amount to 2.110(1) Å, which is between the P-P double bond (2.02 - 2.04 Å in coordination compounds [77–79]) and a single bond (2.259 - 2.365 Å for P-P fragments bridging two Mn atoms [80, 81]). The sums of angles at phosphorus atoms are around 340°, which is more typical for phosphorus in sp^3 hybridization. Together with the C-C intra-ring distances typical for aromatic C-C bonds, this indicates a significant delocalization of the π-electrons, though the phosphorus centers are both pyramidal. The formal oxidation state of both Mn ions calculated from the nominal charge of the ligands is +1.

3.4.2 Static Magnetic Susceptibility

The first step in the magnetic characterization of the Mn binuclear complexes comprised quasi-static DC magnetization measurements. They were performed by A. Parameswaran using the SQUID magnetometer MPMS-XL5 in a temperature range between 2 and 300 K in magnetic fields $\mu_0 H$ up to 5 T. The static magnetic susceptibility $\chi = M/H$ of the powder samples of the complexes **1**, **2** and **3** $\chi(T)$ follows closely the Curie-Weiss law $\chi = C/(T+\theta)$ in a broad temper-

Table 3.1: Fit parameters of the static magnetic susceptibility.

Sample/Ligand	C (erg G^{-2}mole^{-1}K^{-1})	θ (K)	p_{eff} (μ_B/Mn)
1/CO	0.6	1	1.55
2/CH_3CN	1.21	17	2.20
3/PPh_3	1.79	18	2.67

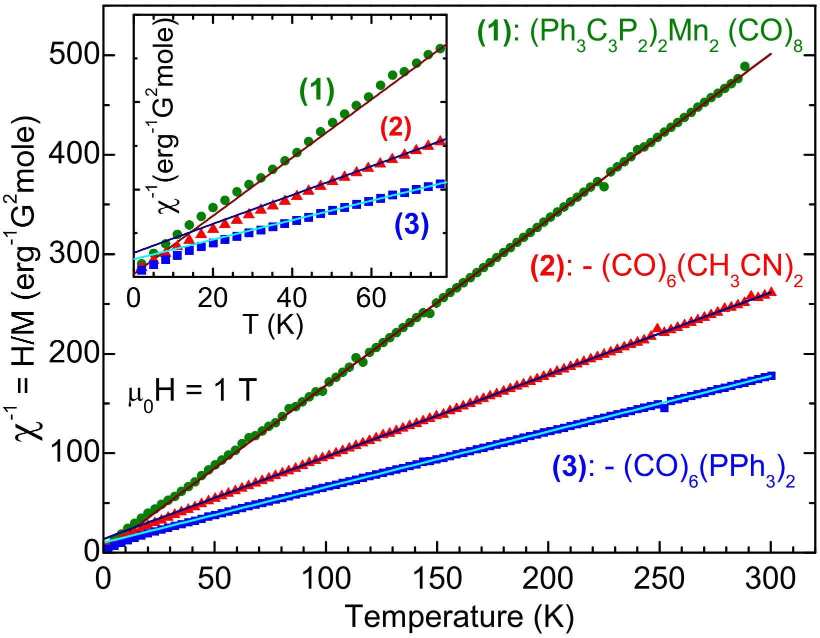

Figure 3.34: Temperature dependence of the inverse susceptibility χ^{-1} of complexes **1**, **2** and **3**. A small temperature independent contribution χ_0 arising due to the diamagnetic susceptibility of the organic ligands has been subtracted from the raw data. Inset shows the low-T region on an enlarged scale.

ature range. Here C is the Curie constant and θ is the Curie-Weiss temperature. The inverse susceptibility χ^{-1} as a function of T is plotted in Fig. 3.34 for all three complexes together. Here experimental data are shown by symbols and straight lines are fits to the Curie-Weiss law. The fits yield the values of C and θ which are summarized in Table 3.1. From the Curie constants for all three complexes the values of the effective magnetic moment p_{eff} per one Mn ion were calculated assuming the g-factor of 2 (see the ESR data below). Corresponding p_{eff} values are presented in Table 3.1 too. Obviously, the effective moment for all studied complexes is significantly smaller than that of Mn(II) in the high spin state ($S = 5/2$, $g = 2$, $p_{\text{eff}} = 5.92\,\mu_{\text{B}}$), or Mn(I) in the high spin state ($S = 2$, $g = 2$, $p_{\text{eff}} = 4.9\,\mu_{\text{B}}$) and is rather close to p_{eff} of Mn(II) in the low spin state ($S = 1/2$, $g = 2$, $p_{\text{eff}} = 1.73\,\mu_{\text{B}}$). Note that Mn(I) in the low spin state is non-magnetic. Thus from the obtained results one can assume that the oxidation state of Mn in all three complexes is close to 2+, however, p_{eff} of Mn continuously increases from complex **1** to complex **2** and further to complex **3**.

In general, the effective magnetic moment can be expressed as $p_{\text{eff}} = g[S_{\text{eff}}(S_{\text{eff}}+$

$1)]^{1/2}\mu_B$, where S_{eff} is an “effective” spin of the Mn ion. Since from the ESR data presented below the g-factor for all samples has the same value $g = 2$, the increase of p_{eff} can be phenomenologically treated as an increase of S_{eff} from 0.4 to 0.9 when going from complex **1** to complex **3** (see Table 3.1). The observed systematic changes of p_{eff} give clear evidence of its dependence on the nature of the ligand at the manganese atom. For example, complex **1**, containing such a strong π-acceptor as CO, has the lowest p_{eff}, while the largest value of p_{eff} is found for complex **3** containing a good σ-donor PPh_3. Such a tendency gives strong indications that the redistribution of the electron density in the complexes controlled by the ligand substitution affects the magnetic state of the transition metal ions. Moreover, in the case of the CO ligands (complex **1**) the obtained Curie-Weiss temperature θ amounts to 1 K, while for CH_3CN (complex **2**) and PPh_3 (complex **3**) θ increases significantly to 17 K and 18 K respectively (see Table 3.1). Therefore, the decrease of the strength of the π-acceptor and increase of the σ-donor yields an enhancement of the antiferromagnetic interactions in the complexes which is reflected in the increase of θ. Thus the susceptibility data clearly suggest that in binuclear manganese complexes **1 - 3** the metal-to-ligand charge transfer (MLCT) takes place with the formation of Mn(II) species which causes antiferromagnetic interactions observed in a broad temperature range. Due to the long distance between both manganese atoms (5.200 Å) this interaction can be realized only through the 1,2-diphosphacyclopentadienide rings.

3.4.3 Continuous Wave Electron Spin Resonance

Further important information regarding magnetic properties of the Mn binuclear complexes has been obtained by means of ESR measurements using an X-Band (9.56 GHz) Bruker EMX spectrometer. The representative ESR powder spectra (magnetic field derivative of the absorbed microwave power dP(H)/dH) for all three complexes are shown in Fig. 3.35. The spectrum of each complex consists of two separate structured ESR signals. One of the signals is situated at the magnetic field H corresponding to the g-factor value $g \approx 2.0$ and the second at about approximately the half of that field corresponding to $g \approx 4.2$. Each signal contains 6 partially resolved lines with a separation of about 80 Oe which indicate a typical for low-spin Mn(II) [82] hyperfine interaction $\mathcal{H}_{\text{HF}} = \mathbf{S} \cdot \mathbf{A} \cdot \mathbf{I}$ of the electron spin $\mathbf{S}$ with the nuclear spin $\mathbf{I}$ of Mn ($I_{\text{Mn}} = 5/2$). Note, that the $\mathbf{A}$ tensor can be substantially anisotropic [82]. In case of a powder

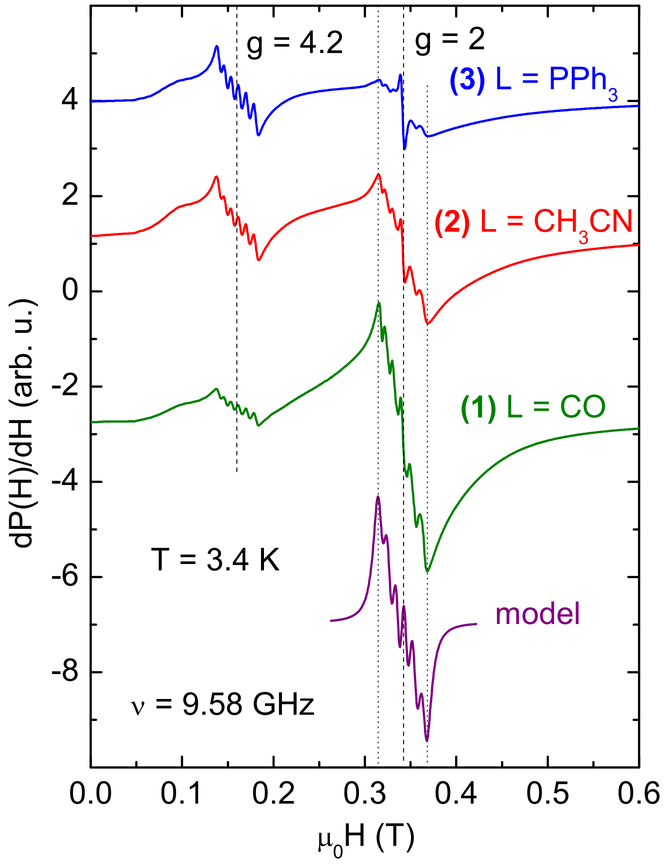

Figure 3.35: X-band ESR powder spectra of complexes **1** - **3** together with the calculated spectrum (bottom "model" spectrum) at $T = 3.4\,\mathrm{K}$.

averaged spectrum this would imply broadening and overlapping of the ESR lines, as it is observed for the studied Mn complexes. The result of a simulation of such a hyperfine split signal with the EasySpin toolbox for Matlab [18] (Fig. 3.35, bottom spectrum) agrees reasonably well with the experimental data. This simulation yields an anisotropic tensor of the hyperfine interaction $\mathbf{A}[A_x, A_y, A_z] = [280, 280, 120]\,\mathrm{MHz} = [13.4, 13.4, 5.8] \times 10^{-3}\,\mathrm{K}$.

The occurrence of the half-field signal in the ESR spectrum of the studied complexes is remarkable. An isolated low-spin ($S = 1/2$) Mn^{+2} ion in the low-symmetry ligand coordination is characterized by a nearly isotropic g-factor close to a value of 2 [83]. In this case only a single (hyperfine split) line due to the resonance transition $+1/2 \Leftrightarrow -1/2$ ($\Delta S_z = \pm 1$) within the Kramers spin doublet is expected at a "full" resonance field value $H_{\mathrm{res}} = h\nu / g\mu_{\mathrm{B}}|\Delta S_z|$. However, a more complex ESR spectrum arises if the spins S_1 and S_2 of the two Mn ions in the complex are exchange coupled in a spin dimer. The relevant spin Hamiltonian

$\mathcal{H} = J\mathbf{S}_1\mathbf{S}_2 + \mathbf{S}_1 \cdot \mathbf{D} \cdot \mathbf{S}_2 + g\mu_B(\mathbf{S}_1 + \mathbf{S}_2)\mathbf{H}$ includes the isotropic and anisotropic exchange interaction, as well as the Zeeman interaction, first, second and third terms, respectively [45].

The observed Curie-Weiss temperatures suggest an energy scale of the order of $\sim 10\,\mathrm{K}$ for the isotropic Mn-Mn magnetic interaction J (Table 3.1). Since usually $|J| \gg |D|$, the strength of the anisotropic part of the magnetic exchange is likely to be comparable with the Zeeman interaction ($\sim 0.5\,\mathrm{K}$). In this regime the otherwise "pure" spin triplet states $|S_z^{\mathrm{tot}}\rangle = |+1\rangle$, $|0\rangle$ and $|-1\rangle$ can be substantially mixed. Thus in addition to the allowed ESR transitions $\Delta S_z^{\mathrm{tot}} = \pm 1$ the formerly forbidden transitions $\Delta S_z^{\mathrm{tot}} = \pm 2$ may occur yielding an intense half-field signal with the 'doubled' effective g-factor $g_{\mathrm{eff}} = g|\Delta S_z| \approx 2g$. Interestingly, the intensity of such signals in the case of the studied Mn complexes increases concomitantly with the increase of the Mn magnetic moment upon changing the ligand (Fig. 3.35). Since the anisotropy of exchange interactions arises due to relativistic spin-orbit coupling effects, one may conjecture that tuning the electron density in the complexes by the ligand substitution enhances the orbital contribution to the magnetism of the binuclear Mn complex when passing from a strong π-acceptor in complex **1** to a σ-donor in complex **3**.

3.4.4 Electron Spin Dynamics in Mn-dimer Complexes

One of the important aspects in the potential applications of single molecular magnets in quantum computing and data storage devices is the understanding of the electron spin dynamics. A qubit, the elementary unit of a quantum computer built of the quantum spin $S = 1/2$, unavoidably experiences the longitudinal T_1 and transverse T_2 relaxation processes which are crucial for quantum information applications [84]. Since usually $T_2 < T_1$, the T_2-time which characterizes the phase coherence of the spin ensemble is of a particular importance. It should be significantly longer than the duration of coherent manipulations to prevent the irreversible leakage of information during the computation cycle [84].

The relaxation times T_1 and T_2 can be directly accessed by the pulse electron spin resonance (ESR) spectroscopy [10]. This technique has been recently used to study the spin dynamics in a number of single molecule magnets (see, e.g., [85–87]) mostly diluted in a frozen solution matrix [85, 86]. A coupling to the fluctuating nuclear spin bath as a major limiting factor for the spin decoherence in magnetic molecules has been put forward by Ardavan *et al.* [85], whereas no significant influence of the intramolecular hyperfine coupling on the electron T_2-time was found by Schlegel *et al.* [86]. The experiments by Takahashi *et al.* [87] on the molecular magnet Fe_8 in the solid phase have revealed, on the other hand, the importance of the dipolar coupling to fluctuating neighboring electron spins yielding a strong temperature dependence of T_2. All this suggests a complex interplay of different spin subsystems in magnetic molecular complexes which deserves further experimental investigation. Therefore, in the present work the electron spin dynamics in the above described binuclear Mn complexes was studied in order to better understand the relaxation mechanisms in molecular magnetic complexes.

Pulse ESR measurements were performed at X-band frequencies by means of an Elexsys E-580 spectrometer (Bruker) in the Zavoisky Physical-Technical Institute, Kazan. Spin decoherence T_2 and longitudinal relaxation T_1 times were measured as described in section 2.2. The measurements at two different temperatures of 6 K and 80 K were performed at the center field of the partially resolved hyperfine-split CW ESR signal (ref. to section 3.4.3). The complexes **1** - **3** were studied as microcrystalline powders and as homogeneously dissolved in tetrahydrofurane (THF). In the latter case, 10 mg ($\sim$ 0.01 mmol) of complex **1** were dissolved in 10 ml THF at room temperature. The samples of complexes **2** and **3** were obtained similarly by dissolution of 11 mg of **2** or 15 mg of **3** in 10 ml THF. The low concentrations of the solutions ($\sim 10^{-3}$ M) allow to eliminate any intermolecular interactions between the molecules of the complexes. Note, that all the measurements were performed at temperatures below the melting point of the solvent ($T_{\mathrm{melt.}} = 165$ K) and, therefore, one should keep in mind that the samples were studied as *frozen solutions*.

Results and Discussion

As seen in Fig. 3.36, neither at low (6 K) nor at high (80 K) temperatures the dependence of the electron spin echo intensity on the delay time τ in powder samples cannot be described by a single exponential decay function $V(2\tau) = V_0 \exp(-2\tau/T_2)$. In particular, in the low temperature regime the echo decays can be reasonably well described by the stretched exponential function

$$V(2\tau) = V_0 \exp\left[-(2\tau/T_2^*)^b\right], \tag{3.7}$$

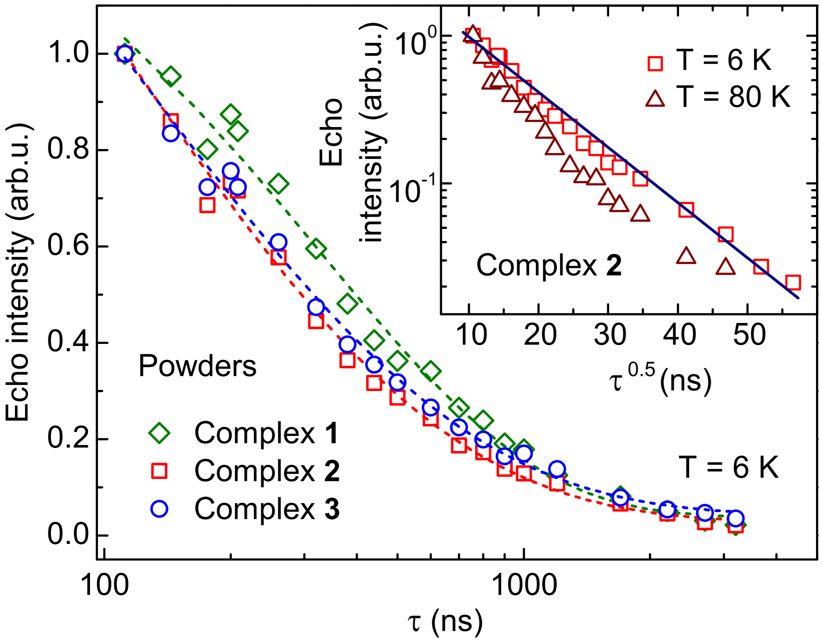

Figure 3.36: The intensity of the primary electron spin echo $V(\tau)$ vs. the delay time τ measured on the powder samples at $T = 6\,\mathrm{K}$, symbols, and fits by the non-exponential decay function, lines (see the text). The presentation of $V(\tau)$ on the log-scale vs. $\sqrt{\tau}$ for complex **2** at 6 K and 80 K is shown in the inset.

as shown in the inset in Fig. 3.36, whereas at high temperature the agreement becomes somewhat worse rendering the values of T_2^* and b less certain. Here b is the exponent stretching factor and T_2^* is the effective spin decoherence time. The respective values of b and T_2^* for all three complexes are summarized in Table 3.2.

Table 3.2: Spin decoherence times T_2 and T_2^* for complexes **1** - **3** in the solid phase and dissolved in a frozen solution matrix.

Complex / Ligand	Sample type		$T = 80\,\mathrm{K}$	$T = 6\,\mathrm{K}$
1 / CO **2** / CH_3CN **3** / PPh_3	Powder	T_2^* (μs) / b	~ 0.08 / ~ 0.5	0.65 / 0.8 0.18 / 0.5 0.20 / 0.5
1 / CO **2** / CH_3CN **3** / PPh_3	Solution	T_2 (μs)	~ 0.1	4.0 3.3 3.2

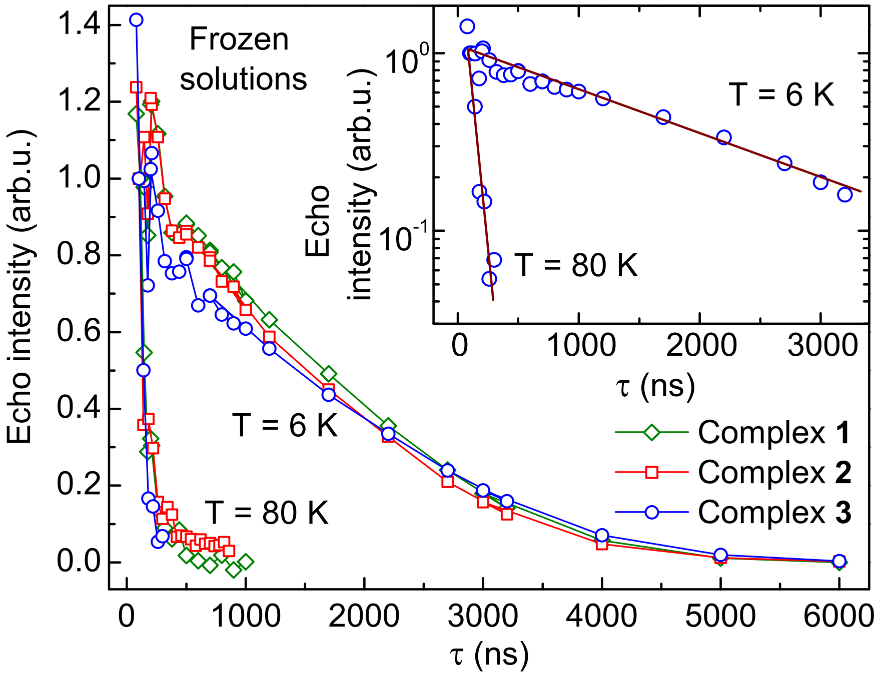

Figure 3.37: The intensity of the primary electron spin echo vs. the time delay τ observed in the frozen solutions of the complexes **1** - **3** at $T = 6\,\mathrm{K}$ and $80\,\mathrm{K}$. Inset: The presentation on the log-scale visualizes a single characteristic decay time T_2.

In frozen solutions, in contrast to powders, the time evolution of the electron spin echo intensity follows a single exponential decay law (Fig. 3.37), which corresponds to $b = 1$ and $T_2^* = T_2$ in Eq. (3.7). The obtained values of T_2 are given in Table 3.2.

A separation of spin decoherence and longitudinal relaxation processes ($T_2 < T_1$) has been checked by the low temperature measurements of T_1. The results reveal a very similar relaxation time $T_1 \approx 10\,\mu\mathrm{s}$ for all complexes in the powder form. In the frozen solutions the longitudinal relaxation times are significantly longer and amount to $140\,\mu\mathrm{s}$, $90\,\mu\mathrm{s}$ and $80\,\mu\mathrm{s}$ for complexes **1**, **2** and **3**, respectively.

All primary echo experiments on powders and frozen solutions revealed a modulation of the spin echo intensity known as the Electron Spin Echo Envelope Modulation (ESEEM) [88, 89]. This modulation is clearly seen in all T_2 measurements at time delays $\tau < 700\,\mathrm{ns}$. Examples of the ESEEM for complex **1** at $T = 6\,\mathrm{K}$ are shown in Fig. 3.38. The origin of the ESEEM is the interaction of electron spins with surrounding magnetic nuclei with a non-zero spin. The modulation arises

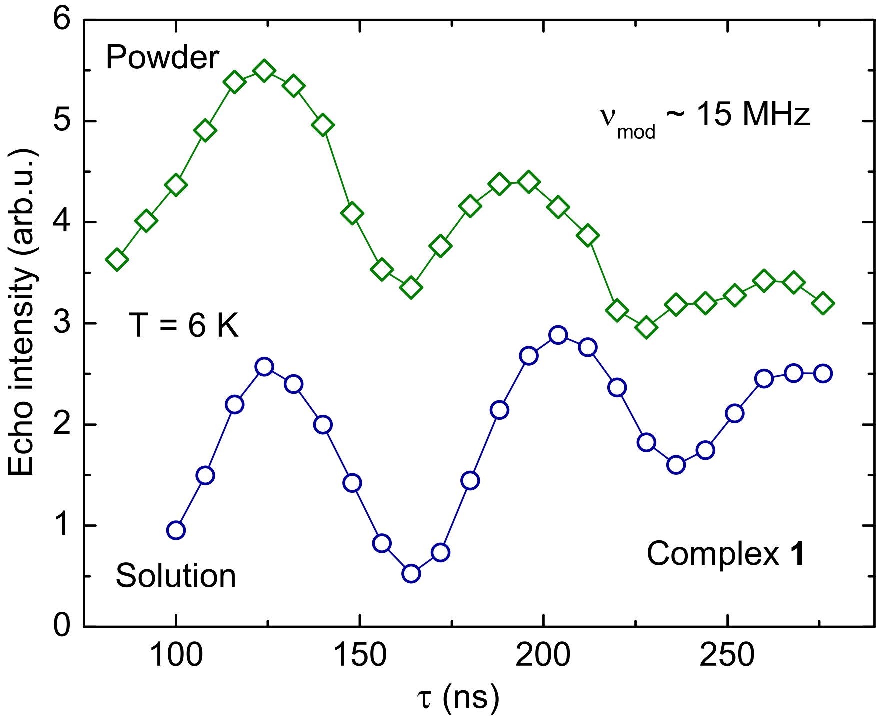

Figure 3.38: The electron spin echo envelope modulation (ESEEM) observed on complex **1** in the powder form and in a frozen solution at $T = 6\,\mathrm{K}$ using the primary echo sequence. The period of the modulation corresponds to the proton Larmor frequency $\omega_{^1\mathrm{H}}$. (see the text).

as the effect of interference between pairs of excited ESR transitions between electron-nuclear levels [89, 90]. The period of the modulation yields the Larmor frequency ν_N of the nuclear spins involved. For all studied samples it amounts to $\sim 15\,\mathrm{MHz}$ which is equivalent to the frequency ν_H of the proton spins at the field value corresponding to the resonance field of the electron spins. This observation gives evidence that the modulation is caused by hyperfine interactions of the Mn electron spin with the nearby protons. We note here, that the ESEEM due to the on-site hyperfine interaction of the electron spin with the nuclear spin of Mn is not experimentally detectable owing to a strong on-site hyperfine coupling.

There is a number of mechanisms which can contribute to the electron spin relaxation processes in the studied Mn-dimer complexes, such as spin-phonon relaxation, spin-spin interactions between Mn ions, hyperfine interactions with the nuclear moments, spin- and spectral diffusion, etc. [91]).

The dipole-dipole interaction with the nearby proton spins is considered to be the main decoherence mechanism in the metal-organic molecular complexes

[85–87]. In our case a coupling between the electron spins and the proton subsystem is evident from the ESEEM experiment (Fig. 3.38). An order of magnitude estimate of this contribution to T_2 in the studied complexes can be made with a simple model that treats a system with an electron spin surrounded by homogeneously distributed nuclear moments [10]. Taking the concentration of nuclear spins equal to the average concentration of the hydrogen atoms in a single crystal of complex **1**, the estimated T_2 relaxation time for the Mn spin is of the order $\sim 5\,\mu$s. This value is rather close to the experimentally obtained values of T_2 in frozen solutions at $T = 6$ K (Table 3.2) suggesting that the proton-mediated mechanism is the dominant relaxation channel for Mn spins. This is in fact not surprising since the intermolecular Mn-Mn interaction is unlikely in this case owing to a big spatial separation between the Mn-complexes in the frozen solution. The spin-spin interaction of the isolated pair of the Mn ions inside the complex should contribute to the structure of the spectrum rather than to the paramagnetic relaxation. It is hence supposed that the intradimer interaction can manifests itself in the relaxation only indirectly, e.g., as a source for a modulation of the spin-spin interaction between dimers in the solid phase. The strong reduction of T_2 at high temperature (Table 3.2) is likely to be associated with increased molecular motion owing to a softening of the glassy-like frozen solution by approaching T_{melt}, as has been discussed before, e.g., in Refs. [92, 93].

In the powder samples, in addition to the coupling to the subsystem of protons, there are obviously further significant dephasing mechanisms which shorten the decoherence time of the Mn spins. Here, compared to frozen solutions, the decay of the electron spin echo signal at 6 K is by an order of magnitude faster and is not exponential (Fig. 3.36). Such a drastic difference suggests that spin-spin exchange and dipole-dipole interactions between the Mn spins give substantial contributions to the phase relaxation in the solid phase. The stretched exponential shape of the spin echo decay (Eq. (3.7)) may arise due to several reasons. Since typically the amplitude of the microwave pulse corresponds to the spectral width of a few Gauss, not all spins contributing to an inhomogeneously broadened ESR line can be excited. This is also the case in the studied complexes where the central line of the ESR spectrum is 50 - 70 G broad (ref. to section 3.4.3). Hence the cross-relaxation between the excited spins which contribute to the spin echo signal and the non-excited fraction of spins can take place by mutual spin flip-flops [91, 94]. Such spin excitation transfer reduces the number of spins contributing to the echo signal and results in its additional decay. Other mechanisms, such as spin and spectral diffusion might be also responsible for the observed kinetics of the phase relaxation [91]. The spin excitation transfer may lead to a spatial diffusion of the spin coherence (spin diffusion) which by reaching, e.g., the surface of the powder particles may yield a fast phase relaxation. Furthermore, the modulation of local fields due to flip-flop processes may cause migration of the frequency of the excited spins (spectral diffusion) which can also contribute to the spin decoherence. Which of the above discussed diffusion mechanisms is dominating in the studied samples remains to be elucidated. However, the fact that the echo decay turns to a single exponential form upon dissolving the complexes in a solution suggests that intermolecular spin-spin interactions between the Mn ions are responsible for additional decoherence in powders.

Notably the values of the effective spin decoherence time T_2^* and of the exponent stretching factor b in complexes **2** and **3** are appreciably reduced compared to complex **1** (Table 3.2). This is in an apparent correlation with the increased values of the Mn magnetic moment in complexes **2** and **3** ($p_{\text{eff}} = 2.20\,\mu_{\text{B}}$ and $2.67\,\mu_{\text{B}}$, respectively) with respect to complex **1** where by an appropriate ligand substitution the p_{eff} has been substantially reduced down to $1.55\,\mu_{\text{B}}$ (see section 3.4.2). This correlation further supports the conjecture that the electron spin decoherence in the studied molecular complexes in the solid phase is driven by intermolecular spin-spin interactions at least at low temperatures. At elevated temperatures the intermolecular magnetic coupling may become less relevant and other mechanisms of the phase relaxation like contributions from spin-lattice relaxation processes, spin diffusion, molecular dynamics may become important. Possibly because of this, the spin echo decays, though remaining non-exponential, show deviations from the stretched exponential behavior, Eq. (3.7) (Fig. 3.36).

3.4.5 Conclusion

Static magnetic measurements give clear evidence of the magnetic state of the Mn ions in the three studied complexes. However, the observed effective magnetic moment is substantially smaller than expected for high spin Mn(I). This finding suggests a remarkable difference between the formal and actual oxidation states of the Mn ions in these complexes. The systematic changes in the effective magnetic moment and the shape of the ESR spectra give clear evidence that the redistribution of the electron density in the molecule caused by the ligand substitution affects the magnetic state of the transition metal ions.

In addition, the time and temperature evolution of the electron spin echo signals in the Mn-dimer complexes were studied. The decoherence of the electron spin ensemble is influenced by a number of factors. One factor which was also commonly discussed before is the hyperfine coupling of electron spins to the surrounding proton moments. Furthermore, there are strong experimental indications that in the solid phase additional decoherence arises due to intermolecular spin-spin interactions. This leads to a non-exponential decay of the electron spin echo. The occurrence of such multichannel relaxation paths might be of a generic character for molecular magnets in the solid phase and thus should be taken into account, e.g., regarding possible applications of molecular magnets in quantum computation technologies.

4 Summary (Part I)

In this work, the magnetic properties of several metal-organic molecular complexes were studied. Magnetization measurements in static magnetic fields up to 15 T or pulsed magnetic fields up to 60 T allowed to determine the ground states of the studied complexes. The temperature dependence of the static magnetization provided information about the intramolecular magnetic exchange interactions between the metal ions. High-field ESR measurements at frequencies up to 650 GHz in magnetic fields up to 15 T were performed in order to determine the g-factors and the magnetic anisotropy of the complexes. The analysis of the magnetization and ESR results was carried out using the effective spin Hamiltonian and enabled determination of all relevant parameters. In addition, some of the complexes were investigated by the pulse ESR technique giving information about the electron spin dynamics and, in particular, spin coherence in the studied molecular clusters.

The first two studied complexes were the Ni(II)-based dimer and trimer. They have a different arrangement of the Ni ions in the cores, which significantly influences the magnetic properties of the complexes. For the Ni_2-complex, the magnetization measurements yield a ferromagnetic coupling of 42 K between the Ni ions and a ground state with total spin $S = 2$. In the case of the Ni_3-complex the measurements show a rather strong antiferromagnetic coupling of 140 K which leads to a $S = 1$ ground state. ESR measurements revealed different signs for the magnetic anisotropy of these complexes. The Ni_2-complex has a negative axial anisotropy ($D = -1.1\,\mathrm{K}$) and therefore a bistable magnetic ground state with an “easy” magnetic axis. For the Ni_3-complex, the analysis of the ESR spectra yields a positive axial anisotropy ($D = 2.9\,\mathrm{K}$) and an “easy plane” situation for the molecule. Thus, the variation of the ligand structure has a very strong impact on the magnetic properties of the studied complexes, which opens the possibility for the synthesis of molecular magnetic complexes with predetermined magnetic properties.

The magnetization measurements performed on the heterometallic Mn_2Ni_3-complex show ferromagnetic intramolecular couplings of 44 K and 19 K between Mn-Ni and Ni-Ni ions, respectively, and a high-spin ground state for the molecule with total spin $S_{\text{tot}} = 7$. From the ESR measurements, a magnetic anisotropy parameter $D = -0.55\,\text{K}$ was determined corresponding to an energy barrier of 27 K for the thermal relaxation of the magnetization. Such a relatively large anisotropy barrier leads to the hysteretic behavior of the magnetization at $T < 1.5\,\text{K}$, as was shown by low-temperature single crystal magnetization and AC susceptibility measurements. Moreover, well pronounced quantum tunnelling steps in the hysteresis curve of the magnetization were observed which confirm the single molecular magnet behavior of the Mn_2Ni_3-complex.

The studied Mn(III)-*meta*-chain (with the *meta*-position of the fluorine ion at the phenyl ring) possesses a pronounced hysteretic behavior of the magnetization below $T_{\text{block}} \approx 3\,\text{K}$ which is a clear property of a single chain magnet. The observed blocking temperature differs significantly from that obtained for the Mn(III)-*ortho*-chain ($T^{ortho}_{\text{block}} \approx 4.5\,\text{K}$ [61]), thus indicating an influence of the fluorine ion position on the magnetic anisotropy in the Mn(III)-chains. The saturation magnetization was reached only in 60 T pulsed-field measurements. The observed value corresponds to the effective spin $S_{\text{eff}} = 1.83$ which is slightly larger than the expected $S = 3/2$ for the chain. The ESR measurements yield a g-factor of 1.8 and an axial magnetic anisotropy with an anisotropy gap $\Delta = 17\,\text{K}$ which is in agreement with the observed hysteretic behavior of the magnetization.

The last studied group of molecular complexes was Mn(I)-dimer clusters. Here, the magnetization measurements give clear evidence of the magnetic state of Mn ions. However, the observed effective moment is substantially smaller than that expected for the high spin Mn(I) for all tree complexes. The observed systematic changes in the effective magnetic moment from one complex to another give clear evidence that the ligand substitution affects the magnetic state of the transition metal ions. Pulse ESR measurements revealed several mechanisms of the electron spin decoherence in the studied complexes. Mainly the relaxation is caused by the hyperfine interactions of the Mn electron spins with the nearby proton moments. However, there are experimental indications that in the solid phase at low temperatures additional decoherence arises due to the intermolecular interaction between Mn spins. Furthermore, the characteristic relaxation times significantly and systematically change while going from one complex to another which is in agreement with the changes in the effective magnetic moment of the Mn ions.

This suggests a possibility to control the static and dynamic magnetic properties of the complexes by the ligand substitution.

Part II

Feasibility of Nanoscaled Magnets for Hyperthermia Cancer Treatment

5 Magnetic Hyperthermia

The heating of tumor tissue using magnetic nanoparticles has great potential as a new treatment approach for cancer therapy. Local heating by means of nanosized probes not only directly affect the cancer cells but also increases the efficiency of concomitant radio- or chemotherapy. Nowadays, the majority of the research in this field is focused on magnetic iron oxide nanoparticles [95] which have proven their feasibility in animal experiments [96, 97] and are now under clinical trials [98]. However, metallic iron would offer advantages over its oxides due to the higher saturation magnetization which implies higher energy losses in alternating magnetic fields. In practice, the use of nanoparticles made of iron is hindered because of oxidation in a biological environment. A possible solution for this problem is the use of iron filled carbon nanotubes (Fe-CNT), where a carbon shell efficiently protects the encapsulated iron from the biological environment while its magnetic properties are retained [99, 100]. Further, the carbon shells prevent cytotoxic effects caused by oxidation processes. Recent toxicity studies of Fe-CNT on cells indicated no significant toxicity of Fe-CNT [101]. Moreover, carbon shells may act as multi-functional containers which can be filled with different materials. Additional filing materials such as a nanothermometer would increase the potential of CNT as hyperthermia agents. Attaching functional elements to the outer shell of CNT might increase their biocompatibility or enable loading anticancer agents. This part of the thesis will concentrate on magnetic properties of differently filled CNT and their potential applications in magnetic hyperthermia. The main goal of this investigation was to test the feasibility of magnetically filled CNT for contactless magnetic heating and to understand their heating mechanisms. In this respect, their magnetic properties in static DC and alternating AC magnetic fields will be described and discussed. Moreover, two initial studies of possible hyperthermia applications of magnetic nanoparticles will be presented, such as a combination of hyperthermia and chemotherapy and a spatial localization of the hyperthermia effect via applying DC magnetic fields.

5.1 Heating mechanisms

There are several possible mechanisms for heating of magnetic particles in alternating (AC) magnetic fields: ferromagnetic (hysteresis) losses, superparamagnetic (relaxation) losses, eddy currents, etc [2, 3, 102, 103]. Ferromagnetic particles possess hysteretic properties in a time varying magnetic field. The hysteresis losses caused by repeated switching of the magnetization of the magnetic particles would lead to very efficient heating. The amount of dissipated energy in this case is given by the frequency ν multiplied by the area of the magnetic hysteresis loop:

$$P = -\mu_0 \nu \oint H \mathrm{d}M \,. \tag{5.1}$$

However, to produce heat in a single domain ferromagnetic nanoparticle the magnetic moment has to be switched by a magnetic field above the switching field, therefore no minor loops can be used for heating. For realistic materials, this can lead to rather high required AC magnetic field strengths, which is not always suitable for medical applications.

An alternative mechanism for magnetically induced heating is associated to superparamagnetic or relaxation losses. The term superparamagnetism was introduced by Elmore in 1938 [104] to describe the magnetic behavior of colloidal systems containing iron oxide particles. When such a colloidal system is removed from a magnetic field, its magnetization relaxes back to zero due to thermal fluctuations. For small magnetic field amplitudes, and assuming minimal interaction between magnetic nanoparticles, the response of the magnetization to an AC field can be described in terms of the complex susceptibility $\chi = \chi' + i\chi''$. Then with a magnetic field of the form

$$H(t) = H_0 \cos\omega t = Re[H_0\, e^{i\omega t}] \,, \tag{5.2}$$

where $\omega = 2\pi\nu$, the resulting magnetization is

$$M(t) = Re[\chi\, H_0\, e^{i\omega t}] = H_0(\chi' \cos\omega t - \chi'' \sin\omega t) \,, \tag{5.3}$$

where it seen that χ' is the in-phase component, and χ'' is the out-of-phase component of the susceptibility. Substituting for M and H in Eq. (5.1) from Eq. (5.2) and (5.3) leads to

$$P_{\mathrm{SPM}} = -\mu_0 \pi \chi'' \nu H^2 \,. \tag{5.4}$$

Eq. (5.4) implies a positive conversion of magnetic energy into internal energy if M lags H [105]. The relaxation of the magnetization in superparamagnetic systems can be connected with either the physical rotation of the particle (Brownian relaxation), or the rotation of the magnetic moment within each particle (Néel relaxation). The Brownian relaxation time τ_{Br} depends on the viscosity η of the liquid dispersion medium and the hydrodynamic volume V_{h} of the particle, and can be described by the relation:

$$\tau_{\mathrm{Br}} = \frac{3\eta V_{\mathrm{h}}}{k_{\mathrm{B}}T} . \tag{5.5}$$

The Néel relaxation time τ_{N} is correlated with the material properties of the particles by the effective anisotropy constant K_{eff} and with the magnetic volume V of the particle:

$$\tau_{\mathrm{N}} = \tau_0 \exp\left[\frac{\mathrm{K_{eff}V}}{\mathrm{k_BT}}\right] . \tag{5.6}$$

In these equations, k_{B} is the Boltzmann constant, T is the absolute temperature and τ_0 is a time constant. For iron oxide nanoparticles τ_0 has the order of magnitude $10^{-9}\,\mathrm{s}$. In a typical superparamagnetic ferrofluid the Brownian and Néel relaxations processes take place in parallel and therefore the effective relaxation time can be given by

$$\frac{1}{\tau} = \frac{1}{\tau_{\mathrm{Br}}} + \frac{1}{\tau_{\mathrm{N}}} . \tag{5.7}$$

The magnetic relaxation involves dissipative processes which can be distinguished by the frequency dependence of the imaginary part χ'' of the complex-magnetic susceptibility. From Debye theory [106], it is known that the relaxation time τ is correlated with the angular frequency ω at which χ'' has a maximum, by the relation: $\omega\tau = 1$. In the case of iron oxide nanoparticle dispersions, such maxima were observed at the frequencies of $1 - 10\,\mathrm{kHz}$ assigned to the Brownian-type relaxation [103, 105, 107] and frequencies of $20 - 40\,\mathrm{MHz}$, assigned to the Néel-type relaxation [108–110]. In the case of pure Néel relaxation, for example, if magnetic nanoparticles are bonded to a solid medium, the measurements of the magnetic response have two temperature regimes - above and below the so called blocking temperature T_{B}. The relaxation of the magnetization of a single particle with K_{eff} is characterized by the Néel relaxation time τ_{N} given by Eq. (5.6). If the relaxation time is short enough and the particle can achieve the thermal equilibrium in the time of measurement, the particle is in the superparamagnetic state (above T_{B}), if not it is in the so called blocked state (below T_{B}). Since different types of experiments have different time windows over which the magnetic response is detected, the blocking temperature of the magnetic particles directly depends on the measurement method i.e. frequency. For example, in a DC magnetization measurement, where the measurement time is about 100 - 500 sec, in small magnetic fields $T_{\mathrm{B,DC}}$ can be estimated using the Eq. (5.8) [103].

$$T_{\mathrm{B,DC}} \approx \frac{K_{\mathrm{eff}} V}{30 k_{\mathrm{B}}} \tag{5.8}$$

Experimentally $T_{\mathrm{B,DC}}$ can be determined by means of field cooled (FC) and zero field cooled (ZFC) temperature dependent DC magnetization measurements.

Note, that in general, eddy currents might cause energy losses in AC magnetic fields too. However, magnetic particles used for the hyperthermia are too small and AC field frequencies are too low for the generation of any substantial eddy currents [2, 105], which was proven experimentally in this work using non-magnetic metal nanoparticles (see section 7.1). Another possible effect of eddy currents in a potential medical application is direct heating of human tissue. This effect is not localized precisely at a certain target position but causes non-specific inductive heating. Therefore, it is important to minimize the eddy currents on human tissue which implies limitations of the magnetic field strength and the frequency $\nu H \leq 4 \cdot 10^8\,\mathrm{Am^{-1}s^{-1}}$ which can be safely applied in hyperthermia treatment [2, 3].

6 Experimental

6.1 Materials

Iron containing multiwalled carbon nanotubes (Fe-MWCNT) have been synthesized by the aerosol-assisted chemical-vapor deposition (CVD) technique [111, 112], which is based on a liquid starting material consisting of a metal-organic catalyst compound (ferrocene) solved in hydrocarbon (cyclohexane or acetonitrile). The transmission electron microscopy (TEM) image of the Fe-MWCNT (pristine MWCNT) is shown in Fig. 6.1(left). The obtained material is a composite of diamagnetic multi-walled CNT and Fe-particles which are used as catalyst during the synthesis. There is always at least one Fe particle for each MWCNT and the diameters of the MWCNT are determined by the size of the catalyst particles. After the synthesis, the MWCNT have outer diameters between 10 and 40 nm while the inner diameters as well as the size of the Fe-particles range between 5 and 20 nm. Most of the Fe-particles look like drops with a smaller and a larger side. The length of the CNT is around 20 μm. In order to have a non-magnetic control material, Fe-MWCNT were annealed at 2500 °C under an argon atmosphere. Detailed magnetic studies of the purified MWCNT show a clear diamagnetic behavior [113]. Other control materials are MWCNT filled with non-magnetic CuI (CuI-MWCNT) and carbon wrapped Cu nanowires. CuI-MWCNT have been produced by the post-synthesis filling method. This technique includes the synthesis of empty MWCNT, opening of their ends and filling with CuI [114]. Carbon coated Cu nanowires have been produced by thermal decomposition of Copper(II)-acetylacetonate in a closed, evacuated quartz ampule as described in Ref. [115]. In order to increase the amount of the magnetic material, additionally filled MWCNT have been synthesized. Iron filled carbon nanotubes (Fe-filled MWCNT) are prepared by means of thermal-catalytic CVD with ferrocene as a precursor. The TEM image of the Fe-filled MWCNT is shown in Fig. 6.1(right). The iron filling forms single crystal nanowires up to 20 μm long and with diameters determined by the inner diameter of the MWCNT. Besides

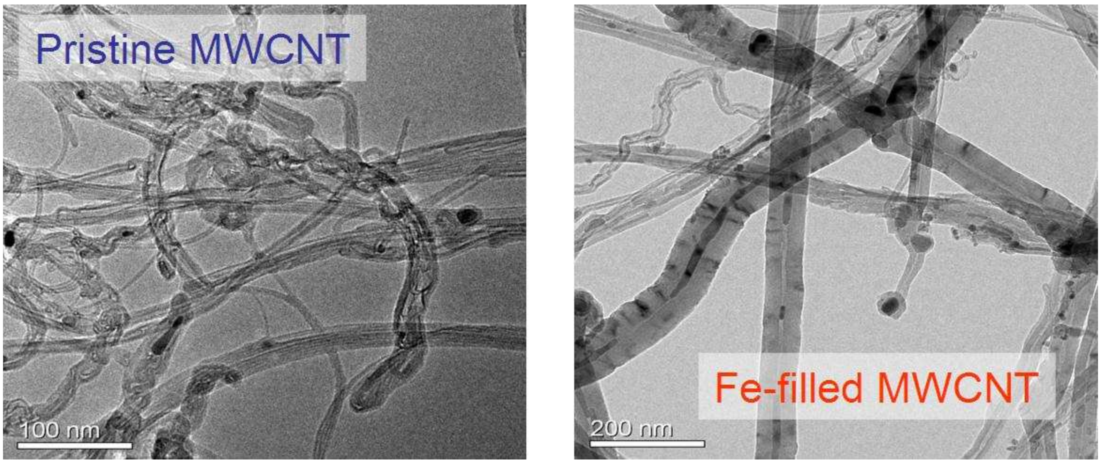

Figure 6.1: Transmission electron microscopy (TEM) image of iron-containing MWCNT. Left: pristine MWCNT (Fe-MWCNT); right: Fe-filled MWCNT.

iron nanowires, however, Fe-filled MWCNT contain Fe-catalyst particles used during the synthesis. The shape and size of catalyst particles is similar to the unfilled MWCNT [116].

Another studied material are cobalt filled carbon nanofibers synthesized as described in Ref. [117]. In this case Co nanoparticles are encapsulated in so-called carbon nanofibres, i.e. carbon shells of different shape (see Fig 6.2). The Co particles have spherical or oblong shape with the average diameter 10 - 15 nm.

6.2 Methods

Static magnetic properties of the studied materials were investigated by means of a commercial Quantum Design MPMS (Magnetic Property Measurement System) SQUID (Superconducting Quantum Interference Device) magnetometer and a MicroMag Model 2900 (Princeton Measurement Corp.) AGM (Alternating Gradient Magnetometer). The magnetic field dependence of the static (DC) magnetization $M(H)$ was measured at room temperature in magnetic fields H up to 10 kOe. Temperature dependence of the magnetization $M(T)$ was measured in a magnetic field of 10 Oe for zero-field-cooled (ZFC) and field-cooled (FC) conditions. In the case of ZFC magnetization measurements, the sample was firstly heated from room temperature up to 400 K and then cooled down to 5 K in zero magnetic field. Then, after applying the magnetic field ($H = 10$ Oe), the magnetization

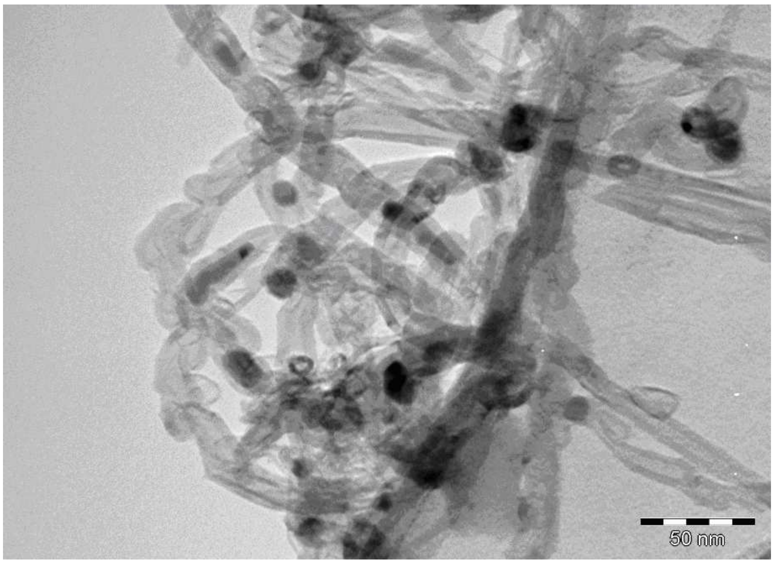

Figure 6.2: TEM image of the Co-filled nanofibers [117].

measurements were performed upon warming. For FC magnetization measurements, the sample was cooled in the same magnetic field ($H = 10\,\mathrm{Oe}$) down to 5 K and the magnetization was measured in the warming cycle up to 400 K under applied magnetic field. AC susceptibility measurements were performed at room temperature ($T = 300\,\mathrm{K}$) in a commercial Quantum Design PPMS (Physical Property Measurement System), using the ACMS (AC Measurement System) option, for frequencies $\nu = 33 - 9333\,\mathrm{Hz}$ and a magnetic field strength $H = 10\,\mathrm{Oe}$.

In order to study the heating ability of the studied materials in alternating magnetic fields, the following experimental setup has been built. As illustrated in Fig. 6.3, it consists of a high-frequency generator (Hüttinger TIG 10 kW) with an impedance matching network and a water-cooled magnetic coil system. The coil contains 5 turns; the height of the coil is 40 mm and the diameter of the inside bore is 30 mm. For such a coil geometry, the setup provides alternating magnetic fields with frequencies $\nu = 100$ - $230\,\mathrm{kHz}$ and magnetic field strengths H up to 120 kA/m (1500 Oe). The temperature change per time unit was determined using a fiber-optic temperature controller (Luxtron One), which is suitable for measurements in high-frequency magnetic fields. Since the goal of these experiments was to estimate the amount of heat produced by the magnetic nanoparticles all the temperature measurements were performed in "quasi-adiabatic" conditions. For this purpose the sample was placed in an evacuated glass dewar vessel situated

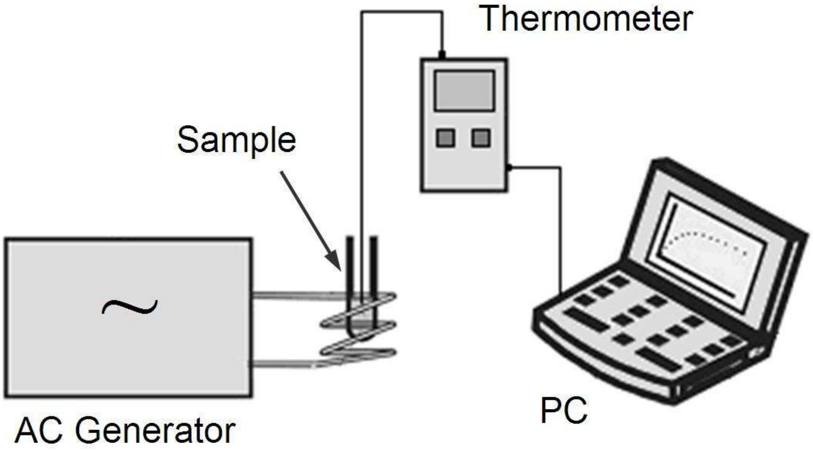

Figure 6.3: Experimental setup for in-vitro AC heating and temperature measurements.

inside the coil which provides reasonably good temperature insulation of the sample space. The measurements were performed on dispersions of the studied nanoparticles in aqueous solutions. In order to obtain a stable dispersion the dry materials were mixed 1:1 weight ratio with human albumin and dispersed in phosphate buffered saline (PBS) using ultrasonication. The concentration of the obtained dispersion C was of $5\,\mathrm{mg/ml}$.

7 Results and Discussions

7.1 Iron containing carbon nanotubes

The initial studies aiming to test the feasibility of magnetically functionalized CNT for the contactless magnetic heating have been done on multiwalled carbon nanotubes containing iron catalyst particles (Fe-MWCNT). In this section static and dynamic magnetic properties of Fe-MWCNT will be described and discussed.

Magnetic properties of Fe-MWCNT

Magnetic properties of iron nanoparticles encapsulated by MWCNT were studied on Fe-MWCNT powders and Fe-MWCNT dispersions by means of MPMS SQUID magnetometer and PPMS (see section 6.2). Static DC magnetization measurements on the Fe-MWCNT powder reveal pronounced ferromagnetic behavior of the material typical for α-Fe. The hysteresis loop of the Fe-MWCNT at room temperature ($T = 300\,\mathrm{K}$), presented in Fig. 7.1, yields a coercivity H_C of 200 Oe and a saturation magnetization M_S of $8.2\,\mathrm{erg\,G^{-1}g^{-1}_{Fe-MWCNT}}$. The coercivity $H_\mathrm{C} = 200\,\mathrm{Oe}$ gives a rough idea about the average switching field of the magnetic nanoparticles, whereas, the saturation magnetization indicates the amount of the magnetic material in the MWCNT. By comparing M_S with the saturation magnetization of bulk α-Fe $M_\mathrm{bulk} = 217\,\mathrm{erg\,G^{-1}g^{-1}}$, the mass ratio of iron in Fe-MWCNT can be estimated to $0.038\,\mathrm{g_{Fe}/g_{CNT}}$. Note that energy dispersive X-ray spectroscopy (EDX) shows an iron concentration in Fe-MWCNT of around 3 ± 1 weight %. This result agrees to the magnetization analysis which however yields the content of ferromagnetic material with a much higher precision than EDX [118]. The temperature dependence of the FC and ZFC magnetization of the Fe-MWCNT powder is presented as an inset in Fig. 7.1. These data reveal a pronounced ferromagnetic behavior of the Fe-MWCNT powder at T up to 400 K, indicating the average blocking temperature T_B^av of the iron nanoparticles above

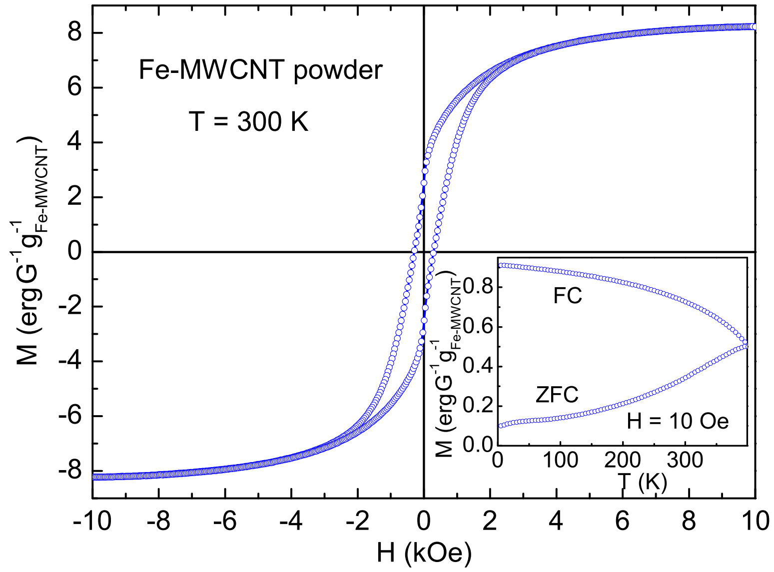

Figure 7.1: Hysteresis loop $M(H)$ of Fe-MWCNT powder at room temperature. Inset: FC and ZFC temperature dependence of the magnetization $M(T)$ for the Fe-MWCNT powder.

400 K. This implies that most of the nanoparticles are blocked at all temperatures (36 - 50 ° C or 309 - 323 K) used in medical hyperthermia. Quantitatively, T_B in DC magnetic measurements can be described by Eq. (5.8) (ref. to section 5.1). For almost spherical catalyst particles the effective magnetic anisotropy K_eff is mostly determined by the magnetocrystalline anisotropy ($K_\mathrm{iron} = 48\,\mathrm{kJ/m^3}$). Thus, according to Eq. (5.8), $T_\mathrm{B}^\mathrm{av} > 400\,\mathrm{K}$ yields a mean particles diameter $D^\mathrm{av} > 18.8\,\mathrm{nm}$. However, the shape of the ZFC curve indicates a presence of magnetic particles with $T_\mathrm{B} < 300\,\mathrm{K}$ ($D < 17.0\,\mathrm{nm}$). This implies that there is a small part of the magnetic particles which are not blocked at the hyperthermia temperatures (in DC measurement conditions).

Magnetic properties of Fe-MWCNT dispersion were studied under two different conditions. Initially the magnetic field dependence of the magnetization $M(H)$ was measured on a liquid dispersion at room temperature ($T = 300\,\mathrm{K}$) and then the same dispersion was frozen at $T = 260\,\mathrm{K}$ and the measurement was repeated. The $M(H)$ curves of both liquid and frozen dispersions are presented in Fig. 7.2. Fe-MWCNT in liquid dispersion show no visible hysteresis and behave like a superparamagnetic system. However, after the freezing the same dispersion shows a magnetic hysteresis similar to the powder. This observation gives evidence that the observed superparamagnetic behavior of Fe-MWCNT in liquid

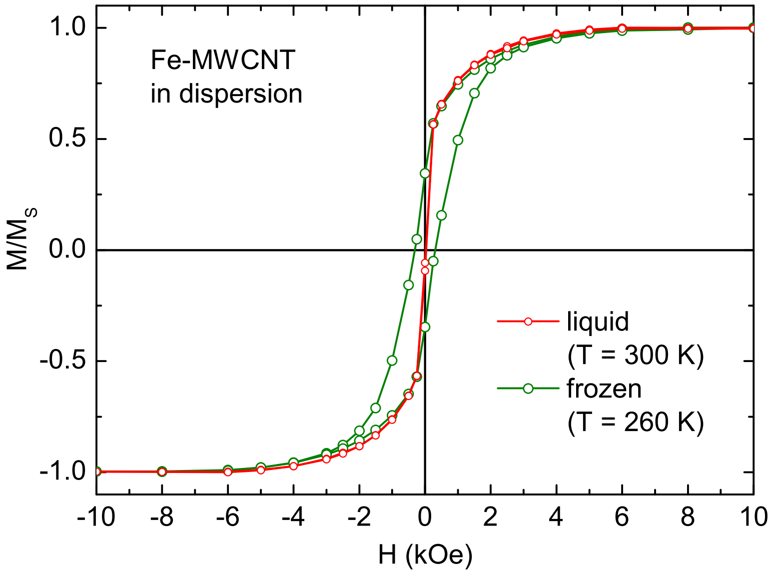

Figure 7.2: Magnetic field dependence of the magnetization $M(H)$ of the Fe-MWCNT dispersion: red curve - liquid sample ($T = 300\,\mathrm{K}$), green curve - frozen sample ($T = 260\,\mathrm{K}$).

is associated with the motion of Fe-MWCNT under exposure to the magnetic field and the Brownian relaxation of the magnetization (see section 5.1) when removed from the magnetic field. The presence of the Brownian relaxation in the Fe-MWCNT dispersion was also confirmed by the AC susceptibility measurements in the frequency range $\nu = 0 - 10\,\mathrm{kHz}$. Figure 7.3 shows the increase of the AC susceptibility of Fe-MWCNT in dispersion in comparison to the powder, which indicates the motion of Fe-MWCNT in liquid under exposure to AC magnetic fields. In general, maximal energy losses for the Brownian relaxation are observed when the condition $\nu = \nu_{\mathrm{max}} = (2\pi\tau_{\mathrm{Br}})^{-1}$ is fulfilled, where τ_{Br} is the Brownian relaxation time (ref. to section 5.1). Hence, if the applied frequency fulfils this condition the imaginary part of the AC susceptibility χ'' exhibits a maximum which indicates maximal energy absorption. The Brownian relaxation time τ_{Br} depends on the viscosity of the liquid medium η and the hydrodynamic volume V_{h} of the particle according to Eq. (5.5). For spherical iron oxide nanoparticles in liquid dispersion (with the viscosity of water $\eta = 1.01 \cdot 10^{-3}\,\mathrm{kg\,m^{-1}s^{-1}}$) the maximum energy losses have been observed for the frequency of about $1.8\,\mathrm{kHz}$ which implies a mean hydrodynamic particle diameter d_{h} of $61\,\mathrm{nm}$ [107]. In the case of Fe-MWCNT, as it is shown in Fig. 7.3, the data display a maximum of χ'' at very low frequencies $\nu < 0.2\,\mathrm{kHz}$. Such long relaxation times can be explained

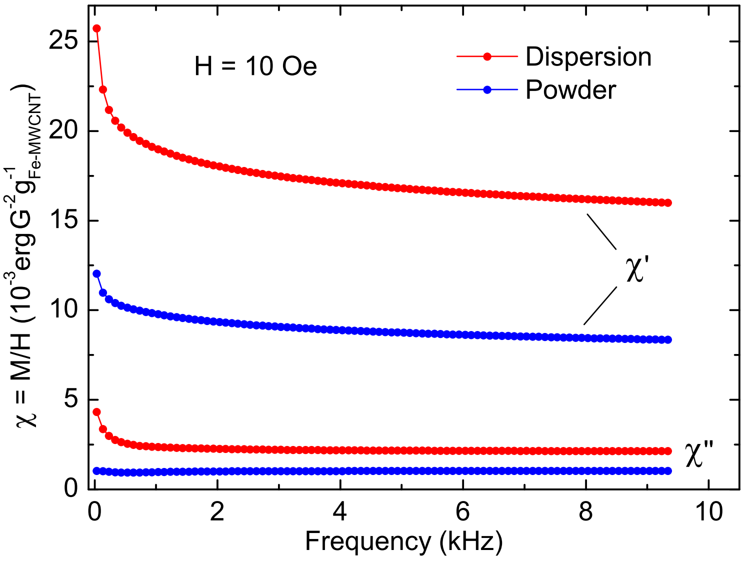

Figure 7.3: Real and imaginary parts of the AC susceptibility vs. frequency for the Fe-MWCNT dispersion and powder.

by the relatively big size and elongated shape of MWCNT, in comparison to the iron oxide nanoparticles.

Heating of Fe-MWCNT in AC magnetic fields

The calorimetrical measurements on Fe-MWCNT dispersions in AC magnetic fields show a substantial heating ability of this material. The temperature change with time for different magnetic field strengths at a frequency of 139 kHz is presented in Fig. 7.4. Here, a significant temperature increase was observed for the magnetic field strength H above 30 kA/m (375 Oe). At $H = 80$ kA/m (1000 Oe) the heating effect reaches 3 °C/min. Control measurements on purified MWCNT, CuI-filled MWCNT and C-coated Cu nanowires did not reveal any significant heating effect (Fig. 7.4). This confirms the expectation that the heating of the Fe-MWCNT dispersion is a purely magnetic effect caused by the presence of iron nanoparticles. To be specific, neither the pure MWCNT show any heating effect nor MWCNT filled with a nonmagnetic salt. The measurements performed with the C-coated Cu nanowires have experimentally proven that the observed heating effect of Fe-MWCNT is not related to eddy currents in the nanosized material under study.

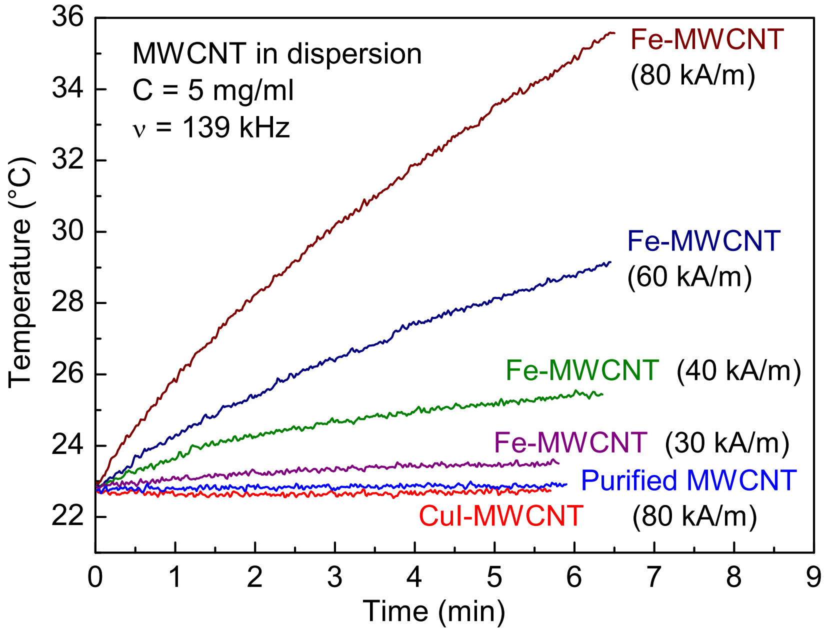

Figure 7.4: The temperature increase of Fe-MWCNT dispersion for different AC magnetic field strengths in comparison to non-magnetic control materials.

Quantitatively, the heating effectiveness of Fe-MWCNT dispersion is expressed in terms of the specific absorption rate (SAR). The SAR (in W/g) is the mass normalized rate of energy absorption by a biological object which can be determined from the initial slope of temperature vs. time curves according to Eq. (7.1) [3].

$$SAR = c\frac{\mathrm{d}T}{\mathrm{d}t}|_{t\to 0} \tag{7.1}$$

Here, c is specific heat capacity of the sample, which in the case at hand is approximated by c of water ($c_{\mathrm{water}} = 4.186\,\mathrm{J\,g^{-1}K^{-1}}$). The SAR depending on the magnetic field strength H is shown in Fig. 7.5 a. The SAR shows a quadratic dependence on the applied magnetic field strength, which is in agreement with the fact that the magnetic field energy is proportional to H^2. For better comparability of Fe-MWCNT to other magnetic materials the SAR was normalized both to the mass of Fe-MWCNT ($\mathrm{SAR_{CNT}}$) and the mass of the active material iron ($\mathrm{SAR_{Fe}}$). $\mathrm{SAR_{CNT}}$ and $\mathrm{SAR_{Fe}}$ are determined according to Eq. (7.2).

$$SAR_{\mathrm{CNT(Fe)}} = SAR\frac{m_{\mathrm{tot}}}{m_{\mathrm{CNT/Fe}}} \tag{7.2}$$

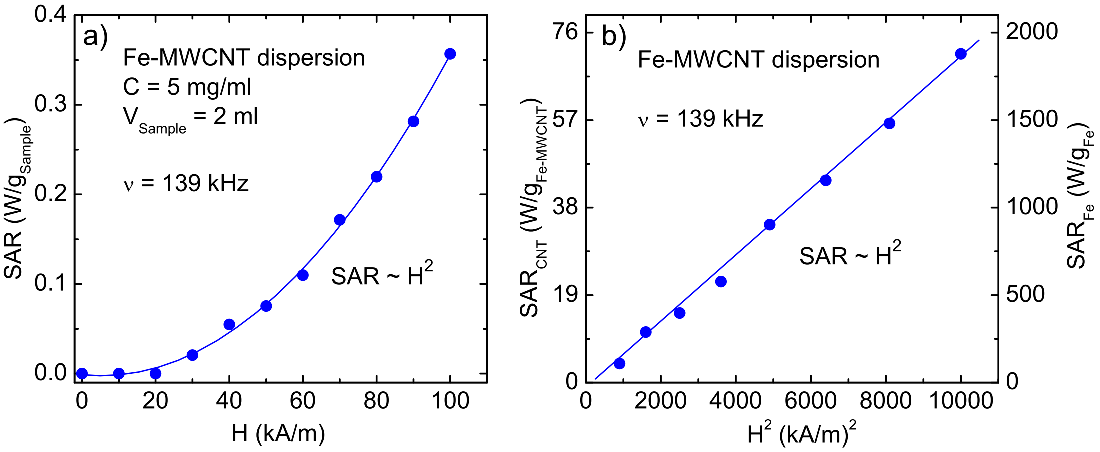

Figure 7.5: The specific absorption rate for Fe-MWCNT dispersion. a) The SAR vs. AC magnetic field strength H; b) SAR$_{CNT}$ and SAR$_{Fe}$ vs. H^2.

Here, m_{tot} is the total mass of the sample, $m_{\text{CNT/Fe}}$ is the mass of Fe-MWCNT/iron. At the maximum applied magnetic field strength of 100 kA/m (1250 Oe) SAR$_{\text{CNT}}$ and SAR$_{\text{Fe}}$ values amount to 71.4 W/g$_{\text{Fe-MWCNT}}$ and 1879 W/g$_{\text{Fe}}$, respectively. Figure 7.5 b presents SAR$_{\text{CNT}}$ and SAR$_{\text{Fe}}$ values vs. H^2 which confirms the quadratic dependence on the magnetic field strength. This quadratic dependence is in agreement with Eq. (5.4), assuming χ'' is independent of the magnetic field strength. With this assumption, the imaginary part of the AC susceptibility for the frequency $\nu = 139\,\text{kHz}$ can be calculated from SAR$_{\text{CNT}}$ according to Eq. (5.4). This calculation yields $\chi'' = 1 \cdot 10^{-3}\,\text{erg}\,\text{G}^{-2}\text{g}^{-1}_{\text{Fe-MWCNT}}$ which is in the same order of magnitude with the measured χ'' at the frequencies of around 10 kHz (see Fig. 7.3). As it was already discussed before, in the case of the Brownian relaxation the maximal energy losses are observed if the condition $\nu = 1/(2\pi\tau_{\text{Br}})$ is fulfilled. Therefore, the experimental observation of similar losses at applied frequencies of 139 kHz and 10 kHz implies that none of these frequencies fulfils this condition.

7.2 Comparison of different materials

Additionally filled Fe-MWCNT

The dissipation of the magnetic field energy is directly connected with the amount of exposed magnetic material. Therefore, an increase of the iron content in Fe-MWCNT is one of the evident ways to improve their heating ability. One of the possibilities to increase the amount of iron is the filling of MWCNT. In this case in addition to catalyst particles iron is present in the form of nanowires encapsulated by the carbon shells of the MWCNT. The filling significantly changes the magnetic properties of Fe-filled MWCNT such as coercivity and saturation magnetization. The hysteresis loop of Fe-filled MWCNT powder at room temperature ($T = 300\,\mathrm{K}$) is presented in Fig. 7.6 (red curve). The blue curve is shown for comparison and represents a hysteresis loop of unfilled MWCNT (Fe-MWCNT discussed in previous sections). These data yield a coercivity H_C of 500 Oe for Fe-filled MWCNT, while in the case of unfilled MWCNT $H_\mathrm{C} = 200\,\mathrm{Oe}$. Such a difference is caused by a strong magnetic shape anisotropy of the long iron nanowires (up to 20 μm) in comparison to almost spherical iron catalyst parti-

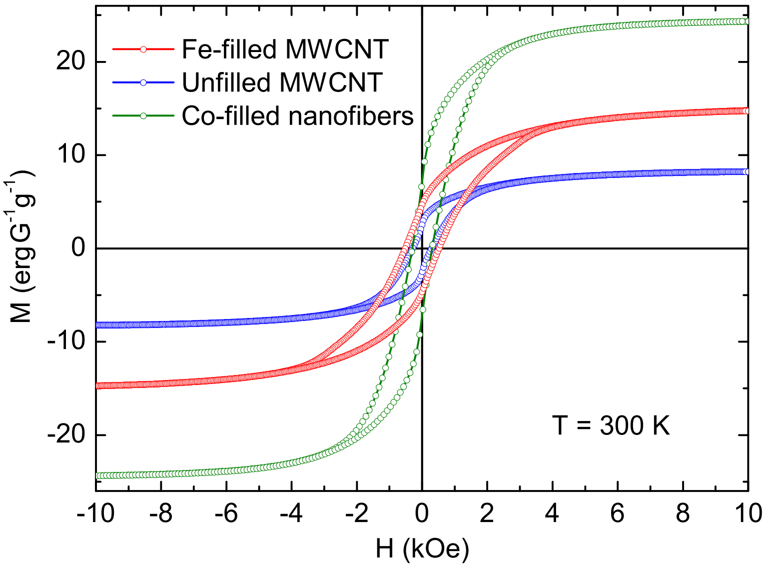

Figure 7.6: The hysteresis loops $M(H)$ of the Fe-filled MWCNT powder (red), unfilled MWCNT powder (blue) and Co-filled nanofibers (green) at room temperature.

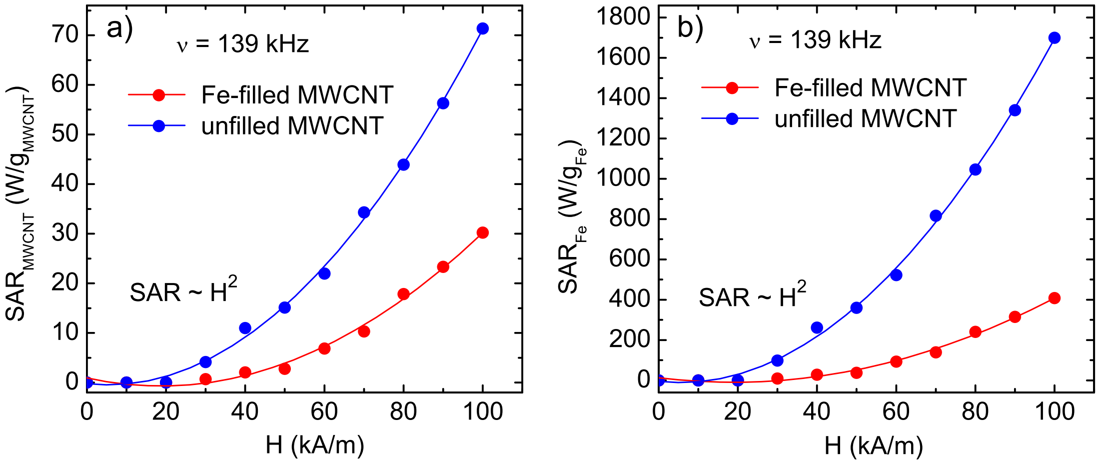

Figure 7.7: The specific absorption rate vs. AC magnetic field strength for Fe-filled MWCNT dispersion (red) and unfilled MWCNT dispersion (blue).

cles. Moreover, the saturation magnetization M_S of Fe-filled MWCNT amounts to $14.8\,\mathrm{erg\,G^{-1}g^{-1}_{MWCNT}}$ and yields $0.068\,\mathrm{g_{Fe}/g_{MWCNT}}$, while unfilled MWCNT have $0.038\,\mathrm{g_{Fe}/g_{MWCNT}}$ ($M_S = 8.2\,\mathrm{erg\,G^{-1}g^{-1}_{MWCNT}}$). This analysis shows that the amount of ferromagnetic iron inside the Fe-filled MWCNT is only two times higher than in the case of unfilled MWCNT. However, although it is known that catalyst particles are also present in the Fe-filled MWCNT, the amount of catalysts cannot be assessed. One might speculate that iron nanowires form at the expense of some catalyst material but a separation of the magnetic signal into the response of nanowires and catalyst particles, respectively, is not possible by means of the data at hand.

The heating of the Fe-filled MWCNT in AC magnetic fields has been tested as in the case of unfilled MWCNT. The specific absorption rate (SAR) (ref. to section 7.1) for Fe-filled MWCNT dispersion is presented in red color in Fig. 7.7. Again, for comparison, the SAR for unfilled MWCNT is shown in blue color here. Figure 7.7 a contains the SAR data normalized by the mass of the dry MWCNT ($\mathrm{SAR_{CNT}}$), while in Fig. 7.7 b the SAR is normalized by the mass of iron ($\mathrm{SAR_{Fe}}$). Unexpectedly, for Fe-filled MWCNT the $\mathrm{SAR_{CNT}}$ is more than two times lower than for unfilled MWCNT, while the $\mathrm{SAR_{Fe}}$ is four times lower. These observations imply much worse heating ability of Fe-nanowires in comparison to Fe-catalyst particles. The reason for this might be a strong agglomeration of iron filled nanotubes due to the dipole-dipole interaction between the iron nanowires which hinders MWCNT from motion in AC magnetic field. On the other hand, the large coercivity of the highly anisotropic Fe-nanowires disables any energy losses associated with the rotation of the magnetic moment within the particle, which could be still contributing in the case of small catalyst particles.

Co-filled nanofibers

As it was shown before, the increase of the iron content by means of filling with long nanowires did not improve the heating effect of MWCNT dispersion. Another approach to increase the amount of magnetic material is the use of cobalt filled carbon nanofibers. The high filling ratio of this material leads to rather large amount of encapsulated magnetic nanoparticles which have spherical or oblong shape with the average diameter of 15 nm. Magnetic field dependent magnetization measurements on the Co-filled nanofibers at room temperature, presented in Fig. 7.6, reveal a coercivity H_C of 310 Oe and a saturation magnetization M_S 24 erg $G^{-1}g^{-1}$. Comparison of the saturation magnetization with the corresponding bulk value of Co $M_{bulkCo} = 162$ erg $G^{-1}g^{-1}$ gives the relative amount of Co in the sample of 0.15 g_{Fe}/g_{tot}. This value is about two times higher than in the case of the studied iron filled MWCNT and about four times higher than in the case of the unfilled MWCNT. The calorimetrical measurements on a dispersion of Co-filled nanofibers show a rather strong heating effect. In particular, a

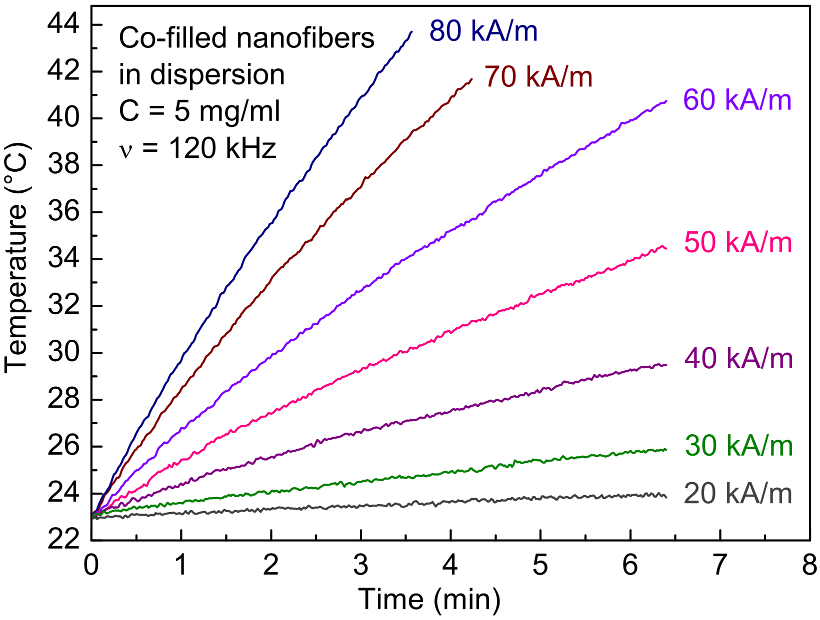

Figure 7.8: The temperature increase of Co-filled nanofibers dispersion for different AC magnetic field strengths.

significant temperature increase was observed in magnetic fields above 20 kA/m (250 Oe) with a frequency of 120 kHz (Fig. 7.8). The $\mathrm{SAR}_{\mathrm{CNT}}$ determined for the magnetic field strength $H = 80$ kA/m (1000 Oe) amounts to 98 $\mathrm{W/g_{CNT}}$, while for Fe-filled MWCNT and unfilled MWCNT it is 18 $\mathrm{W/g_{CNT}}$ and 44 $\mathrm{W/g_{CNT}}$ accordingly. Furthermore, for the same $H = 80$ kA/m the SAR normalized by the mass of active material $\mathrm{SAR}_{\mathrm{Co/Fe}}$ was determined as 653 $\mathrm{W/g_{Co}}$, 265 $\mathrm{W/g_{Fe}}$ and 1158 $\mathrm{W/g_{Fe}}$ for Co-filled nanofibers, Fe-filled MWCNT and unfilled MWCNT accordingly. Obviously, Co-filled nanofibers in dispersion produce more heat than Fe-filled MWCNT and unfilled MWCNT due to the larger amount and the spherical shape of the magnetic nanoparticles. However, the amount of heat related to the mass of the magnetic material is still much higher in the case of Fe-catalyst particles in unfilled MWCNT.

7.3 Combination of magnetic hyperthermia and chemotherapy

Resent studies on biofunctionalization of carbon encapsulated magnetic nanoparticles have shown that carboxylic functionalities can be introduced on the surface of the particles by means of acidic treatments [119]. These carboxylic functionalities have also been exploited for conjugation of the anticancer compound cisplatin [cis-diamminedichloroplatinum(II)] (CDDP) to polymers [120–122]. This complexation is based on the replacement of the chloro ligands of the drug with the carboxylic functionalities of the polymer. The method reported in those studies allows to conjugate cisplatin to carbon encapsulated magnetic nanoparticles containing carboxylic functionalities. This makes such particles a good candidate for magnetic drug delivery or bi-modal treatments based on hyperthermia and chemotherapy.

Loading and release of cisplatin

A possibility of loading the anticancer agent cisplatin to the shell of carbon encapsulated iron nanoparticles (FeNP) and its *in vitro* implications for hyperthermia therapies has been studied and published in Ref. [123]. In this work, commercially available FeNP with an average particle diameter of 25 nm (as stated by the supplier: Sun Innovations Inc., Fremont, USA) were explored in two ways:

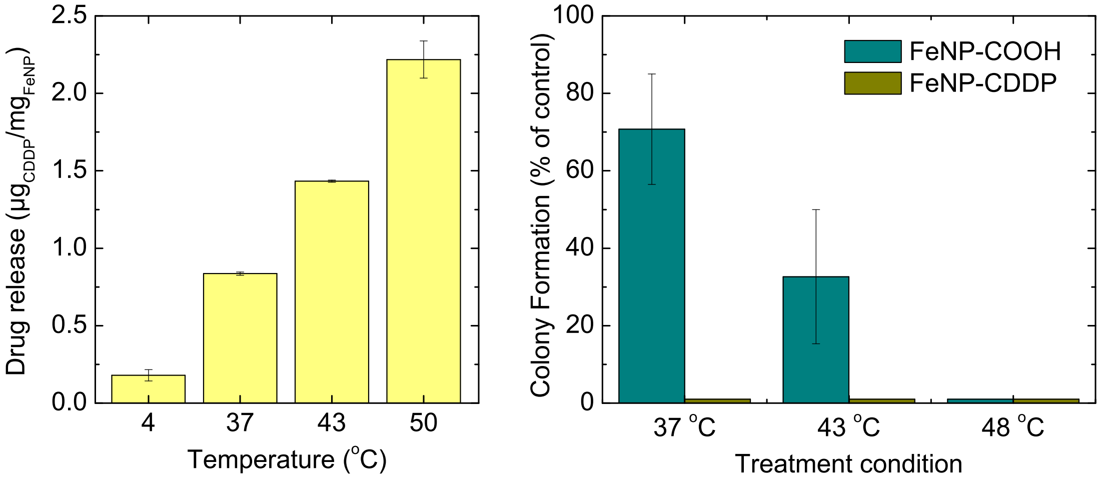

Figure 7.9: a) Temperature dependent drug release from FeNP-CDDP. b) Colony formation by cells which have undergone different thermotherapy treatments with FeNP-COOH or FeNP-CDDP. Results are normalized to control (untreated) conditions.

as a drug carrier and as a heating agent for magnetic hyperthermia. The drug loading and the cells studies have been performed by A. Taylor at the Medical Faculty of the Dresden University of Technology. Initially, in order to obtain -COOH functionalized FeNP (FeNP-COOH), FeNP were treated with nitric acid as described in Ref. [119]. After that, the drug loading was performed by means of the complexation of CDDP with carboxylic groups on the surface of the particles. After the drug was loaded, its release from the nanoparticles (FeNP-CDDP) was studied [123]. For this reason freshly prepared FeNP-CDDP in a saline solution were incubated for 30 minutes at four different temperatures and the amount of drug release was measured. This time period was chosen in accordance with clinical hyperthermia treatments which do not exceed the limit of 30 - 60 minutes. The results imply a temperature dependant release (Fig. 7.9 a). At 4 °C, less than 0.15 μg/mg of cisplatin was released. At body temperature (37 °C) 0.85 μg/mg were released and this value was nearly doubled (1.45 μg/mg) when hyperthermic temperatures were applied (43 °C). The amount of drug release reached 2.16 μg/mg at thermoablation conditions (50 °C). Those results are of interest as potential hyperthermia applications, allowing an increased drug concentration concomitant with hyperthermic temperatures.

Magnetic properties of FeNP

The application of the FeNP for hyperthermia purposes relies on their magnetic properties. Figure 7.10 shows the hysteresis loops of the raw material (FeNP) and FeNP-COOH, measured by means of the AGM (see section 6.2) at room temperature ($T = 300\,\mathrm{K}$). The acidic treatment results in a decay of the saturation magnetization, from $150\,\mathrm{erg\,G^{-1}g^{-1}}$ to $100\,\mathrm{erg\,G^{-1}g^{-1}}$ whereas the coercivity did not change. Firstly, this implies that the decay in magnetic saturation is mainly caused by loss of iron during the acidic treatments and not by its oxidation. Secondly, there is no change in the particle size and, therefore, the particles either completely dissolved or not affected at all. Although the decay is significant, the magnetic saturation is still superior to the theoretical saturation magnetization of the commonly used iron oxides ($90\,\mathrm{erg\,G^{-1}g^{-1}}$ for Fe_3O_4 and $80\,\mathrm{erg\,G^{-1}g^{-1}}$ for Fe_2O_3). The critical feature for the application of those nanoparticles, however, is the amount of heat that is generated upon exposure to an AC magnetic field. For that purpose, the calorimetrical measurements on FeNP-COOH in liquid media have been done by means of the setup described in section 6.2. The specific absorption rate was estimated for a solution with a concentration of 5 mg/ml. At the maximum applied magnetic field strength of 80 kA/m (1000 Oe) and a frequency ν of 120 kHz $\mathrm{SAR_{FeNP-COOH}}$ reaches $240\,\mathrm{W/g_{FeNP-COOH}}$, which is significantly higher then that for the materials presented in the previous sections.

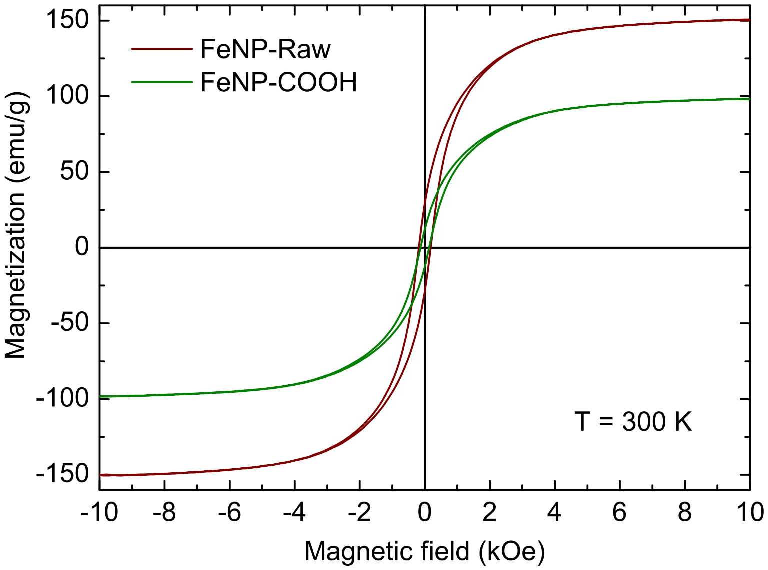

Figure 7.10: Hysteresis loop of the raw FeNP (red curve) and FeNP-COOH (blue curve) powders at room temperature ($T = 300\,\mathrm{K}$).

Combination of hyperthermia and chemotherapy in vitro

The *in vitro* efficiency of hyperthermia using FeNP-COOH or FeNP-CDDP was studied by exposing the prostate cancer cells (DU-145) to either type of nanoparticles for 30 minutes at different temperatures (37 °C, ∼ 43 °C or ∼ 48 °C) [123]. Temperatures above body temperature were reached by applying an AC magnetic field with $H = 60\,\text{kA/m}$ at $\nu = 120\,\text{kHz}$, as it was described before. The measured temperatures during treatment were of $42.5 \pm 0.3\,°\text{C}$ and $47.5 \pm 0.4\,°\text{C}$ for hyperthermic and thermoablation conditions respectively. Fig. 7.9 b shows the colony formation by 200 cells seeded after each of the treatments. Cells treated with the FeNP-COOH at 37 °C showed 29 % decay in the number of colonies which was not statistically significant. At the hyperthermia temperatures (∼ 43 °C), a significant decay in the number of colonies formed was observed, which was down to 33 % in relation to untreated cells. A complete induction of cell death at those conditions is not expected for two reasons. First, hyperthermia was induced in a single session of 30 minutes only. Second, it is recognized that the temperature sensitivity of tumors is not an intrinsic property of the cancer cells themselves but a condition which is related to the tumor physiology [124]. A temperature of 43 °C is thus not enough to have a complete cytotoxic effect under the applied conditions. At the thermoablation temperatures (∼ 48 °C), however, death by necrosis is expected, which is reflected in our results where no tumor cells survived to form colonies.

Cells exposed to the drug loaded nanoparticles (FeNP-CDDP) did not form any colonies in any of the treatment groups. Our studies of the temperature dependent drug release have shown that 30 min at 37 °C are enough to release about $0.85\,\mu\text{g}_{\text{CDDP}}/\text{mg}_{\text{FeNP}}$. That means that a 5 mg/ml FeNP-CDDP solution would lead to cisplatin concentrations higher than 4 µg/ml at this temperature. Although the exposure in this experiment was relatively short (30 min), the results clearly show that at such high drug concentrations death is induced in all cells. Even though the amount of drug released in these *in vitro* conditions was enough to kill all cells at 37 °C the situation in an *in vivo* setting would be certainly different. Depending on the case, cisplatin dosage for systemic treatments *in vivo* can be as high as 34 - 200 mg per day for a patient of average height and weight. Besides that, cells are not evenly exposed to the drugs as in *in vitro* conditions, rendering the treatment less effective. These considerations show that the typical drug load achieved in this study probably would not be completely effective in vivo at 37 °C but would certainly benefit a bi-modal treatment in combination with hyperthermia. However, *in vivo* studies are necessary to confirm these hypotheses.

7.4 AC heating in DC magnetic fields

One of the most important problems in magnetic hyperthermia applications is a control of the precise localization of the hyperthermia effect in order to increase the therapeutic effectiveness and prevent affection of healthy tissue. The conventional way to achieve spatial localization of hyperthermia effect is delivery of magnetic nanoparticles to a tumor. There are several methods to achieve a controlled delivery of hyperthermia agents to a cancer tissue: catheters, scarification, direct injection, targeting cancer cells using functionalized nanoparticles, etc. [125–127]. However, many of the methods can result in delivery of hyperthermia agents not only to cancer tissues, but also to normal tissues where the effect is undesirable. Most of the existing methods are based on invasive techniques to deliver agents directly to a tumor, but even then the agents may disperse. Moreover, invasive methods are always connected with the risks of infection and this is particularly critical in cases of such sensitive tissues like brain. Targeting cancer cells by means of antibodies is another approach for localization of

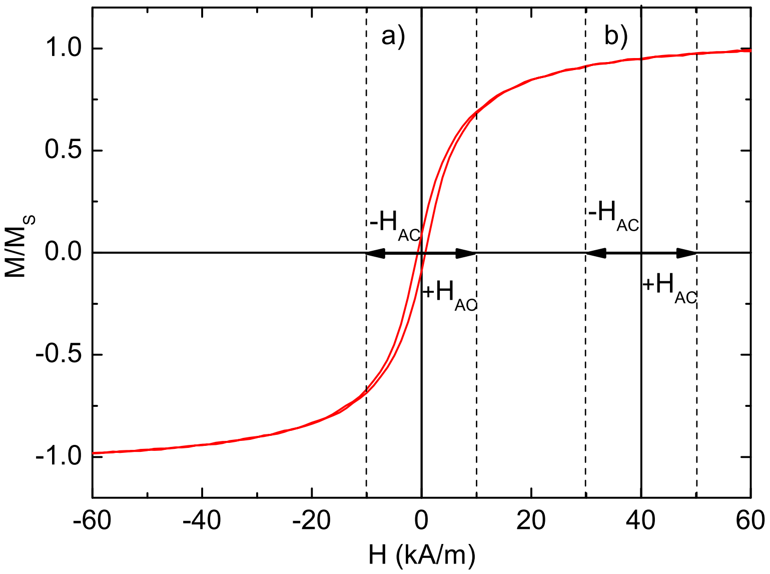

Figure 7.11: The idea of suppression of inductive heating effect in magnetic hyperthermia using an application of a DC magnetic field.

hyperthermia agents. However, targeting one form of cancer cells would mean not influencing tumor cells only, but also the same form of cells throughout the body. Thus, a specific non-invasive method for localization of hyperthermia effect would be highly desirable. This section describes an idea of spatial localization of magnetic hyperthermia effect caused by the special distribution of magnetic fields and presents the first experimental results showing the viability of this method.

The idea of this method is based on a suppression of the inductive heating effect of magnetic nanoparticles using a static (DC) magnetic field. The inductive heating of a system of magnetic particles exposed to an alternating (AC) magnetic field is directly connected to an open M vs. H loop and the hysteretic properties of the system (see e.g. Fig. 7.11 a). Changing the magnetic field direction causes magnetic energy dissipation in the system and, therefore, increases its thermal energy. An additional DC magnetic field applied to such system results in a shift of the zero (equilibrium) point of magnetic field oscillation to the level of the applied DC field (Fig. 7.11 b). The resulting magnetic field oscillates in the range where the magnetic moment of the system is almost saturated (no open $M(H)$ loop) and the change of magnetic field causes no transfer of magnetic energy into internal energy. Therefore, application of a DC magnetic field may result in the suppression of the AC magnetic heating of nanoparticles.

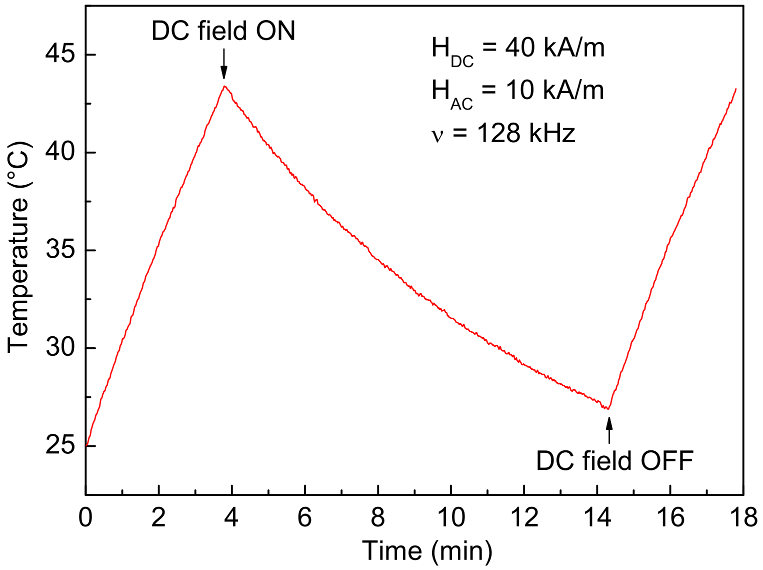

Figure 7.12: Temperature change during the applying AC and DC magnetic fields.

Experiments

In order to study the influence of the DC magnetic field on the AC magnetic heating, the inductive heating setup described in section 6.2 was combined with a 9 T superconducting magnet (Oxford Instruments). The magnetic coil system was assembled in order to place the measured sample into AC and DC magnetic fields concurrently. For this coil geometry the setup provides AC magnetic fields with a frequency of 128 kHz and magnetic field strengths of up to 120 kA/m (1500 Oe). The examined dispersion of iron oxide nanoparticles showed substantial temperature increase when exposed to the AC magnetic field ($H_{\mathrm{AC}} = 10\,\mathrm{kA/m}$ (125 Oe), $\nu = 128\,\mathrm{kHz}$) (see Fig. 7.12). After 4 minutes of exposing it to the AC field, a DC magnetic field of 40 kA/m (500 Oe) was applied to the system. In spite of the fact that the AC magnetic field was still applied the heating effect disappeared and the sample started to cool down due to the interaction with its environment. After about 10 minutes applied DC magnetic field was switched off and the heating effect appeared again. The same experiments were performed for different sequences of DC magnetic field switches (Fig. 7.13 a,b). It was proven that the observed effect of AC magnetic heating suppression is reproducible; it does not depend on the amount of switches and time interval between them, also the examined sample demonstrates identical heating properties before and after performed experiments. Moreover, Fig. 7.13 b illustrates that applying of certain consecutions of DC magnetic field switches results in holding the average temperature at a certain level.

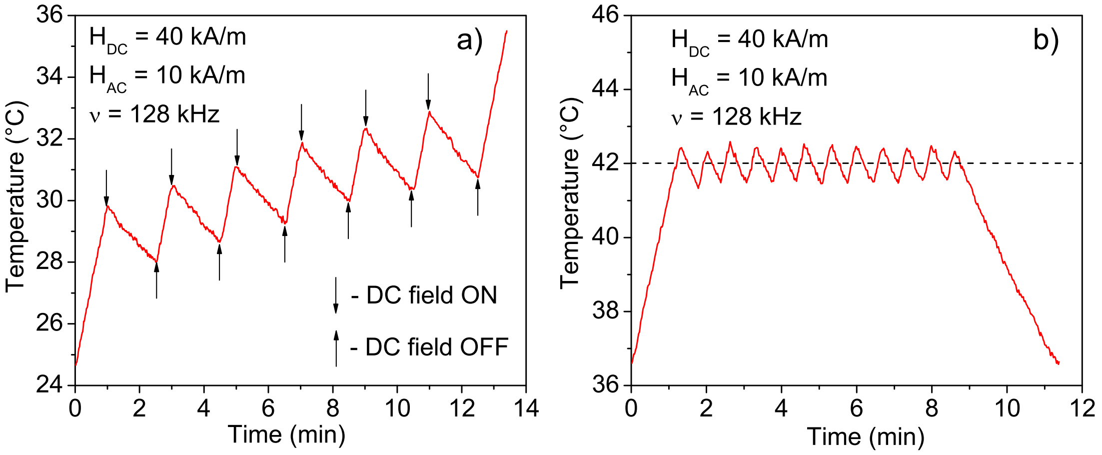

Figure 7.13: Temperature change during the applying AC and DC magnetic fields for different consecutions of DC magnetic field switches.

8 Summary (Part II)

In this (second) part of the thesis a detailed study of magnetically functionalized carbon nanotubes is presented. Obtained results reveal a ferromagnetic behavior of the encapsulated catalyst nanoparticles as well as of the additional fillings. Moreover, it was shown that spherical iron and cobalt nanoparticles encapsulated by carbon nanotubes (Fe-MWCNT) and nanofibers produce a substantial amount of heat while exposed to an AC magnetic field. However, the additional filling of Fe-MWCNT with highly anisotropic Fe-nanowires does not improve the heating ability of this material. This reveals a strong dependence of the AC heating on the shape of the magnetic particles. Furthermore, it was shown that the surface functionalization of carbon coated nanoparticles allows their loading with the drug cisplatin which is released in saline solutions. The results of the *in vitro* studies have shown that such particles can be successfully applied as multimodal anti-cancer agents for a concomitant therapy based on hyperthermia and chemotherapy. In addition, a method of an inductive heating suppression via the application of a DC magnetic field has been presented. This method, in combination with specially distributed DC magnetic fields, enables a spatial localization of the hyperthermia effects in a human body.

Bibliography

[1] M. Todorovic, S. Schultz, J. Wong, and A. Scherer. Writing and reading of single magnetic domain per bit perpendicular patterned media. *Appl. Phys. Lett.* **74,** 2516, 1999.

[2] Q. A. Pankhurst, J. Connolly, S. K. Jones, and J. Dobson. Applications of magnetic nanoparticles in biomedicine. *J. Phys. D: Appl. Phys.* **36,** R167 - R181, 2003.

[3] C. S. S. R. Kumar (Ed.). Nanomaterials for Cancer Therapy. *Wiley-VCH, Weinheim*, 2006.

[4] W. Wernsdorfer. Molecular nanomagnets: towards molecular spintronics. *Int. J. Nanotechnology* **7,** 497-522, 2010.

[5] Jr. C. P. Poole. Electron Spin Resonance: A Comprehensive Treatise on Experimental Techniques. *Wiley-Interscience, New York*, 1967.

[6] F. Hund. Zur Deutung Verwickelter Spektren, Insbesondere der Elemente Scandium bis Nickel. *Z. Phy.* **33,** 345-371, 1925.

[7] A. Abragam and B. Bleaney. Electron Paramagnetic Resonance of Transition Ions. *Oxford University Press, London*, 1970.

[8] N. Majlis. The Quantum Theory of Magnetism. *World Scientific Publishing Co. Pte. Ltd., Singapore*, 2000.

[9] P. Fazekas. Lecture Notes on Electron Correlation and Magnetism. *World Scientific Publishing Co. Pte. Ltd., Singapore*, 1999.

[10] A. Schweiger and G. Jeschke. Principles of Pulse Electron Paramagnetic Resonance. *Oxford University Press, Oxford*, 2001.

[11] D. Gatteschi, R. Sessoli, and J. Villain. Molecular Nanomagnets. *Oxford University Press, Oxford*, 2006.

[12] A. Abragam. The principles of nuclear magnetism. *Clarendon Press, Oxford*, 1961.

[13] E. Hahn. Spin Echoes. *Phys. Rev.* **80,** 580-594, 1950.

[14] C. Golze. Tunable High-Field / High-Frequency ESR and High-Field Magnetization on Single-Molecule Clusters. PhD thesis Dresden University of Technology, 2007.

[15] S. Foner. Versatile and Sensitive Vibrating-Sample Magnetometer. *The Review of Scientific Instruments.*

[16] M. Hücker. Aufbau eines Hochfeldmagnetometers und Studiun der magnetischen Ordnung in dotiertem La_2CuO_4. PhD thesis, University of Cologne, 1999.

[17] http://www.fzd.de/db/Cms?pNid=580.

[18] S. Stoll and A. Schweiger. EasySpin, a comprehensive software package for spectral simulation and analysis in EPR. *J Magn Reson* **178(1),** 42-55, 2006.

[19] http://ewww.mpi muelheim.mpg.de/bac/logins/bill/julX_en.php.

[20] A. M. Ako, I. J. Hewitt, V. Mereacre, R. Clérac, W. Wernsdorfer, C. E. Anson, and A. K. Powell. A Ferromagnetically Coupled Mn_{19} Aggregate with a Record $s = 83/2$ Ground Spin State. *Angew. Chem. Int. Ed.* **45,** 4296-4299; Angew. Chem. **118,** 5048-5051, 2006.

[21] http://www.pi1.physik.uni stuttgart.de/molmagn/Results1_e.php.

[22] T. Lis. Preparation, structure, and magnetic properties of a dodecanuclear mixed-valence manganese carboxylate. *Acta Crystallogr.* **B36,** 2042-2046, 1980.

[23] J. R. Friedman, M. P. Sarachik, J. Tejada, , and R. Ziolo. Macroscopic Measurement of Resonant Magnetization Tunneling in High-Spin Molecules. *Phys. Rev. Lett.* **76,** 3830-3833, 1996.

[24] L. Thomas, F. Lionti, R. Ballou, D. Gatteschi, R. Sessoli, and B. Barbara. Macroscopic Quantum Tunnelling of Magnetization in a Single Crystal of Nanomagnets. *Nature (London)* **383,** 145-147, 1996.

[25] I. G. Dance. The structural chemistry of metal thiolate complexes. *Polyhedron* **5,** 1037-1104, 1986.

[26] M. A. Halcrow and G. Christou. Biomimetic chemistry of nickel. *Chem. Rev.* **94,** 2421-2481, 1994.

[27] P. J. Blower and J. R. Dilworth. Thiolato-complexes of the transition metals. *Coord. Chem. Rev.* **76,** 121-185, 1987.

[28] G. Henkel and B. Krebs. Metallothioneins: zinc, cadmium, mercury, and copper thiolates and selenolates mimicking protein active site features - structural aspects and biological implications. *Chem. Rev.* **104,** 801-824, 2004.

[29] C. A. Grapperhaus and M. J. Darensbourg. Oxygen Capture by Sulfur in Nickel Thiolates. *Acc. Chem. Res.* **31,** 451-459, 1998.

[30] D. Sellmann and J. Sutter. In Quest of Competitive Catalysts for Nitrogenases and Other Metal Sulfur Enzymes. *Chem. Res.* **30,** 460-469, 1997.

[31] A. C. Marr, D. J. E. Spencer, and M. Schröder. Structural mimics for the active site of [NiFe] hydrogenase. *Coord. Chem. Rev.* **219-221,** 1055-1074, 2001.

[32] T. Beissel, K. S. Bürger, G. Voigt, K. Wieghardt, C. Butzlaff, and A. X. Trautwein. (1,4,7-Tris(4-tert-butyl-2-mercaptobenzyl)-1,4,7-triazacyclononane)iron(III): a model for the iron-sulfur center in nitrile hydratase from Brevibacterium, sp. *Inorg. Chem.* **32,** 124-126, 1993.

[33] T. Glaser, T. Beissel, E. Bill, T. Weyhermuller, V. Schunemann, W. Meyer-Klaucke, A. X. Trautwein, and K. Wieghardt. The Electronic Structure of Linear Thiophenolate Bridged Heterotrinuclear Complexes [LFeMFeL]$^{n+}$ (M=Cr, Co, Fe; n=1 - 3): Localized vs Delocalized Models. *J. Am. Chem. Soc.* **121,** 2193-2208, 1999.

[34] H.-J. Krüger and R. H. Holm. Stabilization of trivalent nickel in tetragonal NiS_4N_2 and NiN_6 environments: synthesis, structures, redox potentials and observations related to [NiFe]-hydrogenases. *J. Am. Chem. Soc.* **112,** 2955-2963, 1990.

[35] P. Zanello, S. Tamburini, P. A. Vigato, and G. A. Mazzochin. Synthesis, structure and electrochemical characterization of homo- and heterodinuclear copper complexes with compartmental ligands. *Coord. Chem. Rev.* **77,** 165-273, 1987.

[36] S. Brooker. Complexes of thiophenolate-containing Schiff-base macrocycles and their amine analogues. *Coord. Chem. Rev.* **222,** 33-56, 2001.

[37] V. Lozan, C. Loose, J. Kortus, and B. Kersting. Coordination chemistry of Robson-type polyamine-dithiophenolate macrocycles: Syntheses, structures and magnetic properties of dinuclear complexes of first-row transition metals. *Coord. Chem. Rev.* **253,** 2244-2260, 2009.

[38] J. Hausmann, M. H. Klingele, V. Lozan, G. Steinfeld, D. Siebert, Y. Journaux, J. J. Girerd, and B. Kersting. Realization of Unusual Substrate Binding Motifs in Metalated Container Complexes. Synthesis, Structures, and Magnetic Properties of the Complexes $[(\mathrm{L}^{\mathrm{Me}})\mathrm{Ni}_2(\mu\text{-L}')]^{n+}$ with $\mathrm{L}'{=}\mathrm{NO}_3^-$, NO_2^-, N_3^-, $\mathrm{N}_2\mathrm{H}_4$, Pyridazine, Phthalazine, Pyrazolate, and Benzoate. *Chem. Eur. J.* **10,** 1716-1728, 2004.

[39] Y. Journaux, J. Hausmann, V. Lozan, and B. Kersting. Stabilisation of a paramagnetic borohydrido-bridged dinickel(II) complex by a macrodinucleating hexaaza-dithiophenolate ligand. *Chem. Commun.* 83-84, 2006.

[40] T. Glaser, Y. Journaux, G. Steinfeld, V. Lozan, and B. Kersting. Preparation and Characterization of Cr(III), Mn(II), Fe(II), Co(II) and Ni(II) complexes of a hexaaza-dithiophenolate macrocycle. *J. Chem. Soc. Dalton Trans.* 1738-1748, 2006.

[41] V. Lozan and B. Kersting. Macrocyclic Nickel(II) Complexes Coligated by Hydrosulfide and Hexasulfide Ions: Syntheses, Structures, and Magnetic Properties of $[\mathrm{Ni}_2^{\mathrm{II}}\mathrm{L}(\mu\text{-SH})]^+$ and $[(\mathrm{LNi}_2^{\mathrm{II}})_2(\mu\text{-S}_6)]^{2+}$. *Inorg. Chem.* **47,** 5386-5393, 2008.

[42] J. Goodenough. Magnetism and the Chemical Bond. *John Wiley and Sons, New York*, 1963.

[43] V. Yu. Yushankhai and R. Hayn. Anisotropic superexchange of a 90° Cu-O-Cu bond. *Europhys. Lett.* **47,** 116-121, 1999.

[44] S. Tornow, O. Entin-Wohlman, and A. Aharony. Anisotropic superexchange for nearest and next-nearest coppers in chain, ladder, and lamellar cuprates. *Phys. Rev. B* **60,** 10206-10215, 1999.

[45] O. Kahn. Molecular Magnetism. *Wiley-VCH, Weinheim*, 1993.

[46] J. S. Miller and M. Drillon. Eds. Magnetism: Molecules to Materials. *Wiley-VCH, Weinheim*, 2001.

[47] E. Coronado, P. Delhaes, D. Gatteschi, and J. S. Miller. Eds. Molecular magnetism: From Molecular Assemblies to Devices. *NATO ASI Series, Kluwer, Dordrecht: The Netherlands* **321**, 1995.

[48] Y. Krupskaya, A. Alfonsov, A. Parameswaran, V. Kataev, R. Klingeler, G. Steinfeld, N. Beyer, M. Gressenbuch, B. Kersting, and B Büchner. Interplay of Magnetic Exchange Interactions and Ni-S-Ni Bond Angles in Polynuclear Nickel(II) Complexes. *ChemPhysChem* **11,** 1961-1970, 2010.

[49] H. Miyasaka and M. Yamashita. A look at molecular nanosized magnets from the aspect of inter-molecular interaction. *Dalton Trans.* 399-406, 2007.

[50] H. Oshio, M. Nihei, A. Yoshida, H. Nojiri, M. Nakano, A. Yamaguchi, Y. Karaki, and H. Ishimoto. A Dinuclear $\mathrm{Mn^{III}}$-$\mathrm{Cu^{II}}$ Single-Molecule Magnet. *Chem. Eur. J.* **11,** 843-848, 2005.

[51] H. Oshio, M. Nihei, S. Koizumi, T. Shiga, H. Nojiri, M. Nakano, N. Shirakawa, and M. Akatsu. A Heterometal Single-Molecule Magnet of $[\mathrm{Mn_2^{III}Ni_2^{II}Cl_2(salpa)_2}]$. *J. Am. Chem. Soc.* **127,** 4568-4569, 2005.

[52] C. Kachi-Terajima, H. Miyasaka, A. Saitoh, N. Shirakawa, M. Yamashita, and R. Clérac. Single-Molecule Magnet Behavior in Heterometallic $\mathrm{M^{II}}$-$\mathrm{Mn_2^{III}}$-$\mathrm{M^{II}}$ Tetramers ($\mathrm{M^{II}}$ = Cu, Ni) Containing $\mathrm{Mn^{III}}$ Salen-Type Dinuclear Core. *Inorg. Chem.* **46,** 5861-5872, 2007.

[53] D. Li, S. Parkin, G. Wang, T. G. Yee, R. Cleérac, W. Wernsdorfer, and M. S. Holmes. An $S = 6$ Cyano-Bridged Octanuclear $\mathrm{Fe_4^{III}Ni_4^{II}}$ Complex that Exhibits Slow Relaxation of the Magnetization. *J. Am. Chem. Soc.* **128,** 4214-4215, 2006.

[54] T. Glaser, M. Heidemeier, T. Weyhermüller, R.-D. Hoffmann, H. Rupp, and P. Müller. Property-Oriented Rational Design of Single-Molecule Magnets: A C_3-Symmetric $\mathrm{Mn_6Cr}$ Complex Based on Three Molecular Building

Blocks with a Spin Ground State of $S_t = 21/2$. *Angew. Chem. Int. Ed.* **45,** 6033-6037, 2006.

[55] A. Das, K. Gieb, Y. Krupskaya, S. Demeshko, S. Dechert, R. Klingeler, V. Kataev, B. Büchner, P. Müller, and F. Meyer. A New Family of 1D Exchange Biased Heterometal Single-Molecule Magnets: Observation of Pronounced Quantum Tunneling Steps in the Hysteresis Loops of Quasi-Linear {Mn2Ni3} Clusters. *J. Am. Chem. Soc.* **133,** 3433-3443, 2011.

[56] W. Wernsdorfer, N. Aliaga-Alcalde, D. N. Hendrickson, and G. Christou. Title. *Nature* **416,** 406-409, 2002.

[57] S. Hill, R. S. Edwards, N. Aliaga-Alcalde, and G. Christou. Quantum Coherence in an Exchange-Coupled Dimer of Single-Molecule Magnets. *Science* **302,** 1015-1018, 2003.

[58] A. Caneschi, D. Gatteschi, N. Lalioti, C. Sangregorio, R. Sessoli, G. Venturi, A. Vindigni, A. Rettori, M. G. Pini, and M. A. Novak. Cobalt(II)-Nitronyl Nitroxide Chains as Molecular Magnetic Nanowires. *Angew. Chem. Int. Ed.* **40,** 1760-1763; Angew. Chem. **113,** 1810-1813, 2001.

[59] R. Clérac, H. Miyasaka, M. Yamashita, and C. Coulon. Evidence for Single-Chain Magnet Behavior in a Mn^{III}-Ni^{II} Chain Designed with High Spin Magnetic Units: A Route to High Temperature Metastable Magnets. *J. Am. Chem. Soc.* **124,** 12837-12844, 2002.

[60] M. Ferbinteanu, H. Miyasaka, W. Wernsdorfer, K. i. Nakata, K. Sugiura, M. Yamashita, C. Coulon, and R. Clerac. Single-Chain Magnet $(Net_4)[Mn_2(5\text{-}MeOsalen)_2Fe(CN)_6]$ Made of Mn^{III}-Fe^{II}-Mn^{III} Trinuclear Single-Molecule Magnet with an ST=9/2 Spin Ground State. *J. Am. Chem. Soc.* **127,** 3090-3099, 2005.

[61] M. Bałanda, M. Rams, S. K. Nayak, Z. Tomkowicz, W. Haase, K. Tomala, and J. V. Yakhmi. Slow magnetic relaxations in the anisotropic Heisenberg chain compound Mn(III) tetra(*ortho*-fluorophenyl)porphyrin-tetracyanoethylene. *Phys. Rev. B* **74,** 224421, 2006.

[62] E. J. Brandon, D. K. Rittenberg, A. M. Arif, and J. S. Miller. Ferrimagnetic Behavior of Multiple Phases and Solvates of (*meso*-Tetrakis(4-chlorophenyl)porphinato)manganese(III) Tetracyanoethenide,

$[MnTClPP]^+[TCNE]^-$. Enhancement of Magnetic Coupling by Thermal Annealing. *Inorg. Chem.* **37,** 3376-3384, 1998.

[63] E. J. Brandon, A. M. Arif, B. M. Burkhart, and J. S. Miller. Structure and Magnetic Properties of Antiferromagnetic Manganese(III) Tetrakis(4-methoxyphenyl)porphyrin Tetracyanoethenide, [MnTOMePP][TCNE]·2PhMe, and Manganese(III) Tetrakis(2-fluorophenyl)porphyrin Tetracyanoethenide, [MnTFPP][TCNE]·2PhMe. *Inorg. Chem.* **37,** 2792-2798, 1998.

[64] D. K. Rittenberg and J. S. Miller. Observation of Magnetic Ordering as High as 28 K for meso-Tetrakis(4-halophenyl)porphinatomanganese(III) Tetracyanoethenide, [MnTXPP][TCNE] (X = F, Br, I). *Inorg. Chem.* **38,** 4838-4848, 1999.

[65] M. Fardis, G. Diamantopoulos, G. Papavassiliou, K. Pokhodnya, J. S. Miller, D. K. Rittenberg, and C. Christides. ^{1}H NMR investigation of the magnetic spin configuration in the molecule-based ferrimagnet [MnTFPP][TCNE]. *Phys. Rev. B* **66,** 064422, 2002.

[66] D. Gatteschi and R. Sessoli. Quantum Tunneling of Magnetization and Related Phenomena in Molecular Materials. *Angew. Chem., Int. Ed.* **42,** 268-297, 2003.

[67] J. Brockman, Kh. Abboud, D. N. Hendrickson, and G. Christou. A new family of Mn-12 single-molecule magnets: replacement of carboxylate ligands with diphenylphosphinates. *Polyhedron* **22,** 1765-1769, 2003.

[68] C. von Hänisch, F. Weigend, and R. Clérac. Unique Manganese Phosphorus Complex with a Mn_5P_7 Core: Synthesis, Molecular Structure, and Magnetic Properties. *Inorg. Chem.* **47,** 1460-1464, 2008.

[69] E. Dagotto. Nanoscale Phase Separation and Colossal Magnetoresistance. *Springer-Verlag: Berlin*, 2002.

[70] M. Brandmayer, R. Clérac, F. Weigend, and S. Dehnen. Ortho-Chalcogenostannate Anions as Ligands: Syntheses, Crystal Structures, Electronic Properties and Magnetism of Novel Compounds Containing Ternary Anionic Substructures $[M_4(\mu_4\text{-Se})(SnSe_4)_4]^{10-}$ (M = Cd, Hg), $\{[Hg_4(\mu_4\text{-Se})_4(SnSe_4)_3]^{6-}\}_n$ or $\{[HgSnSe_4]^{2-}\}_n$. *Chem.-Eur. J.* **10,** 5147-5157, 2004.

[71] A. Escuer and G. Aromí. Azide as a Bridging Ligand and Magnetic Coupler in Transition Metal Clusters. *Eur. J. Inorg. Chem.* 4721-4736, 2006.

[72] V. Miluykov, I. Bezkishko, D. Krivolapov, O. Kataeva, O. Sinyashin, E. Hey-Hawkins, A. Parameswaran, Y. Krupskaya, V. Kataev, R. Klingeler, and B Büchner. Binuclear 1,2-Diphosphacyclopentadienyl Manganese(I) Complexes: Synthesis, Structure and Magnetic Properties. *Organometallics* **29,** 1339-1342, 2010.

[73] F. Heinemann, H. Pritzkow, M. Zeller, and U. Zenneck. 1,2,4-Triphospholyl Nickel Complexes: Evidence for a Dimerization Equilibrium That Includes a σ-π Rearrangement of the Triphospholyl Ligand. *Organometallics* **19,** 4283-4288, 2000.

[74] M. Al-Ktaifani, P. Hitchcock, and J. Nixon. 1,2,4-Triphospholyl gold(I) and copper(I) complexes: synthesis, crystal and molecular structures of $[Cu(PMe_3)_2(\mu\text{-}P_3C^t_2Bu_2)(\mu\text{-}I)Cu(PMe_3)_2]$, $[Cu(PMe_3)_2(\mu\text{-}P_3C^t_2Bu_2)_2Cu(PMe_3)_2]$ and $[Au(\eta^1\text{-}P_3C^t_2Bu_2)_2][Au(PEt_3)_2]$. *J. Organomet. Chem.* **665,** 101-106, 2003.

[75] V. Miluykov, A. Kataev, O. Sinyashin, P. Lönnecke, and E. Hey-Hawkins. The reaction of NaP_5 with half sandwich complexes of nickel - the first example of a Ni-promoted transformation of the P_5 anion. *Organometallics* **24,** 2233-2236, 2005.

[76] B. Cordero, V. Gomez, A. Platero-Prats, M. Reves, J. Echeverria, E. Cremades, F. Barragan, and A. Alvarez. Covalent radii revisited. *Dalton Trans.* 2832-2838, 2008.

[77] R. A. Bartlett, H. V. R. Dias, K. M. Flynn, H. Hope, B. D. Murray, M. M. Olmstead, and P. P. Power. Reaction of Bulky Monosubstituted Phosphorus(III) Halides with Disodium Pentacarbonylchromate. Steric and Electronic Factors in the Synthesis of Cr(CO)5 Complexes of Diphosphenes, Phosphinidines, Phosphanes, Diphosphanes, and Cyclopolyphosphanes. *J. Am. Chem. Soc.* **109,** 5693-5698, 1987.

[78] P. Jutzi, U. Meyer, S. Opiela, B. Neumann, and H.-G. Stammler. η^1- und η^2-Komplexe von Cp*-substituierten Diphosphenen und Arsaphosphenen: Synthese, Struktur und Umlagerung unter Cp*-Wanderung. *J. Organomet. Chem.* **439,** 279-301, 1992.

[79] M. Yoshifuji, N. Shinohara, and K. Toyota. Application of 1,2-Bis(2-bromo-3,5-di-*t*-butylphenyl)ethane to Preparation of Compounds Having Two Diphosphene Units. *Tetrahedron Lett.* **37,** 7815-7818, 1996.

[80] J. D. Korp, I. Bernal, J. L. Atwood, W. E. Hunter, F. Calderazzo, and D. Vitali. Studies on organometallic compounds with hetero multiple bridges. X-Ray crystal and molecular structure of $Mn_2Br_2(CO)_6P_2Ph_4$, the product resulting from co-ordinative addition of P_2Ph_4 to manganese(I). *Chem. Commun.* 576-577, 1979.

[81] T. W. Graham, K. A. Udachin, and A. J. Carty. Synthesis of σ-π-phosphinidene sulfide complexes $[Mn_2(CO)_n(\mu\text{-}\eta^1,\eta^2\text{-}P(NR_2){=}S)]$ ($n = 8$, 9) via direct sulfuration of electrophilic μ-phosphinidenes and photochemical transformation to a trigonal prismatic $Mn_2P_2S_2$ cluster. *Inorg. Chim. Acta* **360,** 1376-1379, 2007.

[82] J. Livorness, T. D. Smith, J. R. Pilbrow, and G. R. Sinclair. Electron spin resonance study of the manganese(II) chelate of tetrasodium 3,10,17,24-tetrasulphonatophthalocyanine. *J. Chem. Soc., Faraday Trans. II* **80,** 425-436, 1984.

[83] J. R. Pilbrow. Transition Ion Electron Paramagnetic Resonance. *Clarendon Press: Oxford*, 1990.

[84] T. D. Ladd, F. Jelezko, R. Laflamme, Y. Nakamura, C. Monroe, and J. L. O'Brien. Quantum computers. *Nature* **464,** 45-53, 2010.

[85] A. Ardavan, O. Rival, J. J. L. Morton, S. J. Blundell, A. M. Tyryshkin, G. A. Timco, and R. E. P. Winpenny. Will Spin-Relaxation Times in Molecular Magnets Permit Quantum Information Processing? *Phys. Rev. Lett.* **98,** 057201, 2007.

[86] C. Schlegel, J. van Slageren, M. Manoli, E. K. Brechin, and M. Dressel. Direct Observation of Quantum Coherence in Single-Molecule Magnets. *Phys. Rev. Lett.* **101,** 147203, 2008.

[87] S. Takahashi, J. van Tol, C. C. Beedle, D. N. Hendrickson, L.-C. Brunel, and M. S. Sherwin. Coherent Manipulation and Decoherence of $S = 10$ Single-Molecule Magnets. *Phys. Rev. Lett.* **102,** 087603, 2009.

[88] W. B. Mims. Envelope Modulation in Spin-Echo Experiments. *Phys. Rev. B* **5,** 2409-2419, 1972.

[89] K. M. Salikhov, A. G. Semenov, and Y. D. Tsvetkov. Electron Spin Echoes and Their Applications. *Science: Novosibirsk*, 1979.

[90] S. A. Dikanov and Y. D. Tsvetkov. Electron Spin-Echo Modulation (ESEEM) Spectroscopy. *CRC Press: Boca Raton, FL*, 1992.

[91] K. M. Salikhov and Y. D. Tzvetkov. in Time Domain Electron Spin Resonance, edited by L. Kevan and R. N. Schwartz. *Wiley, New York,* chap. 7, 1979.

[92] R. Konda, J.-L. Du, S. S. Eaton, and G. R. Eaton. Electron spin relaxation rates for nitridochromium(V) tetratolylporphyrin and nitridochromium(V) octaethylporphyrin in Frozen solution. *Appl. Mag. Res.* **7,** 185-193, 1994.

[93] V. Kathirvelu, H. Sato, S. S. Eaton, and G. R. Eaton. Electron spin relaxation rates for semiquinones between 25 and 295K in glass-forming solvents. *J. Magn. Res.* **198,** 111-120, 2009.

[94] N. B. Blombergen, S. Shapiro, P. S. Persan, and J. O. Artman. Cross-Relaxation in Spin Systems. *Phys. Rev.* **114,** 445-459, 1959.

[95] A. Jordan, R. Scholz, P. Wust, H. Fahling, and R. Felix. Magnetic fluid hyperthermia (MFH): Cancer treatment with AC magnetic field induced excitation of biocompatible superparamagnetic nanoparticles. *J. Magn. Magn. Mat.* **201,** 413-419, 1999.

[96] M. Johannsen, B. Thiesen, A. Jordan, K. Taymoorian, U. Gneveckow, N. Waldöfner, R. Scholz, M. Koch, M. Lein, K. Jung, and S. A. Loening. Magnetic fluid hyperthermia (MFH) reduces prostate cancer growth in the orthotopic Dunning R3327 rat model. *Prostate* **64,** 283-292, 2005.

[97] F. Matsuoka, M. Shinkai, H. Honda, T. Kubo, T. Sugita, and T. Kobayashi. Hyperthermia using magnetite cationic liposomes for hamster osteosarcoma. *Biomagnetic Research and Technology* **2,** 3, 2004.

[98] M. Johannsen, U. Gneveckow, K. Taymoorian, B. Thiesen, N. Waldöfner, R. Scholz, K. Jung, A. Jordan, P.Wust, and S. A. Loening. Morbidity and quality of life during thermotherapy using magnetic nanoparticles in

locally recurrent prostate cancer: Results of a prospective phase I trial. *International Journal of Hyperthermia* **23,** 315-323, 2007.

[99] R. Klingeler, S. Hampel, and B. Büchner. Carbon nanotube based biomedical agents for heating, temperature sensoring and drug delivery. *Int. J. Hyperthermia* **24(6),** 496-505, 2008.

[100] S. Karmakar, S. M. Sharma, M. D. Mukadam, S. M. Yusuf, and A. K. Sood. Carbon nanotube based biomedical agents for heating, temperature sensoring and drug delivery. *J. Appl. Phys.* **97,** 054306, 2005.

[101] A. Taylor, K. Lipert, K. Krämer, S. Hampel, S. Füssel, A. Meye, R. Klingeler, M. Ritschel, B. Büchner, and M. P. Wirth. Biocompatibility of Iron Filled Carbon Nanotubes In Vitro. *J. Nanosci. Nanotechnol.* **9,** 5709-5716, 2009.

[102] R. Hergt, S. Dutz, R. Müller, and M. Zeisberger. Magnetic particle hyperthermia: nanoparticle magnetism and materials development for cancer therapy. *J. Phys.: Condens. Matter* **18,** S2919-S2934, 2006.

[103] M. Farle. Magnetism goes Nano, C4, Magnetic Nanoparticles. *Forchungszentrum Juelich*, 2005.

[104] W. C. Elmore. The Magnetization of Ferromagnetic Colloids. *Phys. Rev.* **54,** 1092-1095, 1938.

[105] R. E. Rosensweig. Heating magnetic fluid with alternating magnetic field. *J. Magn. Magn. Mater.* **252,** 370-374 , 2002.

[106] P. Debye. Polar Molecules. *The Chemical Catalog Company, New York*, 1929.

[107] R. Hergt, R. Hiergeist, I. Hilger, W. A. Kaiser, Y. Lapatnikov, S. Margel, and U. Richterd. Maghemite nanoparticles with very high AC-losses for application in RF-magnetic hyperthermia. *J. Magn. Magn. Mater.* **270,** 345-357, 2004.

[108] I. Mălăescu and I. Hrianca. Relaxation processes of magnetite-based ferrofluids in rf magnetic fields. *J. Magn. Magn. Mater.* **157/158,** 585-586, 1996.

[109] P. C. Fannin, B. K. P. Scaife, and S. W. Charles. Relaxation and resonance in ferrofluids. *J. Magn. Magn. Mater.* **122,** 159-163, 1993.

[110] M. Hanson. The frequency dependence of the complex susceptibility of magnetic liquids. *J. Magn. Magn. Mater.* **96,** 105-113, 1991.

[111] R. Andrews, D. Jacques, A. M. Rao, F. Derbyshire, D. Qian, X. Fan, E. C. Dickey, and J. Chen. Continuous production of aligned carbon nanotubes: a step closer to commercial realization. *Chem. Phys. Lett.* **303,** 467-474, 1999.

[112] M. Mayne, N. Grobert, M. Terrones, R. Kamalakaran, M. Rühle, H. W. Kroto, and D. R. M. Walton. Pyrolytic production of aligned carbon nanotubes from homogeneously dispersed benzene-based aerosols. *Chem. Phys. Lett.* **338,** 101-107, 2001.

[113] K. Lipert, F. Kretzschmar, M. Ritschel, A. Leonhardt, R. Klingeler, and B. Büchner. Nonmagnetic carbon nanotubes. *J. Appl. Phys.* **105,** 063906, 2009.

[114] A. Vyalikh, A. U. B. Wolter, S. Hampel, D. Haase, M. Ritschel, A. Leonhardt, H.-J. Grafe, A. Taylor, K. Krämer, B. Büchner, and R. Klingeler. A carbon-wrapped nanoscaled thermometer for temperature control in biological environments. *Nanomedicine* **3(3),** 321-327, 2008.

[115] D. Haase, S. Hampel, A. Leonhardt, J. Thomas, N. Mattern, and B. Büchner. Facile one-step-synthesis of carbon wrapped copper nanowires by thermal decomposition of Copper(II)acetylacetonate. *Surface and Coatings Technology* **201,** 9184-9188, 2007.

[116] S. Hampel, A. Leonhardt, D. Selbmann, K. Biedermann, D. Elefant, C. Mueller, T. Gemming, and Buechner. Growth and characterization of filled carbon nanotubes with ferromagnetic properties. *Carbon* **44,** 2316-2322 , 2006.

[117] P. Lukanov. Synthesis of filled carbon nanotubes and carbon encapsulated nanoparticles for biomedical applications. PhD thesis Toulouse University, 2010.

[118] E. Pellicer, A. B. González-Guerrero, J. Nogués, L. M. Lechuga, and E. Mendoza. Assessment of catalyst particle removal in multi-wall carbon nanotubes by highly sensitive magnetic measurements. *Carbon* **47,** 758-763, 2009.

[119] A. Taylor, Y. Krupskaya, S. Costa, S. Oswald, K. Krämer, S. Füssel, R. Klingeler, B Büchner, E. Borowiak-Palen, and M. P. Wirth. Functionalization of Carbon Encapsulated Iron Nanoparticles. *Journal of Nanoparticle Research* **12,** 513-519, 2010.

[120] S. Cai, Y. Xie, T. R. Bagby, M. S. Cohen, and M. L. Forrest. Intralymphatic Chemotherapy Using a Hyaluronan-Cisplatin Conjugate. *Journal of Surgical Research* **147(2),** 247-252, 2008.

[121] K. J. Haxton and H. M. Burt. Hyperbranched polymers for controlled release of cisplatin. *Dalton Transactions* **43,** 5872-5875, 2008.

[122] X. Yan and R. A. Gemeinhart. Cisplatin delivery from poly(acrylic acid-co-methyl methacrylate) microparticles. *Journal of Controlled Release* **106(1-2),** 198-208, 2005.

[123] A. Taylor, Y. Krupskaya, K. Krämer, S. Füssel, R. Klingeler, B Büchner, and M. P. Wirth. Cisplatin-loaded carbon-encapsulated iron nanoparticles and their *in vitro* effects in magnetic fluid hyperthermia. *Carbon* **48,** 2327-2334, 2010.

[124] J. van der Zee. Heating the patient: a promising approach? *Ann Oncol* **13(8),** 1173-1184, 2002.

[125] U. Gneveckow, A. Jordan, R. Scholz, V. Brüß, N.Waldöfner, J. Ricke, A. Feussner, B. Hildebrandt, B. Rau, and P. Wust. Description and characterization of the novel hyperthermia and thermoabation-system MFH® 300 F for clinical magnetic fluid hyperthermia. *Med. Phys.* **31,** 1444-1451, 2004.

[126] E. S. Handy, R. Ivkov, D. Ellis-busby, and A. Foreman. Thermotherapy via targeted delivery of nanoscale magnetic particles. United States Patent 7074175, 2006.

[127] A. Jordan, N. Waldoefner, and R. Scholz. Method For Carrying Therapeutic Substances Into Cells. United States Patent Application 20080187595, 2008.

Acknowledgements

First of all I am deeply thankful to Prof. Bernd Büchner for this beautiful opportunity to work in his team with great colleagues, interesting projects, and fascinating equipment.

Great thanks to Dr. Vladislav Kataev for his continuous interest to our work, for always productive and interesting discussions and for his detailed answers to any question that can ever appear.

Many thanks to all members of the IFW ESR group with whom I enjoyed working together. Very special thanks to Alexey Alfonsov who always gave me every possible support in my work and not only. It was also very pleasant to work with Dr. Guillaume Lang, Ferdinand Lipps, Dr. Mohammed Elbahrawy, and Yulieth Arango.

I am very grateful to Prof. Rüdiger Klingeler for his kind support and understanding. No matter what is the question or problem he is always ready to listen, understand and give a good advice.

Special kind thanks to my officemates Matthias Lutz, Ahmed El Gendy, and Kamil Lipert for all the nice moments we spent together. It was really a great time full of different emotions, fruitful discussions, and interesting experience.

I would like to say “Many Thanks!” to my “first diploma student” Christopher Mahn for his inexhaustible optimism. He appeared in Dresden right in the beginning of my stay here and was the first person with whom I communicated a lot. Actually, it is still a question, who and from whom of us learned more that time.

Also, I want to thank the Marie Curie Research Training Network CARBIO, with special thanks to its coordinator, for all those opportunities to meet interesting people, to learn interesting things in the most beautiful places all over the Europe.

Thanks to Dr. Olga Kataeva for the X-ray crystal structures of our studied complexes and to Dr. Yurii Skourski for the pulsed-field magnetization measurements in the Rossendorf Research Center. Thanks to Dr. Evgeniya Vavilova, Dr. Ruslan Zaripov, and Prof. Kev Salikhov from the Zavoisky Physical-Technical Institute in Kazan for their inestimable contribution to the pulsed ESR measurements and discussions of the results. Moreover, I thank all my colleagues with whom I spent time working in the lab or having interesting discussions, a specially, Dr. Anupama Parameswaran, Wolfram Lorenz, Dr. Anja Wolter, Dr. Silke Hampel, Sebastian Gaß, and Dr. Arthur Taylor.

Publication List

1. **Y. Krupskaya**, C. Mahn, A. Parameswaran, A. Taylor, K. Krämer, S. Hampel, A. Leonhardt, M. Ritschel, B. Büchner, R. Klingeler. Magnetic study of iron-containing carbon nanotubes: feasibility for magnetic hyperthermia. *J. Magn. Magn. Mater.* **321**, 4067-4071, 2009.
2. A.A. El-Gendy, E.M.M. Ibrahim, V.O. Khavrus, **Y. Krupskaya**, S. Hampel, A. Leonhardt, B. Büchner, R. Klingeler. The synthesis of carbon coated Fe, Co and Ni nanoparticles and an examination of their magnetic properties. *Carbon* **47**, 2821-2828, 2009.
3. A. Taylor, **Y. Krupskaya**, S. Costa, S. Oswald, K. Krämer, S. Füssel, R. Klingeler, B. Büchner, E. Borowiak-Palen, M.P. Wirth. Functionalization of carbon encapsulated iron nanoparticles. *J. Nanopart. Res.* **12**, 513-519, 2010.
4. **Y. Krupskaya**, A. Parameswaran, A. Alfonsov, R. Klingeler, V. Kataev, N. Beyer, J. Lach, M. Gressenbuch, B. Kersting, B. Büchner. High-Field ESR and Magnetization Study of a Novel Macrocyclic Chelate Trinuclear Ni(II) Complex. *J. Low Temp. Phys.* **159**, 84-87, 2010.
5. K. Lipert, M. Ritschel, A. Leonhardt, **Y. Krupskaya**, B. Büchner, R. Klingeler. Magnetic properties of carbon nanotubes with and without catalysts. *J. Phys.: Conf. Ser.* **200**, 072061, 2010.
6. V. Miluykov, I. Bezkishko, D. Krivolapov, O. Kataeva, O. Sinyashin, E. Hey-Hawkins, A. Parameswaran, **Y. Krupskaya**, V. Kataev, R. Klingeler, B. Büchner. The binuclear 1,2-diphosphacyclopentadienyl manganese(I) complexes: synthesis, structure and magnetic properties. *Organometallics* **29**, 1339-1342, 2010.
7. **Y. Krupskaya**, A. Alfonsov, A. Parameswaran, V. Kataev, R. Klingeler, G. Steinfeld, N. Beyer, M. Gressenbuch, B. Kersting, B Büchner. Interplay of Magnetic Exchange Interactions and Ni-S-Ni Bond Angles in Polynuclear Nickel(II) Complexes. *ChemPhysChem* **11**, 1961-1970, 2010.
8. A. Taylor, **Y. Krupskaya**, K. Krämer, S. Füssel, R. Klingeler, B. Büchner, M.P. Wirth. Cisplatin Loaded Carbon Encapsulated Iron Nanoparticles and its in vitro effects in Magnetic Fluid Hyperthermia. *Carbon* **48**, 2327-2334, 2010.

9. M. U. Lutz, K. Lipert, **Y. Krupskaya**, S. Bahr, A. Wolter, A. A. El-Gendy, S. Hampel, A. Leonhardt, A. Taylor, K. Krämer, B. Büchner, R. Klingeler. Feasibility of Magnetically Functionalised Carbon Nanotubes for Biological Applications: From Fundamental Properties of Individual Nanomagnets to Nanoscaled Heaters and Temperature Sensors. In "Carbon Nanotubes for Biomedical Applications" ed. R. Klingeler, R. B. Sim. *Springer-Verlag Berlin Heidelberg*, 2011.

10. A. Das, K. Gieb, **Y. Krupskaya**, S. Demeshko, S. Dechert, R. Klingeler, V. Kataev, B. Büchner, P. Müller, F. Meyer. A New Family of 1D Exchange Biased Heterometal Single-Molecule Magnets: Observation of Pronounced Quantum Tunneling Steps in the Hysteresis Loops of Quasi-Linear {Mn2Ni3} Clusters. *J. Am. Chem. Soc.* **133**, 3433-3443, 2011.

11. D. Yakhvarov, E. Trofimova, O. Sinyashin, O. Kataeva, Y. Budnikova, P. Lönnecke, E. Hey-Hawkins, A. Petr, **Y. Krupskaya**, V. Kataev, R. Klingeler, B. Büchner. New Dinuclear Nickel(II) Complexes: Synthesis, Structure, Electrochemical and Magnetic Properties. *Inorg. Chem.* **50**, 4553-4558, 2011.

12. P. Lukanov, V. K. Anuganti, **Y. Krupskaya**, A.-M. Galibert, B. Soula, C. Tilmaciu, A. H. Velders, R. Klingeler, B. Büchner, E. Flahaut. CCVD synthesis of carbon-encapsulated cobalt nanoparticles for biomedical applications. *Adv. Func. Mater.* DOI: 10.1002/adfm.201100364

13. **Y. Krupskaya**, R. Zaripov, E. Vavilova, V. Miluykov, I. Bezkishko, D. Krivolapov, O. Kataeva, O. Sinyashin, E. Hey-Hawkins, V. Voronkova, K. Salikhov, V. Kataev, B. Büchner. Electron spin coherence in antiferromagnetically coupled Mn-dimer complexes. *Phys. Rev. B* (submitted)

Diese Arbeit wurde unter Betreuung von Prof. Dr. B. Büchner am Institut für Festkörperforschung (IFF) des Instituts für Festkörper- und Werkstoffforschung Dresden e.V. (IFW Dresden) angefertigt.

Versicherung

Hiermit versichere ich, dass ich die vorliegende Arbeit ohne zulässige Hilfe Dritter und ohne Benutzung anderer als der angegebenen Hilfsmittel angefertigt habe; die aus fremden Quellen direkt oder indirekt übernommenen Gedanken sind als solche kenntlich gemacht. Die Arbeit wurde bisher weder im Inland noch im Ausland in gleicher oder ähnlicher Form einer anderen Prüfungsbehörde vorgelegt.

Ich erkenne hiermit die Promotionsordnung der TU Dresden an.